UNIVERSITY OF OKLAHOMA

GRADUATE COLLEGE

COMPREHENSIVE PERFORMANCE EVALUATION AND OPTIMIZATION OF HIGH THROUGHPUT SCANNING MICROSCOPY FOR METAPHASE CHROMOSOME IMAGING

A DISSERTATION

SUBMITTED TO THE GRADUATE FACULTY

in partial fulfillment of the requirements for the

Degree of

DOCTOR OF PHILOSOPHY

By

YUCHEN QIU
Norman, Oklahoma
2013

COMPREHENSIVE PERFORMANCE EVALUATION AND OPTIMIZATION OF HIGH THROUGHPUT SCANNING MICROSCOPY FOR METAPHASE CHROMOSOME IMAGING

A DISSERTATION APPROVED FOR THE
SCHOOL OF ELECTRICAL AND COMPUTER ENGINEERING

BY

Dr. Hong Liu, Chair

Dr. Shibo Li

Dr. Lei Ding

Dr. Monte Tull

Dr. Jizhong Zhou

To my parents

Acknowledgements

The author would like to express his sincere gratitude to his advisor, Dr. Hong Liu, who has provided the author such an incredible opportunity to perform his encouraging research. The author has benefited tremendously from his tireless mentoring and vast knowledge.

The author gratefully acknowledges Dr. Bin Zheng and Dr. Shibo Li (Health Sciences Center, University of Oklahoma), for their continued support of the author's research.

The author also gratefully acknowledges all his committee members: Dr. Lei Ding, Dr. Monte Tull, and Dr. Jizhong Zhou, for their time and efforts serving in author's Ph.D. program committee.

The author also greatly appreciates the help from the members of the research group: Molly Donovan Wong, Yuhua Li, Xiaodong Chen, Da Zhang, Xingwei Wang, Zheng Li, Di Wu, Liqiang Ren, Jie Song, and Muhammad U. Ghani.

Table of Contents

List of Tables

List of Figures

Abstract

Specimen scanning is a critically important tool for diagnosing the genetic diseases in today's hospital. In order to reduce the clinician's work load, many investigations have been conducted on developing automatic sample screening techniques in the last twenty years. However, the currently commercialized scanners can only accomplish the low magnification sample screening (i.e. under 10× objective lens), and still require clinicians' manual operation for the high magnification image acquisition and confirmation (i.e. under 100× objective lens). Therefore, a new high throughput scanning method is recently proposed to continuously scan the specimen and select the clinically analyzable cells. In the medical imaging lab, University of Oklahoma, a prototype of high throughput scanning microscopy is built based on the time delay integration (TDI) line scanning detector.

This new scanning method, however, raises several technical challenges for evaluating and optimizing the performance. First, we need to use the clinical samples to compare this new prototype with the conventional two-step scanners. Second, the system DOF should be investigated to assess the impact on clinically analyzable metaphase chromosomes. Further, in order to achieve the optimal results, we should carefully assess and select the auto-focusing methods for the high throughput scanning system. Third, we need to optimize the scanning scheme by finding the optimal trade-off between the image quality and efficiency. Finally, analyzing the performance of the various image features is meaningful for improving the performance of the computer aided detection (CAD) scheme under the high throughput scanning condition.

The purpose of this dissertation is to comprehensively evaluate the performance of the high throughput scanning prototype. The first technical challenge was solved by the first investigation, which utilized a number of 9 slides from five patients to compare the detecting performance of the high throughput scanning prototype. The second and third studies were performed for the second technical challenge. In the second study, we first theoretically computed the DOF of our prototype and then experimentally measured the system DOF. After that, the DOF impact was analyzed using cytogenetic images from different pathological specimens, under the condition of two objective lenses of 60× (dry, N.A. = 0.95) and 100× (oil, N.A. = 1.25). In the third study, five auto-focusing functions were investigated using metaphase chromosome images. The performance of these different functions was compared using four widely accepted criteria. The fourth and fifth investigations were designed for the third technical challenge. The fourth study objectively assessed chromosome band sharpness by a gradient sharpness function. The sharpness of the images captured from standard resolution target and several pathological chromosomes was objectively evaluated by the gradient sharpness function. The fifth study presented a new slide scanning scheme, which only applies the auto-focusing operations on limited locations. The focusing position was adjusted very quickly by linear interpolation for the other locations. The sixth study was aimed for the fourth technical challenge. The study investigated 9 different feature extraction methods for the CAD modules applied on our high throughput scanning prototype. A certain amount of images were first acquired from 200 bone marrow cells. Then the tested features were performed on these images and the images containing clinically meaningful chromosomes were selected using each

feature individually. The identifying accuracy of each feature was evaluated using the receiver operating characteristic (ROC) method.

In this dissertation, we have the following results. First, in most cases, we demonstrated that the high throughput scanning can select more diagnostic images depicting clinically analyzable metaphase chromosomes. These selected images were acquired with adequate spatial resolution for the following clinical interpretation. Second, our results showed that, for the commonly used pathological specimens, the metaphase chromosome band patterns are clinically recognizable when these chromosomes were obtained within 1.5 or 1.0 μm away from the focal plane, under the condition of applying the two 60× or 100× objective lenses, respectively. In addition, when scanning bone marrow and blood samples, the Brenner gradient and threshold pixel counting methods can achieve the optimal performance, respectively. Third, we illustrated that the optimal scanning speed of clinical samples is 0.8 mm/s, for which the captured image sharpness is optimized. When scanning the blood sample slide with an auto-focusing distance of 6.9 mm, the prototype obtained an adequate number of analyzable metaphase cells. More useful cells can be captured by increasing the auto-focusing operations, which may be needed for the high accuracy diagnosis. Finally, we found that the optimal feature for the online CAD scheme is the number of the labeled regions. When applying the offline CAD scheme, the satisfactory results can be achieved by combining four different features including the number of the labeled regions, average region area, average region pixel value, and the standard deviation of the either region circularity or distance.

Although these investigations are encouraging, there exist several limitations. First, the number of the specimens is limited in most of the assessments. Second, some important impacts, such as the DOF of human eye and the sample thickness, are not considered. Third, more recently proposed algorithms and image features are not used for the evaluation. Therefore, several further studies are planned, which may provide more meaningful information for improving the scanning efficiency and image quality. In summary, we believe that the high throughput scanning may be extensively applied for diagnosing genetic diseases in the future.

Keywords: Metaphase chromosome imaging, high throughput scanning, computer aided detection (CAD) , performance evaluation and optimization, depth of field (DOF), cytogenetic image quality, digital pathology, automatic scanning method, sampling scheme, auto-focusing technique, image sharpness, objective evaluation, chromosome feature extraction

Chapter 1: Introduction

1.1 Objective

Specimen scanning is an effective tool for the diagnosis of genetic diseases such as leukemia [1-3]. Traditionally, the scanning is accomplished manually by clinicians, which is tedious and inefficient. Although many research efforts have been devoted to the development of automatic sample screening in the last twenty years [4], the currently commercialized image scanners still require two step scanning (10× screening and 100× image acquisition) and need clinicians' manual operation [5, 6]. In order to improve the current method, a new technique, high throughput scanning microscopy, was recently proposed, which is able to continuously scan the specimen and select the clinically analyzable cells. In addition, the obtained images have enough resolving power for the clinical diagnosis. In the medical imaging lab, University of Oklahoma, a new prototype of high throughput microscopic scanning microscopy is developed, which is based on the time delay integration (TDI) line scanning camera. However, there are several technical challenges for the assessing and optimizing the new prototype. The objective of this dissertation is to comprehensively evaluate the prototype and optimize the performance.

1.2 Dissertation organization

This dissertation is composed of 10 chapters. Besides the chapter 1, the other 9 chapters are organized as follows:

Chapter 2 briefly presents the background of the entire dissertation. It consists of 4 sections. Section 1 introduces the basic concepts about the chromosome diagnosis, including the chromosome sample preparation and karyotyping. Section 2 explains why we need to scan and identify the analyzable metaphase chromosomes. Section 3 is a brief introduction of chromosome abnormalities and the related diseases. Section 4 discusses the concepts of fluorescent in situ hybridization technique (FISH) method.

Chapter 3 explains the motivation of why high throughput scanning method is proposed. Section 1 first discusses the relationship between the genetic diseases and chromosome abnormalities. Section 2 then summarizes the recent research progress of the automatic specimen scanning based on the transmitted light or florescent microscopic scanners, respectively. After that, section 3 presents the architecture of the high throughput scanning prototype developed in our lab. Finally section 4 discusses the technical challenges of the high throughput scanning microscopy.

Chapter 4 is a preliminary performance comparison between high throughput scanning prototype and the conventional scanners [7]. A total of 9 slides obtained from five patients' blood and bone marrow sample were scanned by both of the two scanning machines. The system performance was evaluated by comparing the number of the clinically meaningful metaphase chromosomes selected by each scanner.

Chapter 5 investigates the off-focusing tolerance of the clinically analyzable metaphase chromosomes acquired from several different types of pathological samples [8, 9]. In this chapter, the optical depth of focus (DOF) was first computed by a well-recognized theoretic model, and then the DOF was measured using a standard USAF1951 resolution target. After that, the DOF impact on the chromosomes was subjectively assessed by comparing the band pattern sharpness of the cytogenetic images which are captured inside or outside the system DOF range. The assessment was conducted under two objective lenses of 60× (dry, N.A. = 0.95) and 100× (oil, N.A. = 1.25).

Chapter 6 tests and compares five auto-focusing functions [10]. The five tested auto-focusing functions were first detailed. Then a certain amount of images were obtained from bone marrow and blood specimens. The five tested auto-focusing functions were applied on these images, and their performance was assessed by four different widely accepted criteria. The optimal functions were finally suggested for each specimen, respectively.

Chapter 7 objectively assesses the chromosome band sharpness [11]. The standard resolution target and several pathological chromosomes were first imaged at different scanning speeds, and the sharpness was objectively assessed by the gradient sharpness function. According to the computed sharpness, the optimal scanning speeding was suggested for the chromosome screening.

Chapter 8 analyzes a sampling-focusing method, which only applies the auto-focusing operations on a limited number of locations of the imaging field [12]. For the rest of the imaging field, the focusing position is adjusted very quickly through linear interpolation. Using different sampling schemes, the investigated method was evaluated on scanning a certain area of blood specimens. The numbers of the selected analyzable chromosomes were summarized for comparison.

Chapter 9 utilizes the receiver operating characteristic (ROC) method to select the optimal feature for the analyzable metaphase chromosome selection. In this chapter, the ROC curve was first briefly explained. Next, a number of 200 bone marrow cells including 67 clinically meaningful chromosomes were acquired under the high throughput scanning prototype. After that, a number of 9 image features were individually applied on these obtained images, to group the analyzable images from the others. The classification performance of each feature was assessed by the ROC curve. Finally, the optimal features were suggested for the first on-line and second off-line CAD schemes, respectively.

Chapter 10 summarizes the entire dissertation and suggests the future studies.

Chapter 2: Background

2.1 Human chromosomes: Extraction and karyotyping

Chromosome is a specially organized biological structure in the cell nucleus which carries heredity materials including Deoxyribonucleic acid (DNA), Ribonucleic acid (RNA), and some other special proteins [13]. In the clinical application, physicians are interested in the number and morphology of the human chromosomes. The chromosome numbers are different for a variety of organisms. The number of the human chromosomes was first discovered by Tjio and Levan in 1956, which illustrated that each normal human cell contains 46 chromosomes, including 44 autosomes and 2 allosomes [1]. The chromosomes morphology varies in the different stages of the cell division. In the interphase stage, chromosomes are inside the cell nucleus for DNA duplication, as demonstrated in Fig 1 (a). In the mitosis stage, the chromosomes are divided into two identical parts for the two individual daughter cells. The mitosis stage can be further classified into several steps, among which the middle step is called metaphase. In metaphase step, two identical parts of one chromosome are attached at the centromere, and these chromosomes are highly condensed and coiled, as shown in Fig 1 (b). Comparing to the other steps, the metaphase chromosomes have the best morphology, thus they are most suitable for the clinical diagnosis.

In the clinical application, the metaphase chromosomes are obtained from different kinds of patient samples, including bone marrow, peripheral blood, product of conception, amniotic fluid etc. The chromosome extracting procedure is composed of three steps: incubation, fixation, and spreading. These obtained samples are first incubated for several days, during which phytoagglutinin is applied to increase the cell reproduction. At the end of the incubation, the cell division is inhibited by colchicines, to maximize the number of the useful metaphase chromosomes. Then, using the mixture of carbinol and glacial acetic acid, the cells are fixed at one stage of the cell cycle. The fixed chromosomes are finally spreaded on the microscopic slides for the purpose of following observation.

Before staining, the chromosomes are transparent and cannot be observed under the transmitted microscope. The clinically distinguishable chromosome segments are defined as the chromosome band patterns, which are accomplished by the banding techniques. Among different banding methods, the G-banding technique is used in all the experiments discussed in this dissertation. The G-banding technique utilizes the Giemsa dye to stain the investigated chromosomes, which are composed of alternating bright and dark segments, as demonstrated in Fig 2.

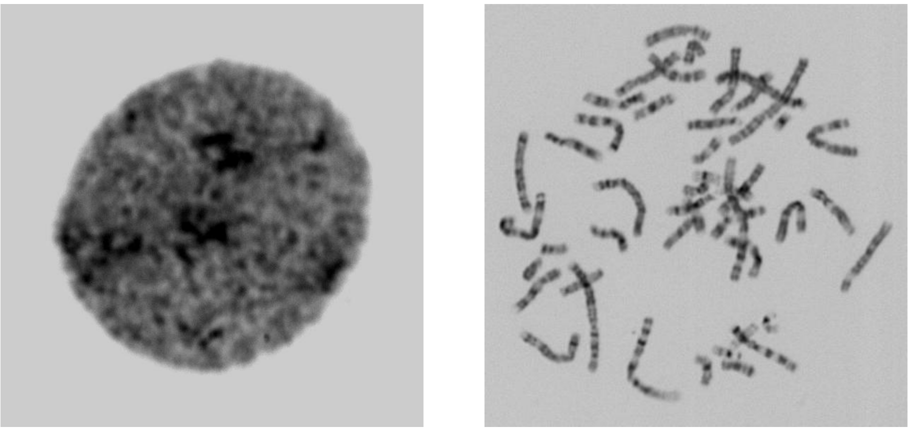

(a) (b)

Figure 1: The microscopic images of chromosomes

(a): The microscopic image of an interphase chromosomes (b): The microscopic image of a metaphase chromosomes

The 46 chromosomes can be grouped into 23 pairs, each of which contains a unique band pattern. Since all the chromosomes are randomly distributed on the captured images, we need to organize them with a standard order, which is defined as chromosome karyotyping. As illustrated in Fig 2 (b), each pair of the chromosomes is recognized from Fig 2 (a), by comparing the unique band pattern with a standard layout. The karyotyped results are ordered with decreasing length.

(a) (b)

Figure 2: The microscopic images of a metaphase bone marrow cells before (a) and after (b) karyotyping

(Courtesy Genetics Lab, University of Oklahoma Health Sciences Center)

2.2 Human chromosomes: Indentifying the pathologically analyzable metaphase chromosomes

As mentioned before, only metaphase chromosomes are suitable for the clinical investigation. However, metaphase chromosomes are not all analyzable for the diagnostic purpose. Due to the reasons of the clinical sample preparation and processing, some metaphase chromosomes are overlapped with each other, and some chromosomes are too close to be distinguished under the microscope, as demonstrated in Fig 3 (a) and (b). These cells are defined as clinically un-analyzable metaphase chromosomes.

Clinicians need to screen and detect the clinically meaningful chromosomes before the karyotyping. Since metaphase chromosomes only account for approximately 4% of all the cells depicted on the clinical slide and only part of the metaphase cells are pathologically analyzable, clinician need to scan 3-5 slides to identify a certain amount of analyzable chromosomes, which is labor intensive and time consuming.

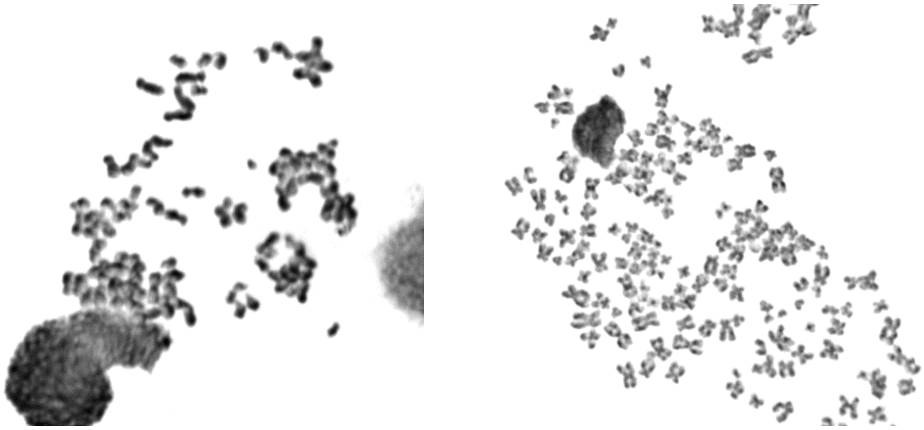

(a) (b)

Figure 3: The microscopic images of pathologically meaningless chromosomes (a): Two many metaphase chromosomes aggregated together (b): metaphase chromosomes from two cells.

2.3 Human chromosomes: Chromosome abnormalities

Since Philadelphia translocation t(9;22)(q34;q11) was first discovered by Novell and Hungerford in 1959, chromosome abnormalities have been proved to be consistent with genetic related diseases [3]. Chromosome abnormalities can be classified into structure abnormality and number abnormality. The Philadelphia translocation is a typical example of structure abnormality, which is a reciprocal translocation between 9th and 22nd chromosome. On the karyotyped image Fig 4, the 9th chromosome is longer and 22th chromosome is shorter than the normal case. In addition, their band patterns are also different. Chromosome number change is defined as the number deletion (monosomy) or redundancy (trisomy). For example, 21 trisomy is a sensitive indicator of Down's Syndrome, which has an extra 21st chromosome, as illustrated in Fig 4 (b). In Fig 4 (c), however, has only one chromosome in 16th, 18th, and 22th chromosome, which is associated with a specific leukemia.

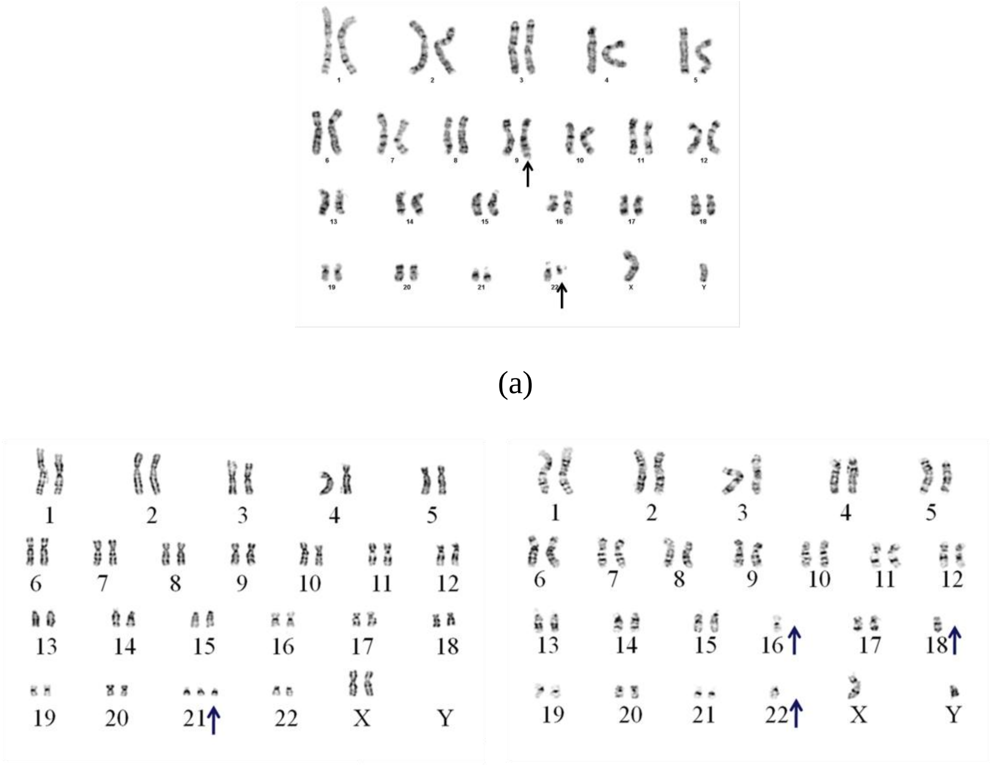

(a)

(b) (c)

Figure 4: Three examples of chromosome abnormities

(a): Philadelphia translocation (b): 21 trisomy (c): 16th, 18th, and 22th monosomy (Courtesy Genetics Lab, University of Oklahoma Health Sciences Center)

In hospital, physicians have different standards for various samples. For the bone marrow sample, clinicians need to image and karyotype at least 20 analyzable metaphase chromosomes for each case. Since the heterogeneous case might contain both normal and abnormal chromosome band patterns, the case will be diagnosed as positive if chromosome abnormalities (number or structure) are identified in three or more cells. For the peripheral blood sample, clinicians need to find 20 analyzable chromosomes. Among these detected chromosomes, 17 cells are examined by counting the number of the chromosomes, while the other three cells are karyotyped to analyze both the number and structure abnormalities.

2.4 The fluorescent in situ hybridization (FISH) technique

The method of fluorescent in situ hybridization (FISH) [14, 15] has been widely used in the detection of gene abnormality for medical applications such as prenatal aneuploidy [16] and chronic myeloid leukemia (CML) [17]. Similarly, the FISH sample preparing procedure also includes cell incubation, fixation and spreading [18]. After the cell spreading, the fluorescent biomarkers are added, which diffuse into the cell and finally attach the centromere of the interested chromosomes. Under the fluorescent microscope, the investigated chromosomes can be observed as circular dots with different colors. Fig 5 is an example of the FISH image. 13rd and 21st chromosomes are indicated by the centromeric CEPX (DXZ1) and CEP 3 (D3Z1) spectrum probe, which appear as green and red dots, respectively [19]. The blue background of the entire cell nucleus is stained by the DAPI. The chromosome abnormally is investigated by counting the number of the dots. Clinicians need to check at least 50 cells for each case.

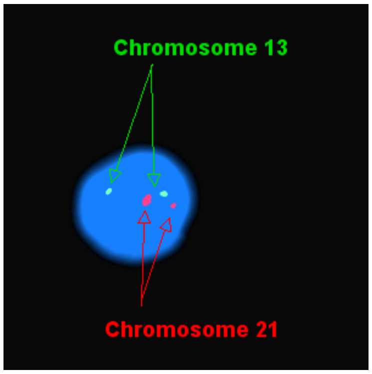

Figure 5: A microscopic image of an interphase cell processed by FISH technique

(Courtesy Genetics Lab, University of Oklahoma Health Sciences Center)

Chapter 3: The motivation of investigating the high throughput scanning

3.1 Why do we need to develop automatic scanning microscopy?

Pathological examination of clinical specimens provides a ground-truth of disease diagnosis. In clinical practice, consistent chromosome abnormalities have been proved to be associated with some serious diseases [1-3, 6, 20, 21]. Furthermore, pathological chromosome analysis helps to categorize patients into different clinical groups of various cancer or disease prognoses, for which oncologists could evaluate cancer prognosis and select more effective treatment procedures [22].

For the chromosome analysis, karyotyping and fluorescence in situ hybridization (FISH) are the standard techniques in today’s hospital [23, 24]. Karyotyping is only suitable for the analyzable metaphase chromosomes [23]. For each indentified chromosome of the interested cell, it is compared with the standard chromosome band patterns, to determine the chromosome abnormalities on number or morphology. All these chromosomes are arranged in pair and ordered with decreasing length on the finally karyotyped result. FISH technique is suitable for both metaphase and interphase chromosomes. The interested DNA segments are attached with fluorescent biomarkers, which can be observed as colored dots under the fluorescent microscope [24]. Clinicians can identify the abnormalities by counting the number or estimating the size of the dots.

Traditionally, karyotyping or FISH analysis are accomplished manually in the hospital. However, the visual searching and identification is very labor intensive. In addition, the inter-observer variability during the chromosome selection may produce inconsistent results. Therefore, the development of automatic scanning microscopy has received extensive research interest since 1980’s [4, 25-31].

3.2 Introduction to automatic scanning microscopy: Literature review

3.2.1 The automatic scanning microscopy for metaphase chromosome screening and karyotyping

The automatic scanning microscopy can be divided into three basic steps: 1) image acquisition; 2) image separation; 3) feature extraction and classification [4]. In order to find a desirable number (20-30) of analyzable metaphase chromosome cells for each patient, the machine needs to scan 3 to 5 sample slides for one patient (in particular for the bone marrow specimens). The current commercialized image scanning systems (i.e., MetaSystems, Altlussheim, Germany [21]) are semi-automatic, which screens the specimen under 10× or 20× objective lenses with low numerical aperture (N.A.), as illustrated in Fig 6 (a). Since these lenses cannot obtain images with adequate spatial resolution for the karyotyping, clinicians need to manually move the slide to the identified location and acquire the image under a high magnification objective lens. An example is demonstrated in Fig 6 (b).

After the images are obtained, the interested chromosomes are separated from the background, for the following feature extraction and classification. Before the segmentation, a low pass filter is applied to suppress the noise and remove the small size debris [32]. The chromosome separation is composed of two steps. First, the separated or clustered chromosomes are segmented from the background by setting an intensity threshold. Among the different threshold methods, the adaptive threshold [33] and region based level set [34] are considered as the best methods [35]. Then, the clustered chromosomes are disentangled as individual entities. The early disentangling methods, such as shape reasoning [36] or geometric contour separation [37], are only effective for the slightly overlapped chromosomes [38]. The method can be improved by using chromosome feature [39] and classification evidence [40]. Recently, a more accurate method employs global text and variant analysis [41], but the accuracy decreases when the image quality is deteriorated. Another recently reported method is based on the tree of choices, which is able to achieve an accuracy of 90% [33]. However, the dataset only contains 162 chromosome images [33]. In general, although the automatic segmentation and disentangle techniques are significantly improved in the last several years, they are still not satisfactory for clinical practice. The current commercialized scanning systems require clinician's intervention to correct the segmentation [4].

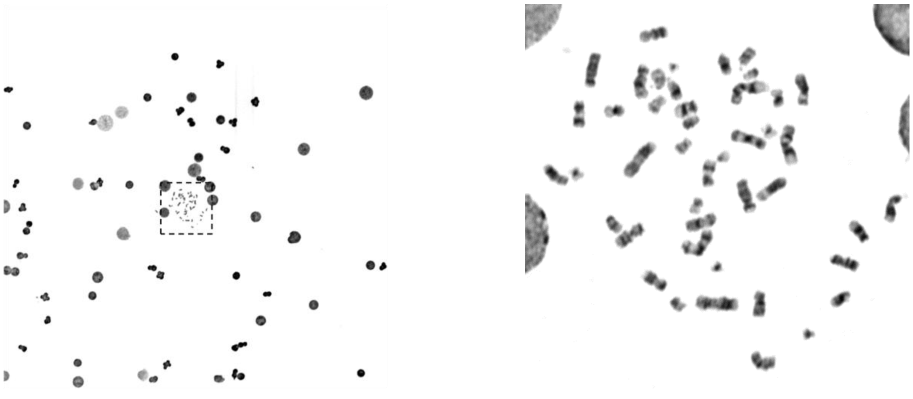

(a) (b)

Figure 6: The microscopic images of a clinically analyzable metaphase cell

(a): The cell was captured under 10× (N.A. = 0.25) objective lens (b): The cell was 100× (N.A. = 1.25) objective lens

The feature extraction and classification is the final step of the entire procedure [4, 42]. The common chromosome features include relative length [43-45], centrometric index [43-45], band pattern density profile [44-46], local energy [47], multi-resolution curvature [38], DNA index [28], and gradient profile [48]. Most of the above features are related to the chromosome centromere, thus some researchers investigated the algorithms of identifying and locating the centromeres depicted on the captured images [49, 50]. The classifying accuracy can be improved by using machine learning tools to combine the advantages of different features [28, 30, 51]. Some typical classifiers are Hopfield networks [52] or multilayer perception networks [28, 30, 45, 51, 53], support vector machine [54], and fuzzy rule based expert system [55]. Among these machine learning tools, multilayer perception networks (MPN) are most popularly used, as the MPN has relatively low complexity and satisfied classifying accuracy. Another interesting topic is the selection of the chromosome features. Although the optimal combination of the above features are suggested in some publications [53], feature selection are still highly dependent on the specific clinical application.

3.2.2 The automatic scanning microscopy for FISH screening

Similarly, the scanning microscopy for FISH analysis is also divided into four steps. The FISH images are acquired from 2 dimensional (2D) or 3 dimensional (3D) fluorescence microscopes [56]. The first 2D FISH scanning system was proposed by Netten in 1997 [57]. The Netten's system can capture the fluorescent images of two different bio-markers (one background marker and one FISH marker). For each acquired image, the region of interest (ROI) depicting interested interphase cells are first determined by an automatically-chosen constant threshold algorithm [58], and the interphase cells are then separated from the ROI background using isodata threshold approach [59]. The FISH dots are finally segmented by a combined method of TopHat transform [60] and non-linear Laplacian operator edge detecting algorithm [61]. The segmented regions with proper size and relative intensity are considered as FISH dots and the number of the dots of each interphase cells is calculated as the final result. The Netten's prototype achieves an accuracy of 89%, which is comparable to the manual dot enumeration [57].

Although the test result was encouraging, a series of new scanners were proposed to further improve the Netten's FISH scanning prototype. Since several FISH biomarkers are applied in many clinical diagnosis, de Solórzano [62] reported a new scanner which is able to screen and identify the FISH emitting images from two FISH markers. Besides the dot number, the recently proposed scanners also applied the ratio of green and red dots [63], telomere length [64], translocation detection [21] for the diagnosis. In addition, some pre-processing algorithms, such as CCD response recovery [65, 66], contrast enhancement [65, 66], and systematic error correction [21, 62], were also utilized on the FISH scanners, to improve the detecting accuracy.

Due to the large sample thickness of the FISH cells, the interested DNA segments may be located differently in depth, but observed as overlapped dots under the 2D the fluorescence microscopes [67]. These overlapped signals can be easily distinguished by 3D confocal microscopes [67], and the distance of the different FISH dots can be computed more accurately [68, 69]. Besides the confocal microscopes, 3D FISH scanner can also be implemented by the regular 2D fluorescent microscope [70], which sequentially obtains a stack of FISH images at different focusing positions to create the 3D FISH images [70].

Different from the karyotyping CAD, the mostly widely used features for the FISH dots are contrast, intensity, size, texture, eccentricity, etc [21, 71]. Besides the ANN, several other classifiers, such as Fuzzy ARTMAP [72, 73], support vector machine [74], native Bayesian classifier (NBC) [75], are also applied, which are able to achieve a classifying accuracy up to 87.1% [73].

3.3 High throughput scanning microscopy: Concept and practice

Our research group has developed and tested a fully-automated microscopic scanning system based on a time-delay integration (TDI) scanning concept [76]. The scanner was built based on a commercially available microscope (Eclipse 50i, Nikon Instruments, Tokyo, Japan). The system includes a Time Delay Integration (TDI) CCD image detector (Piranha HS-40-04k40, Dalsa Company, Canada) and a motorized scanning stage (99S000, Ludl Electronic Products Ltd, U.S.A.).

Different from the previously reported scanners, the high throughput prototype is able to scan the image continuously when the stage is moving. The continuous scanning is accomplished by the Time Delay Integration (TDI) CCD image detector. The principle of the TDI camera is demonstrated by a simplified detector with 9 pixels. As demonstrated in Fig 7 (a), a small object will be obtained by the detector, for which the image exactly matches the size of one detector pixel. If the object is moving, the obtained image will be blurred under the same exposure time, which is defined as motion blur. An example is illustrated in Fig 7 (b). In order to overcome the motion blur, the TDI detector divides the long exposure into three short exposures, each of which can acquire the object within one camera pixel. Thus the images are not blurred, but the signal to noise radio (SNR) will decrease as the exposure time declines. The SNR can be enhanced by adding these three images properly, to finally create a high SNR image without motion blur, as shown in Fig 8 (d).

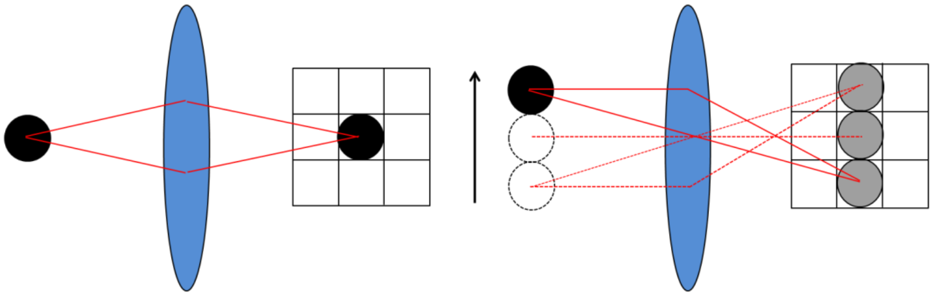

(a) (b)

Figure 7: A demonstration of the motion blur

(a): A still object is captured. (b): The image is obtained when the object is moving.

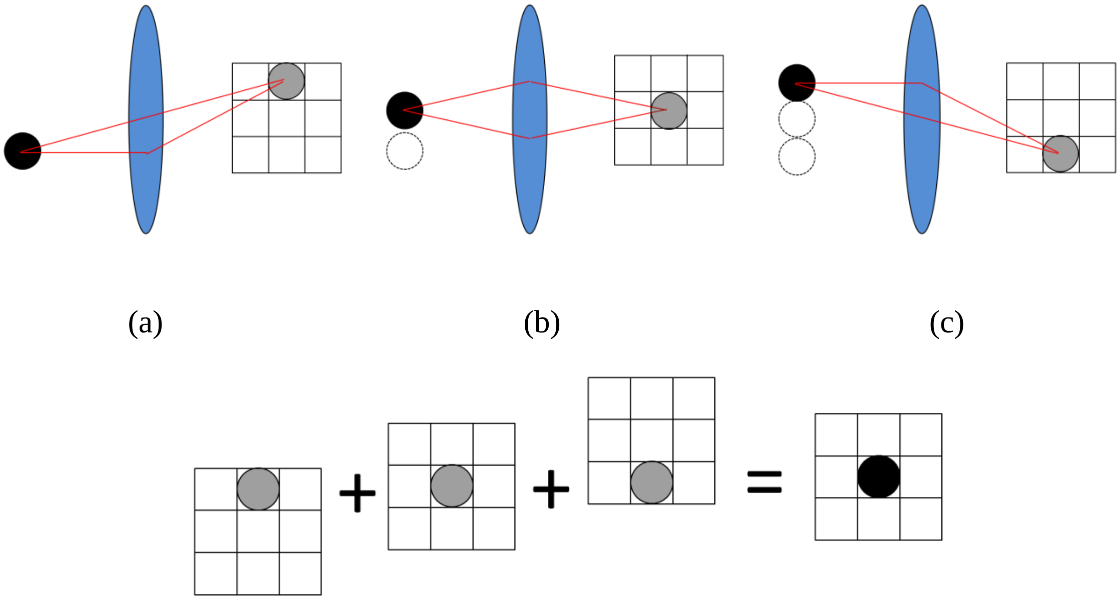

(a) (b) (c)

(d)

Figure 8: A demonstration of the time delay integration

The object is captured in first (a) second (b) and third (c) short exposure. (d): The final images are accomplished by add these three images properly.

In the high throughput scanning prototype, the CCD detector is made of a TDI chip that includes 4096 active photo-elements in the horizontal direction (X-direction). In the vertical direction (Y-direction) of the TDI detector, the signal are added and averaged by shifting the signal charges. For our specific detector, there are 96 pixels in the vertical direction (Y-direction). The output signal is given by:

$$n_{sig} = \sum_{i=1}^{96} n_i \tag{3-1}$$

where n_{sig} is the output signal, and n_i is the signal collected by each pixel in the vertical direction (Y-direction).

In the continuous scanning, the stage and the TDI camera should be synchronized. In order words, the image of the object must be acquired within exactly one detector pixel during the exposure. If the object is imaged partially in one pixel and partially in another pixel, the final image will also be blurred after the integration, which is defined as synchronization blur. An example is as demonstrated in Fig 9 (d). In order to avoid the synchronization blur, the speed of the stage and the sampling rate of the TDI camera must be matched, which is determined by the following formula [77]:

$$T = \frac{p}{V \times M} \tag{3-2}$$

In the formula, T is the exposure time. V is the scanning speed. M is the system magnification (i.e. the magnification of the objective lens), and p is the pixel size of the detector, which is 0.007mm for our scanning prototype.

Our TDI scanning prototype system has the capability of scanning a complete slide of 40mm × 20mm (0-40mm in X-direction, and 0-20 mm in Y-direction) under various optical magnification levels. As demonstrated in Fig 10 (a) and (b), the

USAF1951 resolution target (USAF1951, Edmund Optics, New Jersey, U.S.A.) is obtained at 12.28mm/sec under 10× (dry, N.A. = 0.25), and at 2.4mm/sec under 40× (dry, N.A. = 0.75), respectively. In Fig 11, metaphase chromosome cells are imaged using a 100× (oil, N.A. = 1.25) objective lens, with two scanning speeds (0.6mm/s and 1.2mm/s). As compared to the current digital microscopes equipped with 2-D (CCD) detectors, the new TDI scanning system has the potential to directly scan an entire specimen under a high magnification objective lens (i.e. 100× oil immersion objective lens). Thus, the acquired images can be directly used for the diagnostic purpose.

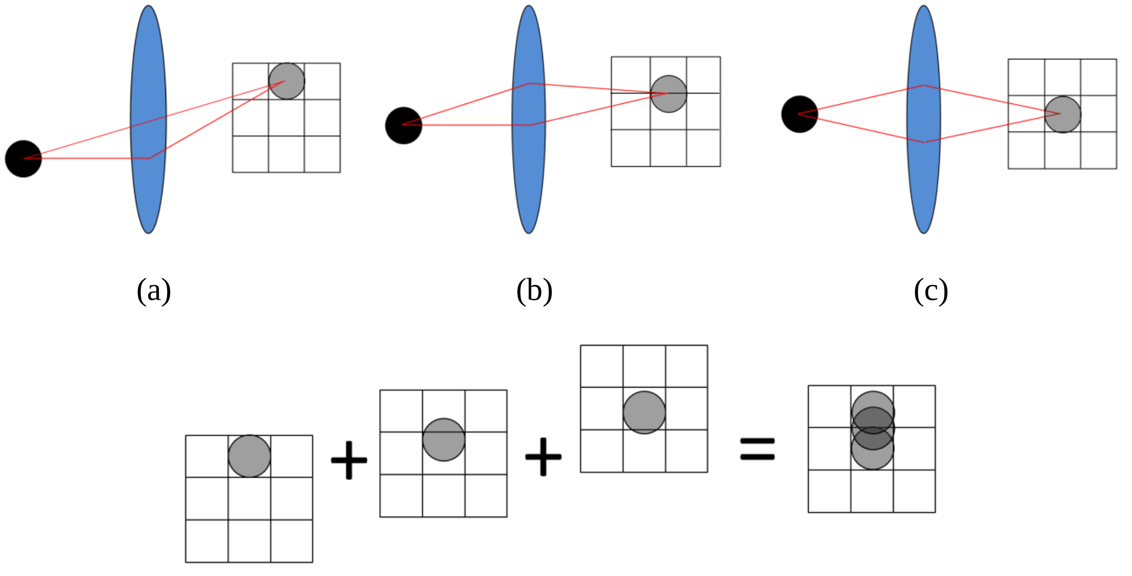
(a) (b) (c)

(d)

Figure 9: A demonstration of the synchronization blur

(a): The object is captured in first exposure. (b) In the second exposure, the object is acquired in synchronized state. (c): In the second exposure, the object is acquired in unsynchronized state. (d): If the system is not synchronized, the finally obtained image will be blurred.

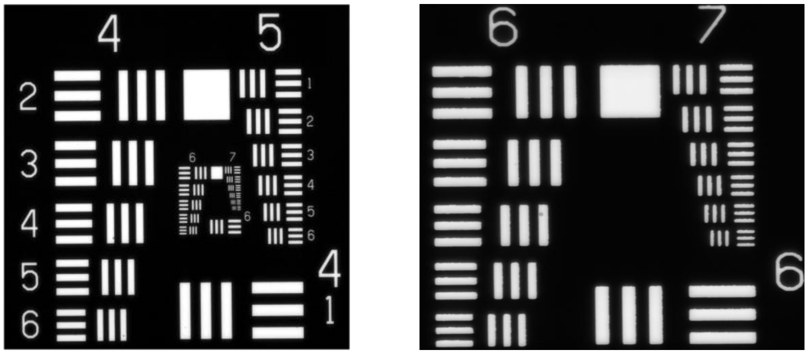

(a) (b)

Figure 10: The scanned images of an USAF1951 resolution target

The images were captured with TDI camera under (a) 10× (dry, N.A. = 0.25), 12.28 mm/sec stage moving speed, and TDI synchronization frequency of 17.75KHz, and (b) 40× (dry, N.A. = 0.75), 2.4mm/sec stage moving speed. TDI synchronization frequency is 14.4 kHz.

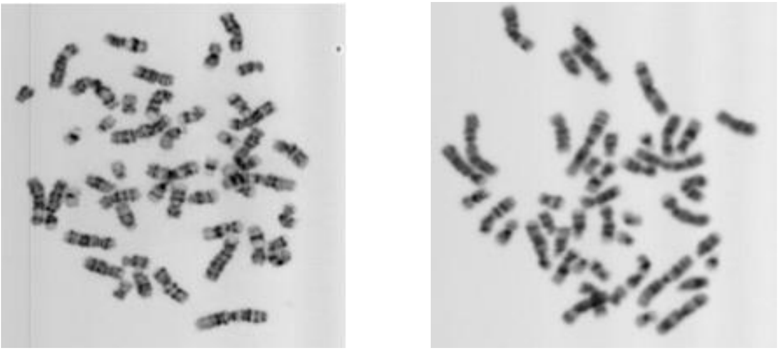

(a) (b)

Figure 11: The microscopic images of metaphase chromosomes obtained by a TDI camera under a 100× (oil, N.A. = 1.25) objective lens

They were obtained under (a) 0.6mm/sec stage scanning speed and TDI synchronization frequency of 11.25 kHz, and (b) 1.2mm/sec stage scanning speed and TDI synchronization frequency of 22.5 kHz.

3.4 Technical challenges of the current prototype

The automated high-resolution image scanner raises several technical challenges. First, the performance of the automated scanner needs to be compared with the traditional two-step scanners. Second, in order to keep the pathologic specimen in focus during the image scanning, we need to investigate the tolerance level of tolerance level of the off-focusing in clinically analyzable metaphase chromosomes. Furthermore, during the scanning, the focusing position of the specimen is maintained by applying the auto-focusing technique. But the performance of auto-focusing methods are application oriented, which must be carefully assessed to achieve the satisfactory results. Third, auto-focusing operations are very time consuming, especially when they are repeatedly applied during the scanning. Thus the optimal scanning scheme should also be examined to balance the efficiency and image quality. In addition, we need to carefully select the scanning speed, as sharpness of the obtained images might be deteriorated due to the short exposure, scanning blur, and the stage random vibrations. Finally, in the development of the CAD scheme, selecting optimal and robust feature set is a critically step, as the image features may directly determine the final performance of the entire scheme. Since the effectiveness of the features varies according to different applications, we should assess the classification accuracy of these features under the high throughput scanning condition.

Chapter 4: The feasibility of the automatic detection of analyzable metaphase chromosomes

4.1 Background

During the scanning process, the high throughput microscopic scanner generates a large number of images with high resolving power. However, only a few regions of interest (ROI) contain analyzable metaphase chromosomes. Therefore, a computer aided detection (CAD) scheme is necessary to automatically identify ROIs depicting analyzable metaphase chromosomes [28-30, 78].

4.2 Experimental methods

In this study, we investigated the feasibility of integrating the high throughput image scanner and the CAD scheme. During the investigation, a number of 9 specimens were first selected by the experienced clinicians. Among these specimens, 6 were acquired from the blood samples, and the others are from the bone marrow samples. These specimens were processed using the standard methods. For each specimen, the analyzable metaphase chromosomes were visually selected under the same condition of routine clinical practice.

These selected specimens were then scanned using the high throughput image scanner. During the scanning, the CAD scheme was applied to detect and identify ROIs that may contain analyzable chromosomes. To improve the efficiency, the CAD scheme is divided into two processing modules: the on-line and off-line processing modules. The on-line module quickly follows the scanning processing to detect and save ROIs containing suspiciously analyzable chromosomes. After the scanning is finished, the off-line CAD module is used to process each saved image section to further detect the analyzable ROIs.

The flowchart of both on-line and off-line CAD schemes is illustrated in Fig 12. These schemes are composed of 4 different steps. The suspicious chromosome region is first separated and labeled, using a region growth and labeling algorithm. Then, a set of rules based on size and circularity are applied to discard the labeled regions under or above the previously determined threshold. After that, several image features are computed on the remained regions, which are detailed as follows [28, 29]:

1) Number of the labeled regions [29]: This feature is defined as the number of the isolated "chromosomes" depicted on the entire image.

2) Average intensity of each labeled region [79]: This feature is the average value of the pixel intensity for each separated "chromosomes" contained on the obtianed image.

3) Area of each labeled region [29]: It is computed by counting the number of the pixels for each labeled "chromosome" contained in the image.

4) Circularity of each region [80]: In this feature, the gravity center of each labeled "chromosome" is first determined. Next, the CAD creates a circle with the same size as the labeled region. Then, the method estimates the size of labeled region which is overlapped size with the equivalent circle. The ratio between the overlapped size (A_o) and entire size of the region (A) is defined as the region circularity: A_o / A.

5) The radial length to the center [29]: For this feature, the global gravity center (x_g, y_g) of all the labeled regions is calculated. Then the method determines the distance

between the gravity center (x, y) of each label region and global gravity center (x_g , y_g)., which is defined as the radial length to the center.

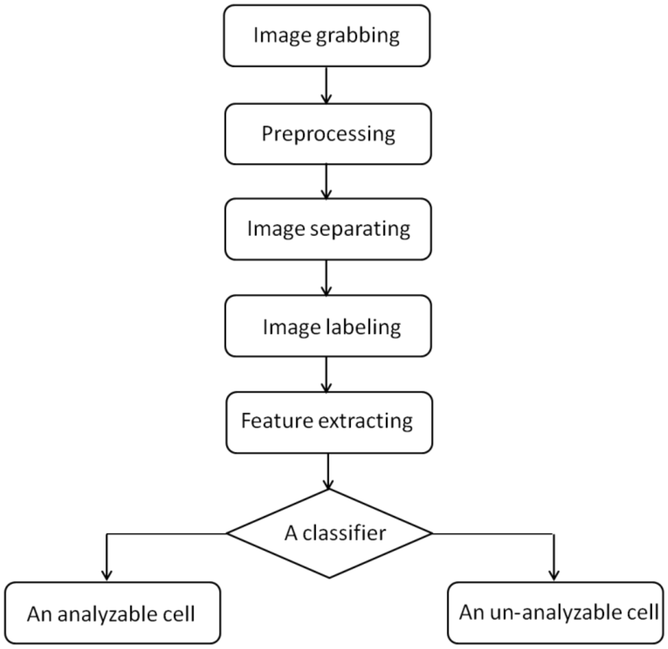

Figure 12: The flow chart of the CAD scheme program [29]

The offline CAD scheme extracts all of the above five features. For the online CAD scheme, only first three features are used to improve the algorithm efficiency.

In the fourth step, based on these calculated features, the scheme identifies the analyzable metaphase chromosomes. For each feature, a range was first determined based on the clinician's experience, within which the image will be consider as analyzable chromosome. The captured image will be discarded if the any one of the calculated features are outside the pre-determined range. The selected results are visually confirmed by a panel of three clinicians independently, to detect and discard the false-positive chromosomes.

4.3 Experimental results

Figure 13-14 shows several analyzable chromosomes acquired by both area scanning and TDI line scanning detectors. Fig 13 (a) was acquired by the area scanning camera, which shows clear chromosomal band patterns with high contrast. Fig 13 (b), however, was captured by the TDI detector. Fig 13 (b) demonstrates clear chromosomal band patterns that are adequate for clinical interpretation, although they provide less contrast as compared to the image in Fig 13 (a). The relatively low contrast may be attributed to multiple factors including TDI noise. Experimental results demonstrate the potential of the high speed TDI scanning, online processing technique for clinical applications.

The image contrast and sharpness will decrease more significantly if the cell chromosomal band patterns deteriorate, as demonstrated in Fig 14. The image acquired manually in Fig 14 (a) depicts very clear chromosomal band patterns with high contrast. However, the auto-captured result in Fig. 14 (b) shows fuzzy chromosomal band patterns which do not meet the requirement for clinical interpretation. Generally, the sharpness and contrast of the auto-captured image by the TDI line scanning camera is inferior to the manual-captured image by the area camera, but in most situations, the auto-captured results are acceptable for clinicians.

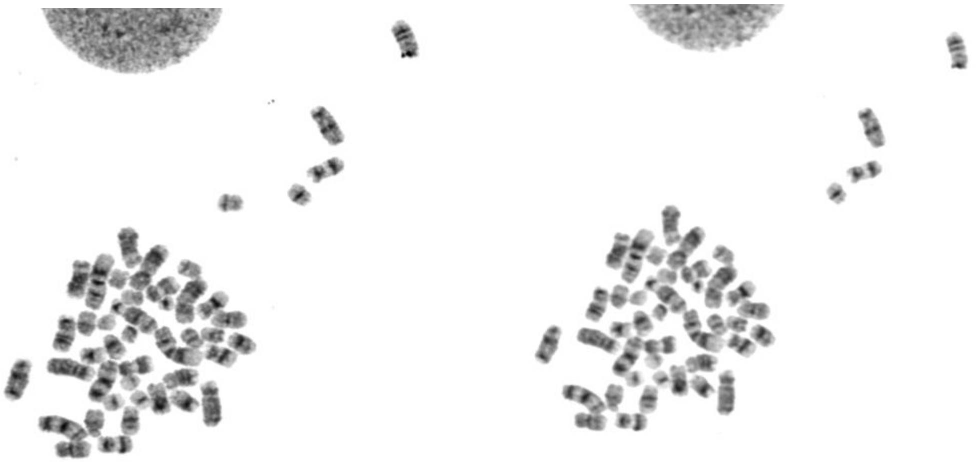

(a) (b)

Figure 13: Digital microscopic images of an analyzable cell

(a): The cell is acquired manually from a bone morrow slide, by an area scanning camera with a 100× objective. (b): The cell is acquired from the same slide, by a TDI line scanning camera with a 100× objective.

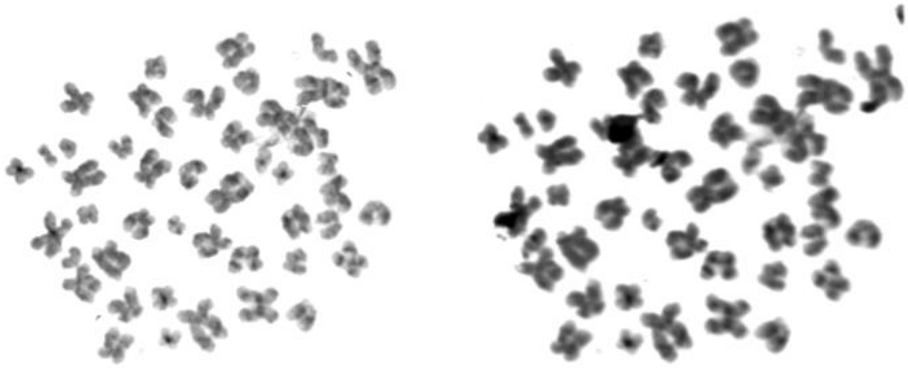

(a) (b)

Figure 14: An example of image contrast and sharpness deterioration due to the off-focusing effect

(a): Digital microscopic image of an analyzable cell which is acquired manually from a bone morrow slide, by an area scanning camera with a 100× objective. (b) Image of the same cell acquired by a TDI line scanning camera with a 100× objective.

The experimental results of blood specimens are demonstrated in Table 1. The clinicians initially selected 3 to 4 analyzable metaphase cells in these six specimen slides for their diagnostic purpose. However, a large number of image frames were captured (ranging from 518 to 3696 with an average of 1954 frames in each specimen) when scanning and applying the online CAD scheme to the six blood specimens. The large number of the on-line results can be attributed to the low specificity of the on-line CAD scheme. Real time scanning requires the high efficiency and high sensitivity of the on-line CAD, but this occurs at the cost of low specificity. After applying the off-line CAD scheme on the scanned results, the clinicians finally confirmed that 2 to 46 ROIs depicting analyzable metaphase chromosome cells for the diagnosis. These results reveal that our scanning system can select more analyzable cells in five out of six blood specimens.

Analyzing bone marrow specimens is typically more difficult than analyzing blood specimens. In the experiment, the clinicians initially selected 10, 9, 10 analyzable cells from three bone marrow specimens. After conducting the automated scanning on these slides, the offline CAD scheme ultimately selected 80, 73, 20 ROIs with “analyzable cells”. Finally, clinicians confirmed 50, 22, 9 analyzable ROIs. Among these results, 9, 7, and 5 ROIs are matched with the initially visual selection, and 41, 15 and 4 analyzable ROIs are missed in visual searching. On the other hand, the scheme selected 30, 51, and 11 ROIs in which the clinicians considered as un-analyzable cells, which is larger than the corresponding results of blood specimens. The relatively high false-positive cell numbers can be attributed into multiple factors including image quality degradation by using TDI scanner as compared to the still-acquired images. In general, although the further improvement on CAD performance in reducing "false-positive" selection is needed in our future studies, experimental results demonstrate the potential of high speed TDI scanning and CAD pre-screening for clinical applications.

Factually, clinicians can also find as many analyzable cells as CAD scheme does. However, due to the time and cost restriction, they usually find only about 3 to 5 analyzable metaphase cells per slide, although obtaining more analyzable metaphase cells can significantly improve the accuracy of the diagnosis. Using high speed TDI scanning, the tested system can provide more analyzable images for clinicians, to enhance their diagnostic accuracy with no additional costs. The results of the experiment reveal that the automated scanning system could help clinicians to achieve more accurate diagnosis while avoiding the tediously visual searching process under the microscopes.

Table 1: Comparison between the numbers of visually selected analyzable cells using microscopes and the automated scanning system with CAD

Blood Specimen	Cells selected in initially visual searching	Cells selected by on-line CAD module	Cells selected by off-line CAD module	Analyzable cells visually confirmed among CAD-selected cells
1	3	1262	33	28
2	3	3696	50	46
3	3	1618	39	32
4	4	2583	10	9
5	3	518	34	19
6	3	2046	4	2

4.4 Discussion

High throughput scanning microscopy is an important technique for the diagnosis of genetic diseases. However, there is no investigation on the performance comparison between the new scanning method and the conventional scanners. In this paper, a total of 9 slides from five patients were used to test the system performance. During the scanning, an online program was used to determine whether the acquired image to be saved. Due to the high specificity caused by the strict time and sensitivity requirement of the online program, an offline program was necessary to further select the analyzable metaphase cells within the online results from the scanning process. The results demonstrate that the investigated system can identify more analyzable metaphase cells than clinicians do in six out of the seven slides. These cells are presented with acceptable specificity and adequate contrast and sharpness for further interpretation.

As compared to the traditional method, the new high throughput scanning system has two principal advantages. First, the new system can offer the high resolution images directly for clinicians or the computer aided processing, while the conventional scanner only provide the location of the possible analyzable metaphase cells, requiring clinicians to recapture and confirm the image in high resolution [27]. Second, the new system has the potential high efficiency of the slide scanning. Due to the superior TDI line scanning mechanism, the high throughput scanning system can acquire the images when the stage is moving, while the conventional scanner must capture the image when the stage is stationary to avoid serious image blurring. The highly efficient TDI line scanning may provide more analyzable metaphase cells for clinicians with no additional workload, which can substantially enhance the diagnosis accuracy because the accuracy is strongly related to the number of analyzable metaphase cells.

Although the initial testing of the system provides an encouraging result, this study is preliminary. The number of the specimens is limited, and the CAD scheme should be improved to increase the detecting accuracy for the bone marrow analyzable chromosomes. In spite of these limitations, we believe that the high throughput scanning technique may be meaningful for improving the diagnostic accuracy in the future.

Chapter 5: Impact of the optical depth of field on cytogenetic image quality

5.1 Background

In digital pathology, high throughput digital microscopic image scanning is a fundamental technique for the diagnosis of various diseases [1-4, 20]. For this technique, however, one of the technical challenges is to maintain the pathologic specimen in focus during the image scanning, which may affect the reliability and efficiency of the image acquisition. The off-focused images can be attributed to several different factors, including the narrow depth of field (DOF) of an optical imaging system, and the impact of mechanical drifting and random vibrations of a scanning stage. These factors are often unavoidable even when using the high precision moving stages, which may blur the scanned images. Although the researchers pursue to develop a precise focusing trace technique for the high quality microscopic image scanners, understanding the impact of the DOF on the scanned digital images can help balance the tradeoff between the scanning efficiency and image quality, which is important and necessary in the design of cost-effective digital microscopic image scanners.

This study aims to systematically investigate the tolerance level of off-focusing in diagnostic cytogenetic images. We first analyzed optical DOF of a microscope in theory. Then, we measured the DOF using a standard resolution target, under objective lenses with different magnification powers and numerical apertures (N.A.). After that, cytogenetic images from different clinical specimens were acquired and analyzed using the same microscope equipped with a 60× (dry, N.A. = 0.95) and a 100× objective lenses (oil, N.A. = 1.25), respectively. The chromosomal band sharpness was subjectively assessed to investigate the image quality deterioration when the metaphase or interphase cells were captured at in-focused and off-focused states. The detailed experimental procedures and image quality analysis results are presented in this article.

5.2 Optical depth of field (DOF): Definition and calculation

5.2.1 Geometric DOF

The DOF of an optical system is defined as the axial range in the object space where the quality degradation of the imaged object is undistinguishable [56]. There are two different types of DOF which contribute to the system DOF: geometric DOF and diffractive DOF. The geometric DOF is the axial range in the object space within which the blurred spot on the image space cannot be distinguished by the detector, as illustrated in Fig 15.

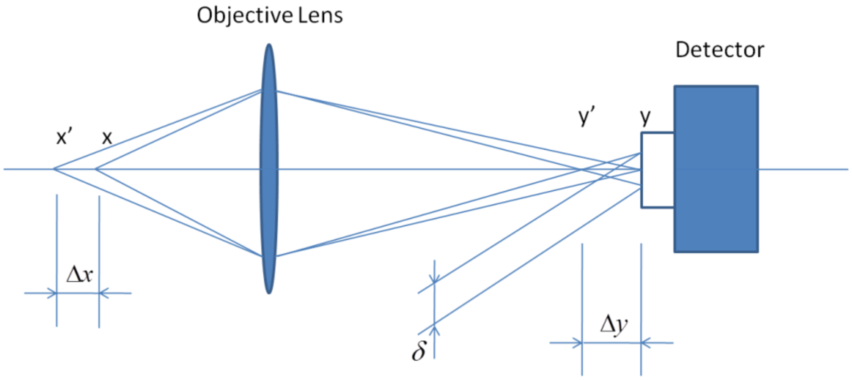

Figure 15: The demonstration of geometric DOF

In Fig 15, x, x' are objective points, y, y' are the corresponding image points. Δx, Δy are the distance between x, x' and y, y' respectively. δ is the diameter of the blurred circular region. The detector has a pixel size of p µm.

In the figure, the objective point x is placed in the object side of the objective lens and the point x is imaged as a distinct point at point y on the other side. When the object point moves a distance of Δx towards the lens, the image point will also move a distance of Δy further to the lens on the other side. However, if the camera is not moved, a blurred circular region will be detected instead of a distinctive point. According to the Nyquist sampling theorem, the circular region will not affect the final image quality if the diameter of the circular region is smaller or equal to twice the pixel size on the detector [81]. Therefore, the diameter of the blurred circular δ must be smaller or equal to twice the pixel size:

$$\delta \approx 2\Delta y \bullet \alpha' \leq 2p \tag{5-1}$$

where Δy is the moving distance, and α' is the aperture angle of the light path on the image space.

Given that the axial magnification relation between the moving distance in the image space (Δy) and object space (Δx) is:

$$\frac{\Delta y}{\Delta x} = \frac{1}{n}\beta^2 \tag{5-2}$$

where β is defined as the magnification of the light aperture angle, and n is the refractive index of the object space. Substitute (2-2) into (2-1), we have [56, 82]:

$$\Delta x = \frac{n\Delta y}{\beta^2} = \frac{np}{\beta^2\alpha'} = \frac{np}{\beta N.A.} \tag{5-3}$$

Note that N.A. is numerical aperture of the objective, which is [82]:

$$N.A. = n\alpha \tag{5-4}$$

In the formula, α is the aperture angle of the object space.

If the object point moves further, the same Δx is achieved through the similar method. Thus the final geometric field depth is [56]:

$$\Delta x = \frac{2np}{\beta N.A.} \tag{5-5}$$

5.2.2 Diffractive DOF

The diffractive DOF is based on the light intensity distribution along the optical axis. For the object point *x*, the axial light intensity distribution of the corresponding image point *x'* is can be approximated as a Sinc function centered at *x*. The detected image point *x'* will be considered as acceptable if the intensity is larger than 80% of the maximum. Accordingly, the corresponding moving range on the object space is defined as the diffractive DOF, which can be calculated as follows [56, 82]:

$$\sigma = \frac{n\lambda_0}{N.A.^2} \qquad (5\text{-}6)$$

Where *n* is the refractive index in object space, N.A. is the numerical aperture of objective lens, and λ_0 is the wavelength of the illumination. In this investigation, the wavelength is assumed to be 0.550 μm.

5.2.3 The total DOF of the optical system

For a realistic microscopic imaging system, both geometrical and physical effects exist simultaneously. The calculation of the total DOF has been thoroughly discussed in the last several decades [56, 83-85]. Although a standard method of determining the total DOF has not been established to date, the following method is the most recommended to compute total DOF, which is the sum of the diffractive and geometric DOF [56, 83-85]:

$$\sigma = \frac{2np}{\beta N.A.} + \frac{n\lambda_0}{N.A.^2} \qquad (5\text{-}7)$$

5.3 DOF measurements

The DOF of the tested microscopic system can be investigated experimentally by measuring the contrast at a series of in-focused and off-focused positions. The DOF is estimated by determining the range where the contrast is larger than 80% of the maximum [86-90].

During the experiment, the DOF range was estimated separately when applying 60× (dry, N.A. = 0.95) and 100× (oil, N.A. = 1.25) objective lenses. The experiment is divided into three steps. First, we measured the modulation transfer function (MTF) to determine the spatial frequency for DOF estimation. MTF was accomplished by measuring the image contrast at a series of discrete spatial frequencies from 0 to the system resolving limit. The measured contrast values are normalized for the final MTF curve. Second, according to the MTF curve, the frequency where the contrast drops to half of the maximum is selected to estimate the DOF. Finally, at the selected frequency, the contrast was measured to determine the system DOF.

In order to determine the spatial frequency of DOF estimation, the MTF was first measured using standard resolution targets. Two different bar pattern targets were used in the experiments. The USAF1951 resolution target (USAF1951, Edmund Optics, New Jersey, U.S.A.) contains different bar patterns with discrete spatial frequencies up to 645 lp/mm. Another target with maximal frequency of 2000 lp/mm (MRS-4, Geller Microanalytical Laboratory, Massachusetts, U.S.A) was also applied to measure the contrast at spatial frequencies higher than 645 lp/mm.

For each microscopic objective lens, the MTF was estimated through measuring the contrast at different spatial frequencies from 0 to the resolving limit. In this investigated system, the pixel size of the camera is smaller than half of the resolving limit. Therefore, the spatial resolution was determined by the following formula [56]:

$$\sigma = \frac{0.61\lambda_0}{N.A.} \tag{5-8}$$

where N.A. is numerical aperture of the objective lens, and λ_0 is the wavelength of the illumination. In this investigation, the wavelength is assumed to be 0.550 μm. Thus, when using the two objective lenses with 60× and 100× magnification power, the spatial resolution calculated with Equation (5-8) is 0.353 and 0.268 μm, or 1416 lp/mm and 1863 lp/mm, respectively.

In the MTF measurement, the test target was placed on the stage. The system was manually adjusted to ensure that the target is imaged at the in-focused condition. After that, the target was captured and the contrast of each pattern on the target is calculated by the following formula [91]:

$$C = \frac{I_{\max} - I_{\min}}{I_{\max} + I_{\min}} \tag{5-9}$$

where I_{max} and I_{min} are the average maximum and minimum digital pixel values of the imaged test bar patterns at different frequencies. Based on the calculated contrasts at different spatial frequencies, the curve fitting method was then applied to create a smooth MTF curve [92]. The frequency where the MTF decreases to 0.5 was selected for the DOF estimation.

After the spatial frequency was determined, the DOF range was estimated for each objective lens. The estimation was accomplished using the above test bar pattern targets. Before the measurement, the target was placed on the stage and the in-focused position was visually adjusted and determined. Then, starting from the in-focused position, the stage was gradually moved up and down with a series of steps. At each position, the target image was obtained by the detector and the contrast of the image is computed by Equation (5-9). Finally, the calculated contrast was curved as a function of focusing positions. The range where the contrast is larger than 80% of the maximum is determined as the system DOF estimation [86].

5.4 Results

5.4.1 DOF theoretical results

Table 1 tabulates the theoretical results calculated by Equation (5-7) in *Section 5.2.1*. The one-dimensional pixel size of the CCD detector used in the investigated system is 7 μm. When applying a dry 60× (N.A. = 0.95) microscopic objective lens and an oil-emerged 100× (N.A. = 1.25) objective lens, the computed system DOF are 0.855 and 0.703 μm, respectively. As expected, using higher magnification power results in smaller DOF.

Table 2: The depth of field of our microscopic scanning system equipped with two different objective lenses

Magnification	Type	Refractive index of object side	Numerical aperture (N.A.)	Detector pixel size	Geometric DOF	Diffractiv e DOF	System DOF
60×	Dry	1	0.95	7 μm	0.246 μm	0.609 μm	0.855 μm
100×	Oil	1.515	1.25	7 μm	0.170 μm	0.533 μm	0.703 μm

5.4.2 DOF experimental results

Two example images of the USAF1951 resolution test bar target are demonstrated in Fig 16 (a) and (b), which were captured at the focal position and 3.5 μm away from the focal plane of an oil-emerged 100× objective lens, respectively. The image in Fig 16 (b) was acquired at the off-focused state, as the resolution patterns are obviously blurred. Fig 17 illustrates two measured MTF curves of the microscope when using two 60× and 100× objective lenses separately. The measured curves reveal that the MTF decreases approximately to the half maximum value at 456 lp/mm and 645 lp/mm, respectively. These spatial frequencies were therefore utilized to estimate the system DOF when the 60× and 100× objective lenses were applied.

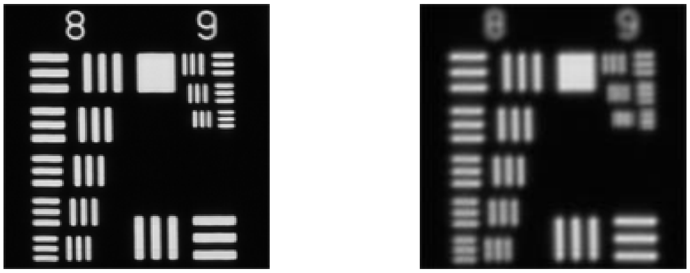

(a) (b)

Figure 16: Sample images of an USAF 1951 standard resolution target

The target was captured by a 100× (oil, N.A. = 1.25) objective lens, at (a) in-focused position (b) 3.5 μm away from the focal plane.

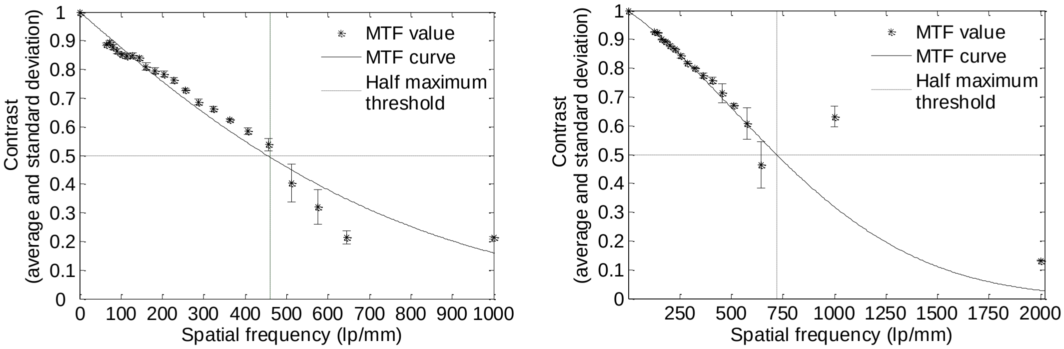

(a) (b)

Figure 17: The MTF curve measured for the tested microscope using (a) 60× (dry, N.A. = 0.95) objective lens and (b) 100× (oil, N.A. = 1.25) objective lens

The “half-maximum” contrast measurements, plotted as a function of focusing positions, are shown in Fig. 18 (a) and (b), when the 60× and 100× objective lenses were used, respectively. For each curve, the contrast value reaches the maximum at the in-focused position (0 at x-axis), and decreases as the target is moved away from the in-focused position. As mentioned previously, the DOF can be estimated as the range where the contrast is higher than 80% of the maximal value [86]. Therefore, the actually measured system DOF are 3.0 μm and 1.8 μm when applying the 60× and 100× objective lenses, respectively.

As predicted by theoretical calculations, the results reveal that the DOF decreases when increasing the N.A.. Due to the experimental restriction, the measured DOF is substantially greater than the theoretical prediction. In the experiment, we could not directly measure the size of the image spot or the axial light intensity for the geometrical and diffractive DOF separately. Alternatively, the DOF was estimated by measuring the image contrast. But the z-position where the image contrast drops to 80% of the maximum is not exactly the same position for the geometrical or diffractive DOF. In other words, theoretical computation can only be used as a reference.

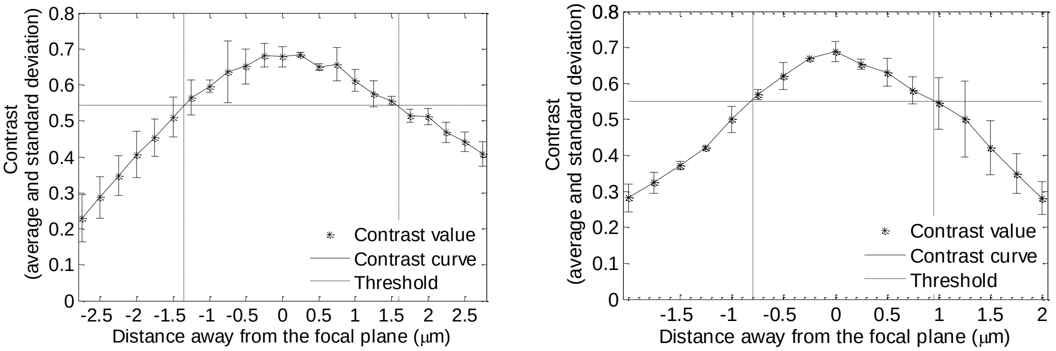

(a) (b)

Figure 18: The measured “half-maximum” contrast values versus focusing positions for the investigated microscopes when using (a) 60× (dry, N.A. = 0.95) objective lens and (b) 100× (oil, N.A. = 1.25) objective lens

5.4.3 DOF impact on diagnosis of clinical cytogenetic images

The microscopic images of analyzable cells acquired from four pathological samples including bone marrow, blood, amniotic fluid, and products of conception

(POC) are shown in Figs 19-26 as examples. Figs 19-21 are metaphase cells acquired by the microscopic system using 60× (dry, N.A. = 0.95) objective lens, and Figs 22-25 are metaphase cells acquired under 100× (oil, N.A. = 1.25) objective lens. Figure 26 illustrates an interphase cell captured under 100× (oil, N.A. = 1.25) objective lens. In each of Figs 19-21, Image (a) was obtained at the focal plane resulting in clear and sharp chromosome band patterns, which are adequate for clinical diagnosis. Image (b) was acquired 1 μm out of focus, and the band patterns are as clear as Image (a). When the cell was obtained 1.5 μm away from the focal plane, the image is somewhat blurred but still recognizable, as shown in Image (c). The band contrast decreases more significantly when the cell moves further away from the focal plane, with the band shapes becoming barely recognizable and then totally unrecognizable in Image (d) and (e), both of which were acquired 2 μm and 2.5 μm out of focus, respectively.

In Figs 22-25, the band sharpness decreases at a faster rate as compared with those shown in Fig 19-21. In Figs 22-25, Image (c) was obtained 1 μm away from the focal plane, which shows a cell containing somewhat recognizable band shapes with decreased contrast. These cells are still suitable for clinical practice. Furthermore, when the image was obtained 2 μm out of focus, the band patterns become completely unrecognizable and unsuitable for the diagnosis purposes, as illustrated in Image (e).

Fig 26 shows a typical image of an interphase cell acquired from a POC sample. This cell was processed by the fluorescence in situ hybridization technique (FISH) biomarkers. The diagnostic genome fragments are demonstrated as bright dots in the captured image. The cell in Fig 26 (a) was imaged at the focal plane, and shows two clear green dots on the blue background. When the cell was moved 1 μm away from the focal plane, as shown in Fig 26 (b), the dots become smaller but still recognizable. However, the dots disappear completely in Fig 26 (c), which was captured 2 μm out of focus.

In summary, these experimental and observation results agree with the measured DOF ranges demonstrated in *Section 5.4.2*. For the investigated microscopic system, the range of DOF is approximately 3.0 μm and 1.8 μm when applying 60× (dry, N.A. = 0.95) and 100× (oil, N.A. = 1.25) objective lenses, respectively. The images acquired within DOF illustrate clearly cytogenetic features, which are adequate for the diagnosis of diseases in clinical practice. However, when the cell is moved out of the DOF range, the pathological meaning of the acquired images slowly diminishes.

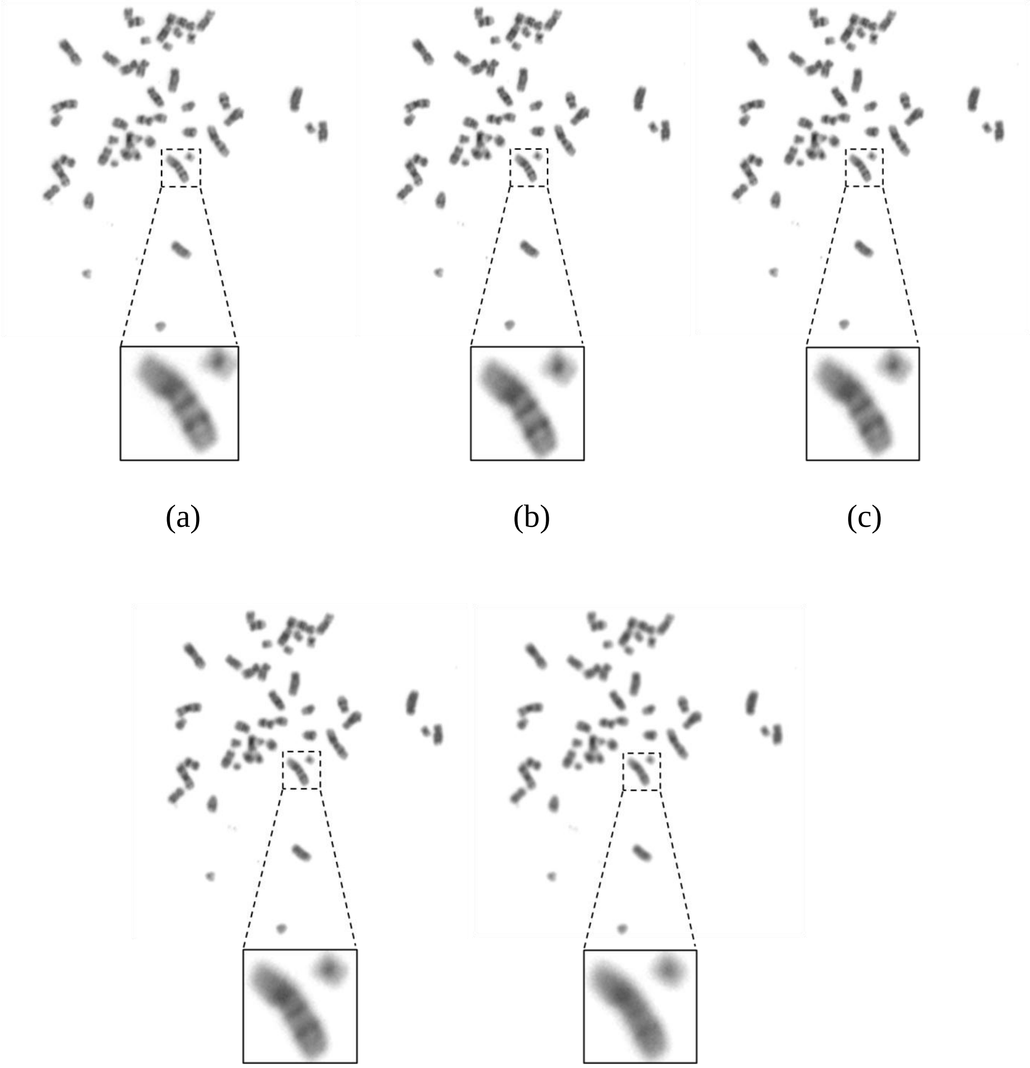

(a) (b) (c)

(d) (e)

Figure 19: Microscopic images (60×) of a clinically analyzable cell contained in a bone marrow sample

The cell was captured using a 60× objective lens (dry, N.A. = 0.95), at positions of (a) in-focused, (b) 1 μm, (c) 1.5 μm, (d) 2 μm, and (e) 2.5 μm away from the focal plane.

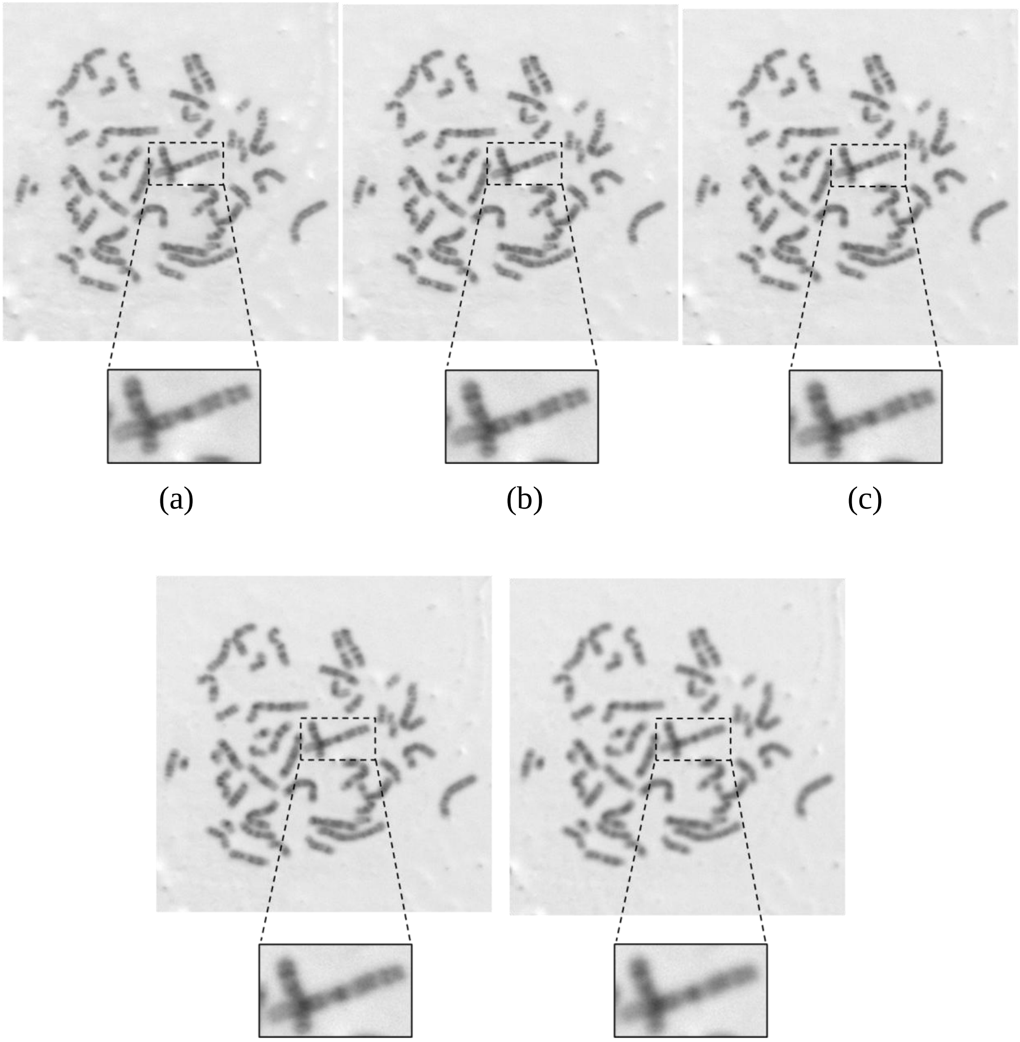
(a) (b) (c)

(d) (e)

Figure 20: Microscopic images (60×) of a clinically analyzable cell contained in a blood sample

The cell was captured using a 60× objective lens (dry, N.A. = 0.95), at positions of (a) in-focused, (b) 1 μm, (c) 1.5 μm, (d) 2 μm, and (e) 2.5 μm away from the focal plane

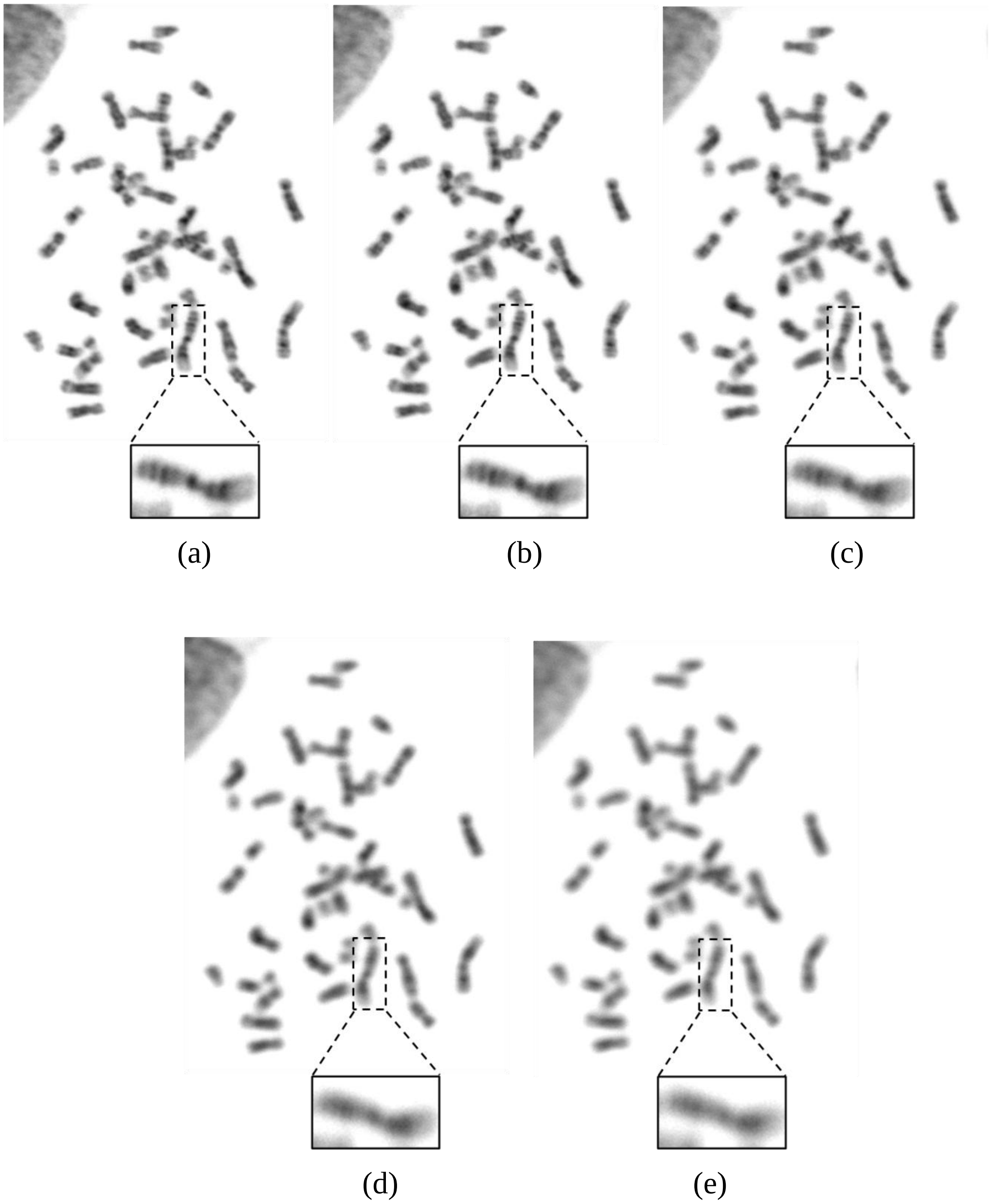
(a) (b) (c)

(d) (e)

Figure 21: Microscopic images (60×) of a clinically analyzable cell contained in a POC sample

The cell was captured using a 60× objective lens (dry, N.A. = 0.95), at positions of (a) in-focused, (b) 1 μm, (c) 1.5 μm, (d) 2 μm, and (e) 2.5 μm away from the focal plane.

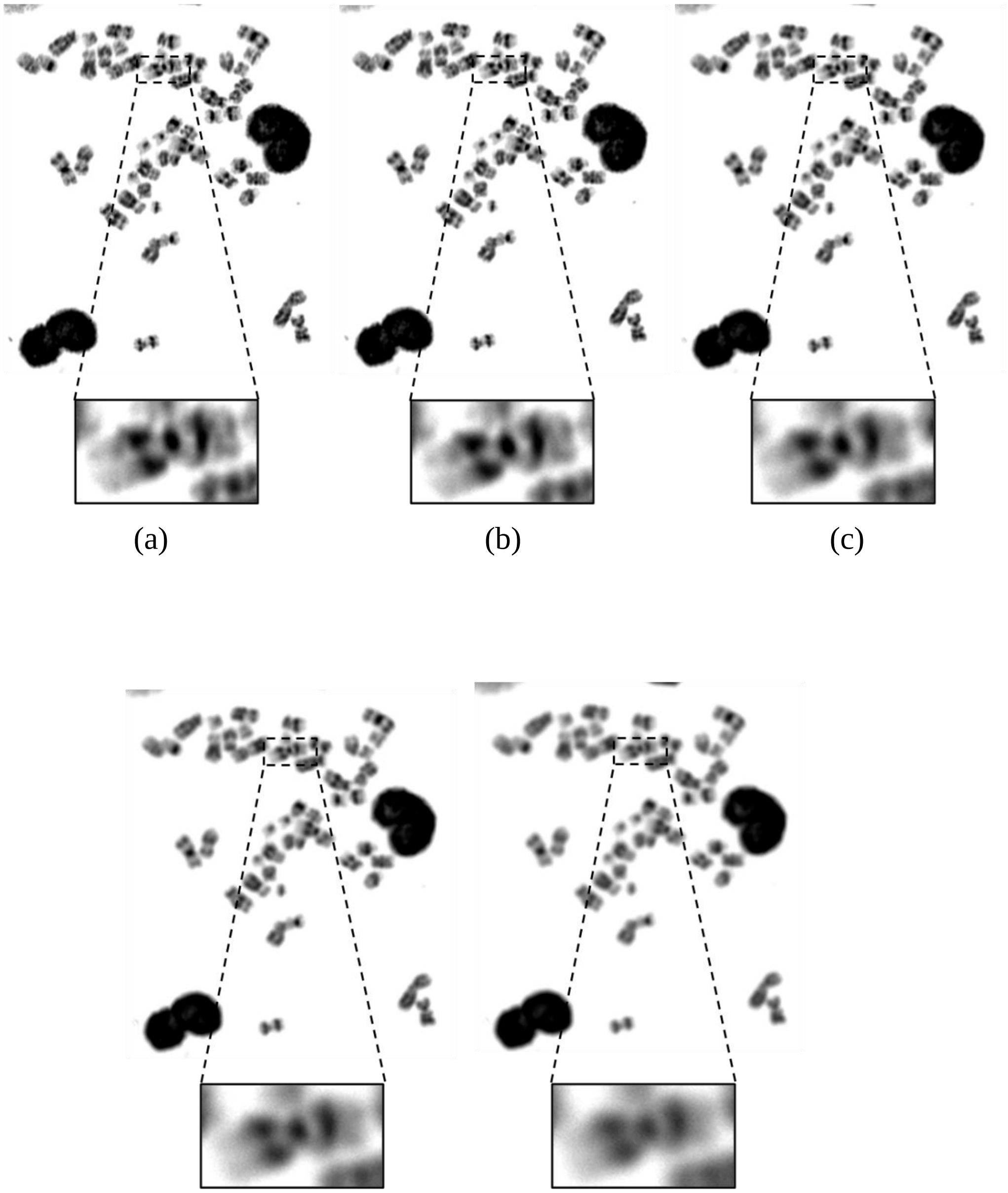

(a) (b) (c)

(d) (e)

Figure 22: Microscopic images (100×) of a clinically analyzable cell contained in a bone marrow sample

The cell was captured using a 100× objective lens (oil, N.A. = 1.25), at positions of (a) in-focused, (b) 0.5 μm, (c) 1 μm, (d) 1.5 μm, and (e) 2 μm away from the focal plane.

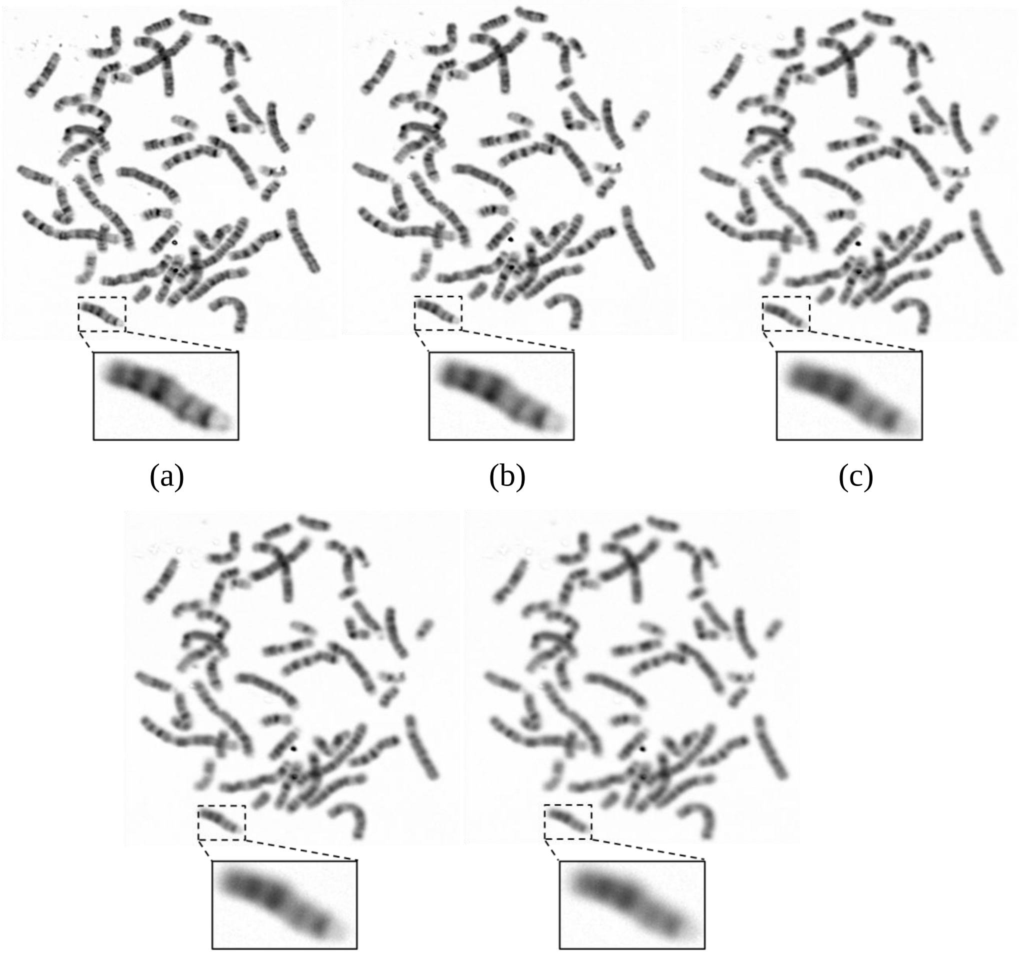
(a) (b) (c)

(d) (e)

Figure 23: Microscopic images (100×) of a clinically analyzable cell contained in a blood sample

The cell was captured using a 100× objective lens (oil, N.A. = 1.25), at positions of (a) in-focused, (b) 0.5 µm, (c) 1 µm, (d) 1.5 µm, and (e) 2 µm away from the focal plane.

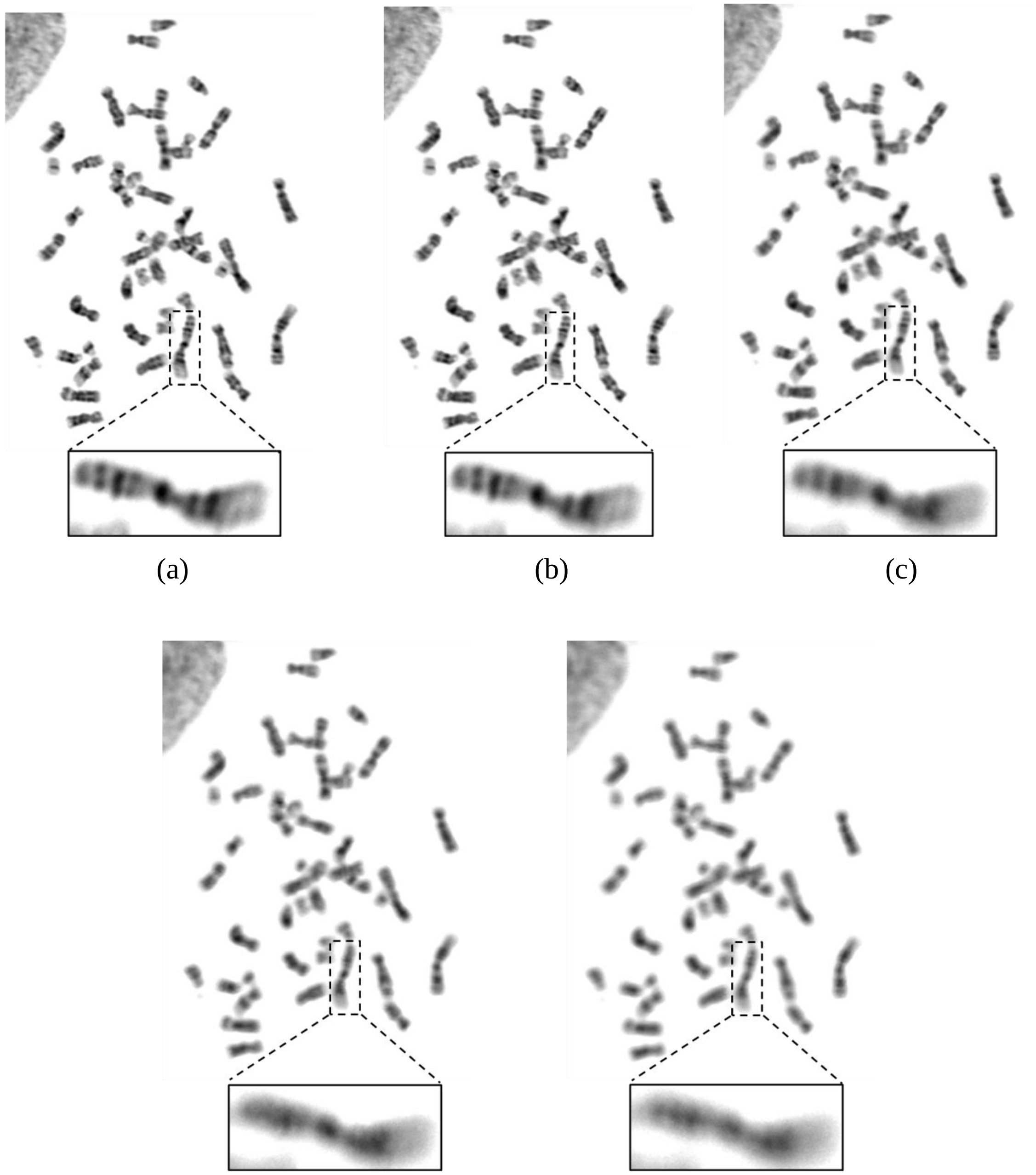

(a) (b) (c)

(d) (e)

Figure 24: Microscopic images (100×) of a clinically analyzable cell contained in a POC sample

The cell was captured using a 100× objective lens (oil, N.A. = 1.25), at positions of (a) in-focused, (b) 0.5 μm, (c) 1 μm, (d) 1.5 μm, and (e) 2 μm away from the focal plane.

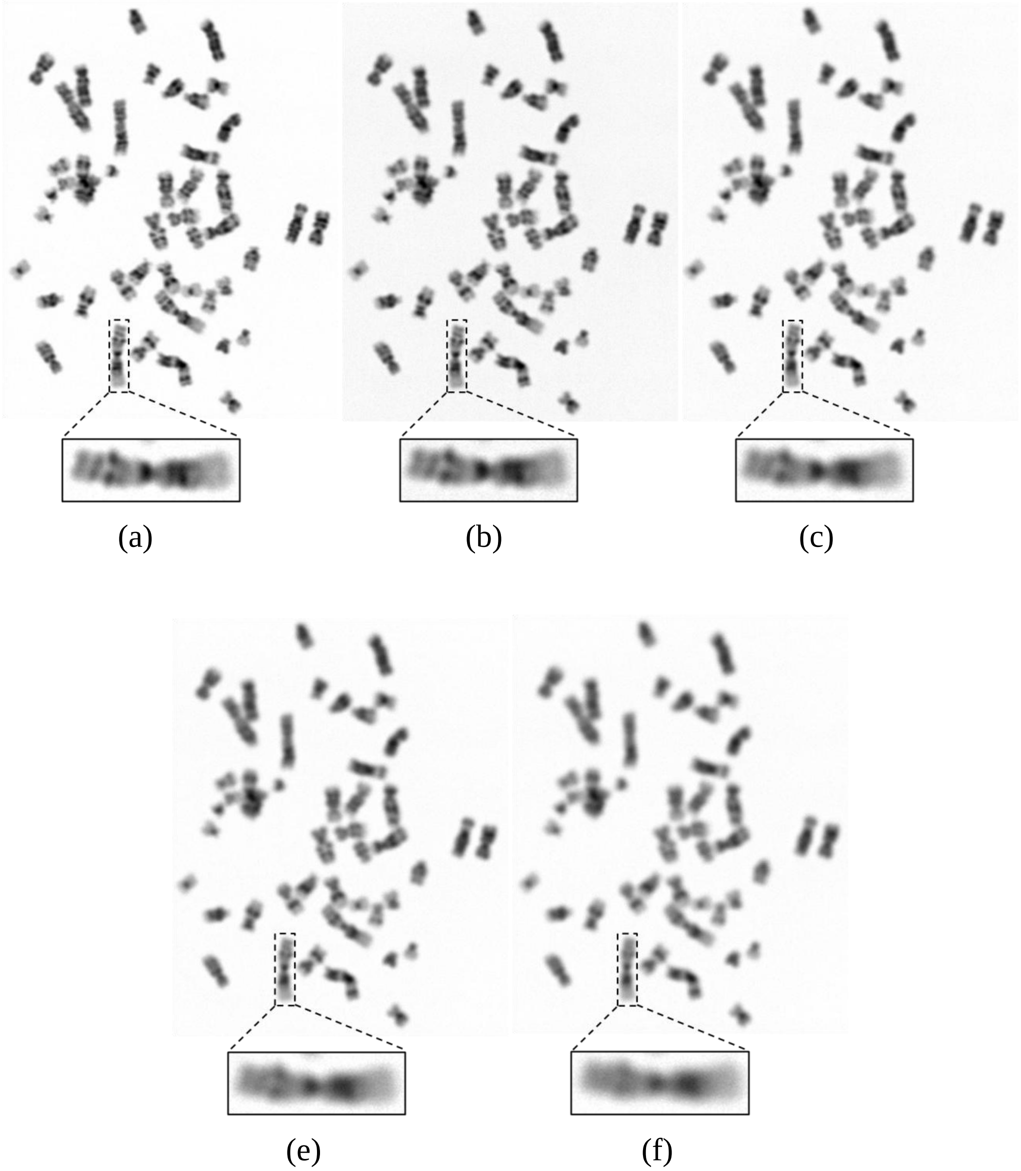

(a) (b) (c)

(e) (f)

Figure 25: Microscopic images (100×) of a clinically analyzable cell contained in an amniotic fluid sample

The cell was captured using a 100× objective lens (oil, N.A. = 1.25), at positions of (a) in-focused, (b) 0.5 μm, (c) 1 μm, (d) 1.5 μm, and (e) 2 μm away from the focal plane.

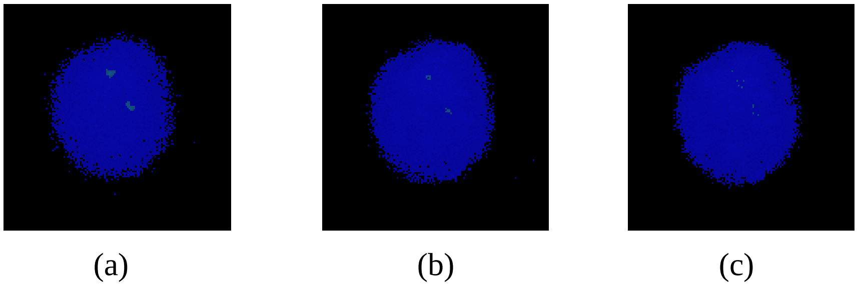
(a) (b) (c)

Figure 26: Microscopic fluorescent in situ hybridization (FISH) images of a clinically analyzable interphase cell contained in a POC sample

The chromosomes of interest are marked as the fluorescent dots, and the cell is captured by the system under investigation using 100× objective lens (oil, N.A. = 1.25), at positions of (a) in-focused, (b) 1 μm, and (c) 2 μm away from the focal plane.

5.5 Discussion

In clinical practice, the consistent chromosome abnormalities have been used to diagnose some serious diseases [1-3]. In order to diagnose these diseases, clinicians in the cytogenetic laboratories need to obtain in-focused images with clear and sharp chromosome bands, as the blurred bands in the digital images may result in misdiagnosis. For instance, among the karyotyping of metaphase chromosomes, 21st trisomy is an important diagnostic evidence of the down's syndrome [2]. Since the size of 21st chromosome is shorter than the others, these chromosomes can be easily misunderstood as small debris in the off-focused state. In another example, Philadelphia translocation t(9;22)(q34;q11), a reciprocal translocation between 9th and 22nd chromosome, is highly related to chronic myelogenous leukemia [3]. Clinicians need to locate the region q34 in the 9th chromosome and q11 in the 22nd chromosome, by analyzing the band shape and counting the bands. However, if the image is off-focused, the band patterns become fuzzy, hence these two different regions (q34 and q11 in the

9th and 22nd chromosomes) are extremely difficult to distinguish, which might cause false positive or false negative results.

In order to ensure that the imaged chromosome bands are adequately sharp for the diagnosis, many current microscopic systems perform the auto-focusing operation repeatedly for each useful cell [5, 21, 25]. However, these scanning systems are often inefficient because the auto-focusing operation is quite time consuming. Therefore, in order to balance the trade-off between the scanning efficiency and the image quality for a clinical diagnostic purpose, we need to analyze how the DOF impacts on the acquired chromosome bands. To the best of our knowledge, no similar studies have been previously conducted and reported to investigate the tolerance level of out-focusing in automatically scanning pathological specimen slides.

In this study, we first computed DOF using a well-recognized theoretic model of an optical image system and then measured DOF of the same optical system using a standard test bar pattern target. Our results showed that the experimentally measured DOF was substantially greater than that computed by the theoretic model, which suggests the importance of using well-designed experiments to assess and measure the actual DOF of an optical system (e.g., a microscope). In addition, we also analyzed DOF (or off-focusing tolerance level) by obtaining cytogenetic images under the 60× (dry, N.A. = 0.95) and 100× (oil, N.A. = 1.25) objective lenses. Four types of commonly cytogenetic specimens acquired from bone marrow, blood, amniotic fluid, and products of conception (POC) in our cytogenetic laboratory were tested and analyzed in this study. Although the quality (i.e., sharpness and/or contrast of the metaphase chromosomes) of the images acquired from these four types of specimens varies, our experimental results demonstrated that the chromosomal bands remained analyzable if the cells were captured within the range of 1.5 or 1.0 μm away from the focal plane when using the two 60× or 100× objective lenses, respectively. Comparing the experimental results acquired from using these two objective lenses, one could find that the microscopic system's DOF would be wider if low magnification objective lenses were utilized. However, the resolution of the pathological features also decreased. In summary, the results support the feasibility of developing the automated microscopic or pathological image scanners with limited power of auto-focusing, which will significantly increase the efficiency of image scanning as well as the efficacy of digital pathology.

Although the results of this preliminary study are encouraging, there are several limitations. First, we did not consider the effect of the chromosome thickness [93]. Second, a simple DOF measurement was used, and we did not test whether applying the new contrast calculation methods proposed recently could achieve more accurate results [94-98]. Third, we did not test and discuss the DOF of the human eye, which is also an important factor affecting subjective evaluation of the cytogenetic image qualities [99, 100]. Hence, a more comprehensive investigation is under way from which we hope to acquire better knowledge about the designing trade-off parameters to optimize the automated digital microscopic image scanning systems for cytogenetic image diagnosis and the other digital pathology applications in the future.

Chapter 6: Evaluations of auto-focusing methods

6.1 Background

High throughput scanning microscopy is an important technique for the diagnosis and treatment of genetic related diseases [1, 3, 5, 20]. To make this technology clinically acceptable, obtaining the in-focused high resolution images is critically important, as the blurred images may directly affect the diagnostic accuracy. Therefore, the auto-focusing technique is required for the high throughput microscopic system in the clinical practice.

During the last twenty years, substantial research efforts have been devoted to the development of reliable auto-focusing techniques for automated digital microscopes and other optical imaging applications [101-107]. Since the performance of the auto-focusing operation heavily depends on the selection of the auto-focusing function [108-111], a focusing function that performs well for the digital camera might not be selected as the optimal function for the digital scanning microscope [108]. Recently, some researchers have investigated and compared several different auto-focusing techniques for scanning a number of specific pathological specimens acquired from blood smear, pap smear, tuberculosis, or fluorescent samples [110, 112-114]. However, these researches are not specifically designed for the clinical specimens (i.e. blood or bone marrow) used in the pathological metaphase chromosome analysis.

In this study, we investigated and compared a number of different auto-focusing methods when they were applied to acquire metaphase chromosome images from bone marrow and blood specimens. The optimal auto-focusing method is selected and recommended based on the experimental results. The details of our experimental methods and results are presented as follows.

6.2 Auto-focusing functions: Definition and introduction

6.2.1 The definition of the auto-focusing function

Auto-focusing function is a function which can estimate the sharpness or contrast of the image, to determine whether the target is in-focused or not. The system can locate the focal plane by searching the maximum. For example, the estimated sharpness of Fig 27 (a) is larger than Fig 27 (b). Accordingly, the system will determine that the focusing position of Fig 27 (a) is closer to the focal plane. In fact, Fig 27 (a) was captured at the focal plane, while Fig 27 (b) was 3.75 μm away.

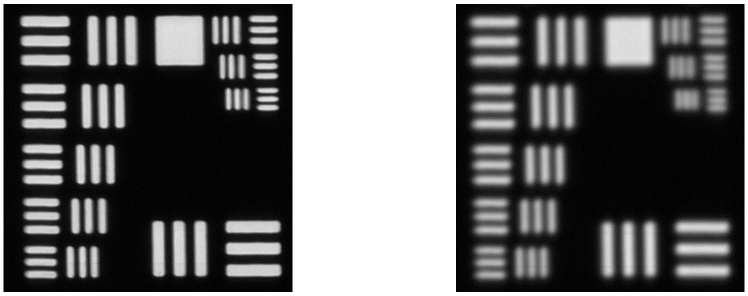

(a) (b)

Figure 27: Microscopic images of a USAF1951 standard resolution target

(a): The target was acquired at in-focused position. (b): The same target was acquired 3.75 μm away from the focal plane.

In the last several years, many auto-focusing functions have been investigated and reported. The published auto-focusing functions can be grouped into several classes including but not limited to: i) image gradient [104, 109-111], ii) histogram or contrast [109-111], iii) statistical measurement (e.g. correlation) [105], iv) wavelet transform [111, 115, 116], and v) discrete cosine transform [107].

In this study, we tested five typical methods selected from group i), ii) and iii), which are Brenner gradient, histogram range, threshold pixel counting, Vollath F5, and variance [104-106, 108, 109]. These methods have been used for a variety of biomedical specimens including fluorescent sample, blood smear, pop smear, and tuberculosis [110, 112-114]. The concepts of these functions are briefly described in the following sections.

6.2.2 Auto-focusing functions: Brenner gradient

This function is based on the fact that the intensity gradient of the acquired image will decrease when the cell is placed away from the focal plane. For example, Fig 28 (a) and (b) are the microscopic images of the 456 lp/mm pattern of the USAF1951 resolution target in Fig 28 (a) and (b), which were obtained at the focal plane and 3.75 µm away. When fixing the row value $y = 50$, the intensity variance over the x direction are plotted in Fig 28 (c) and (d). The intensity decreases and increases very sharply when the target was in-focused, but the intensity varies much smoothly when image was off-focused. The variance can be estimated by the Brenner gradient function.

For each pixel on the captured image, Brenner gradient function calculates the square of the difference between the two neighbors of the pixel, and then adds them together using the following equation [104]:

$$F = \Sigma_{x,y}(i(x+1,y) - i(x-1,y))^2 \tag{6-1}$$

with $|i(x+1,y) - i(i-1,y)| > \alpha$, where i(x, y) is the intensity at pixel (x, y), α is the threshold of the intensity difference.

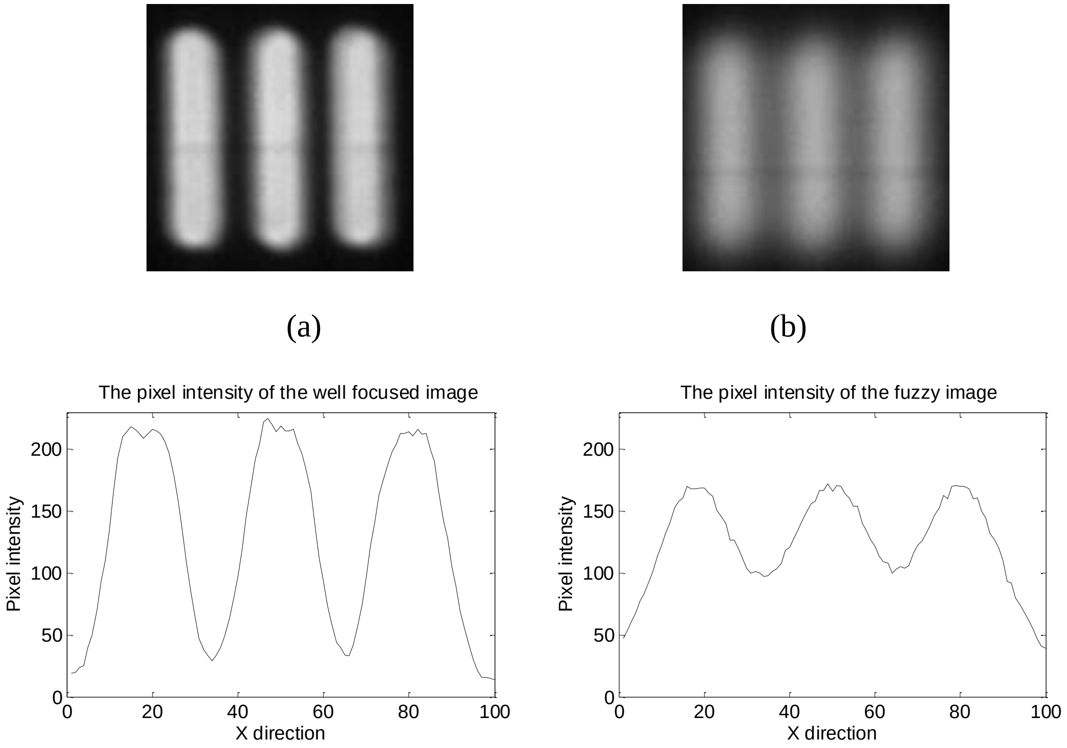

(a) (b)

(c) (d)

Figure 28: The microscopic images of the 456 lp/mm pattern of the USAF1951 standard resolution target

The target was acquired at (a) in-focused position fluorescent (b) 3.75 μm away from the focal plane. (c) and (d) illustrate the one direction intensity variance of (a) and (b) by fixing *y* = 50.

6.2.3 Auto-focusing functions: Histogram range

When the target is obtained inside or outside the depth of field (DOF) range, the histogram of the acquired images will also be changed. Fig 29 (a) shows the histogram range of Fig 28 (a), which is the image of the 456 lp/mm resolution patterns acquired at the focal plane. The range in Fig 29 (a) is obviously larger than the histogram range of Fig 29 (b), which is the result of the same pattern captured at 3.75 μm away. Therefore, we can measure the image sharpness by calculating the histogram range, which is defined as the difference between the maximum and minimum pixel intensities measured on the acquired image. Let N_k be the number of pixels with intensity k (0≤ k ≤255 for the 256 level grayscale images), which can be written as [109]:

$$F = \max(k \mid N_k \neq 0) - \min(k \mid N_k \neq 0) \tag{6-2}$$

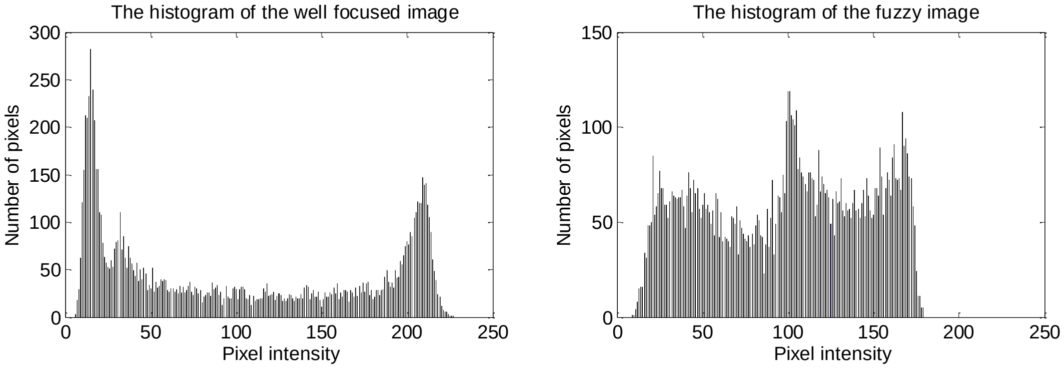

(a) (b)

Figure 29: The histogram of the 456 lp/mm pattern of the USAF1951 standard resolution target

(a): The pattern was acquired at in-focused position (b): The pattern was acquired 3.75 μm away from the focal plane.

6.2.4 Auto-focusing functions: Threshold pixel counting

The Fig 29 also demonstrates that the number of the pixels with large intensity decreases when the pattern is moving away from the focal plane. Therefore, if a threshold is determined, the image sharpness can also be estimated by counting the number of the pixels below (or above) the threshold. In this investigation, the threshold pixel counting is defined as the number of pixels whose intensity is lower than a predetermined intensity (or grayscale) threshold [108]:

$$F = \Sigma_{x,y} sign[i(x,y), th] \tag{6-3}$$

where the sign function is 1 if the pixel intensity is below the threshold and 0 otherwise.

6.2.5 Auto-focusing functions: Vollath F5

Vollath F5 is defined as follows [105]:

$$F = \Sigma_{x,y} i(x,y) \bullet i(x+1,y) - MN\bar{i}^{\,2} \qquad (6\text{-}4)$$

In order to investigate the relationship between the value F and the image sharpness, the pixel intensity can be written as the sum of three different parts:

$$i(x,y) = \bar{i} + a(x,y) + n(x,y) \qquad (6\text{-}5)$$

where *i(x, y)* is the pixel intensity at *(x, y)*, $\bar{i}$ is the average intensity value, and *a(x, y)* is the intensity amplitude, which has the following property:

$$\Sigma_{x,y} a(i,j) = 0 \qquad (6\text{-}6)$$

Note that *n(x,y)* is the noise. Obviously, the sum of all the noise *n(x, y)* over the entire image is also zero.

Therefore, the intensity of the neighboring can be written as:

$$i(x+1,y) = \bar{i} - \Delta(x,y) + a(x,y) + n(x+1,y) \qquad (6\text{-}7)$$

where Δ*(x, y)* is the amplitude difference between *(x, y)* and *(x+1, y)*.

Given that the pixel amplitude and noise are independent with each other and the noise is also independently distributed, we have the following results:

$$\Sigma_{x,y} a(x,y) n(x,y) = 0 \qquad (6\text{-}8)$$

$$\Sigma_{x,y} n(x+1,y) n(x,y) = 0 \qquad (6\text{-}9)$$

Substitute the above formula into (6-4), we have the following formula:

$$F = \Sigma_{x,y} a(x,y)^2 - a(x,y)\Delta(x,y) \qquad (6\text{-}10)$$

In order to derive the formula (6-10), we assume that the following equations are established [105]:

$$\Sigma_{x,y} a(x,y)^2 \approx a(x+i,y)^2 \tag{6-11}$$

$$\Sigma_{x,y} n(x,y)^2 \approx n(x+i,y)^2 \tag{6-12}$$

$$\Sigma_{x,y} a(x,y) \approx a(x+i,y) \tag{6-13}$$

The above functions are correct when *i* is very small (i.e. *i* = 0, 1, 2) and *x*, *y* are very large (i.e. larger than 1000).

As demonstrated in Fig 28, the amplitude *a(x,y)* increases when the image is becoming sharper. Since the intensity difference $\Delta(x,y)$ increases slower than the amplitude *a(x,y)*, the overall value *F* will increase when the image is obtained at the focal plane.

6.2.6 Auto-focusing functions: Image variance

For each pixel of the image, this method computes the square of difference between pixel intensity and the average pixel value of the image, and then adds them together for the final value [105, 106, 108, 110]:

$$F = \Sigma_{x,y} (i(x,y) - \bar{i})^2 \tag{6-14}$$

Using the similar method as in *Section 8.2.5*, we can have the following equation [105]:

$$F = \Sigma_{x,y} (a(x,y)^2 + n(x,y)^2) \tag{6-15}$$

Given that the amplitude *a(x, y)* increases when the image is sharper, the variance function will also increase when the cell is placed closer to the focal plane.

6.3 Experimental methods

In microscopic imaging, the obtained images will become fuzzy with decreased contrast and edge sharpness when the imaged objects (e.g. metaphase chromosomes) are located outside of the focal plane. The image contrast can be estimated by several auto-focusing functions. Therefore, the in-focused position of the imaged objects can be determined by searching for the maximal image contrast value.

In this investigation, a number of five different auto-focusing functions were evaluated using the metaphase chromosome images acquired from the bone marrow and blood specimens. All the experiments were performed on a prototype microscopic image scanning system previously developed in our medical image laboratory [7]. The specimens were prepared based on the standard clinical procedure.

During the experiment, we selected and tested a number of the auto-focusing functions aiming to obtain the high contrast images with maximum sharpness of chromosome band patterns. In this study, we tested five typical methods selected from group i), ii) and iii), which are Brenner gradient, histogram range, threshold pixel counting, Vollath F5, and variance [104-106, 108, 109]. These methods have been used for a variety of biomedical specimens including fluorescent sample, blood smear, pop smear, and tuberculosis [110, 112-114]. These functions are described in *Section 6.2*.

In the above five functions, the focus value F is an estimation of image contrast. Since image contrast is smaller than 1, the computed focus values are normalized for each metaphase chromosome cell.

In order to evaluate the performance of the above five different auto-focusing functions, the off-line (static) evaluation method was applied in this investigation, which is widely accepted as a standard method [108-111, 113, 114]. The off-line evaluation assesses the auto-focusing functions using the previously captured chromosome images. In this study, chromosome images were obtained from blood and bone marrow specimens. For each specimen, a number of twenty metaphase chromosome cells were selected and used. For each cell, the focal position was first visually determined by the trained researchers. Then, a number of 25 images were captured for each cell by moving the scanning stage up and down in a range from +6μm to – 6μm, with a step of 0.5μm. To acquire clinically acceptable images, a 100× oil immersion objective lens was used in the experiments.

The performance of using each of these auto-focusing functions was then assessed based on the acquired images. The auto-focusing function was applied on each captured image and the focus value was calculated. The computed focus value was curved as a function of focusing positions. As illustrated Fig 30 (a), a typical auto-focusing curve has only one maximum, and the focusing position corresponding to the maximum value is determined as the in-focused position.

In order to assess the auto-focusing function, four evaluation criteria were applied in this study, including execution time, focusing accuracy, number of false maxima, and full width at the half maximum (FWHM). These measuring parameters are described as follows [110, 111, 114]:

1) Execution time: The time used to compute the auto-focusing value for each captured image.

2) Focusing accuracy: The difference between the visually determined and automatically determined focal positions. In this study, the visually determined position was calibrated at the central position. (0 μm)

3) Number of false maxima: False maximum is defined as the failed auto-focusing curve, as illustrated in Fig. 30 (b). In this case, the in-focused position cannot be determined from the curve.

4) FWHM: As shown in Fig. 30 (a), the auto-focusing value decreases vastly when the targeted cell is moved away from the in-focused plane. FWHM is the range where the auto-focusing function value reduces to 50% of the maximum.

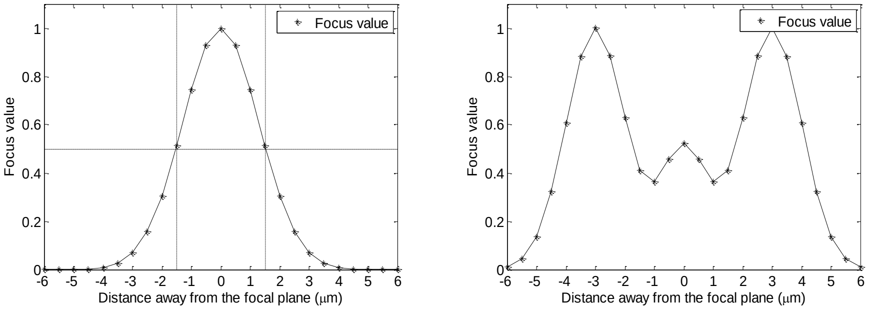

(a) (b)

Figure 30: Examples of an ideal focus curve (a) and a failed focus curve (b)

The calculated focus value is plotted as a function of focusing position. (a): An ideal focus curve is approximated by Gaussian function, which has only one maximum value corresponding to the focal plane (0μm). The focus value decreases when the cell is away. The range where the focus value is above 50% of the maximum is defined as full width at the half maximum (FWHM). (b): A failed auto-focusing curve. The focus curve has two maximal values, thus the focal position cannot be located.

The evaluation results were tabulated for comparison and analysis. Among the applied criteria, the number of false maxima was first considered, as this criterion directly demonstrates the efficacy of the auto-focusing functions. The execution time was then compared, which demonstrates the efficiency of the operation. The FWHM was analyzed next. The standard of the FWHM is related to the system depth of field (DOF), as the ideal focus curve can be approximated by the DOF contrast curve. The DOF is defined as the range where the measured contrast is larger than 80% of the maximum [9]. Under the experimental conditions (using 100× oil immersion objective lens), the measured DOF is 1.8μm. Thus, the ‘ideal’ FWHM will be approximately 3.0μm, as shown in Fig 34 (a). The focusing accuracy will not be used for comparison if the accuracy is within the system’s DOF. All auto-focusing algorithms were assessed using a personal computer equipped with an Intel i3 2.4G Hz dual core processor with 4G RAM using the MATLAB R2011 software application.

6.4 Experimental results

Fig. 31 demonstrates an example of the auto-focusing functions. Fig 31 (a) and (b) demonstrate two images that were separately acquired at the in-focus plane and 3μm away. Among these two images, Fig. 31 (b) is obviously blurred. Fig. 31 (c)-(g) illustrate the results of the five different auto-focusing functions. Among these functions, the Brenner function, threshold, Vollath F5 and variance methods can effectively locate the focal position, as the calculated value reaches the maximum around the focal plane (0 μm). The Brenner function deceases faster than the other three methods when the cell is moved away from the in-focused plane. Histogram range, however, fails to find the focal plane. The range value varies at different positions and no peak value can be found.

In the high throughput scanning microscope, the captured image is very large (3488×2048, 3488 pixels in x direction and 2048 pixels in y direction) and also contains interphase cells. As compared to the chromosome bands, the size of the interphase nuclei is larger, thus the spatial frequency is lower. According to the Fourier optics theory, the contrast of high spatial frequency regions decreases more significantly than the low frequency regions when the cell is moved away from the focal position [117]. Therefore, the high throughput scanning technique requires that the auto-focusing function can extract the useful high frequency components from the obtained image. Among all the five selected methods, Brenner function performs better than the others, as the difference operator can extract the high frequency information while discarding the others. The threshold pixel counting, Vollath F5, and variance methods can somehow extract the useful high frequency information. The pixel intensity variance of in-focused images is larger than the off focused images, which can be demonstrated by calculating the image variance (variance method), standard deviation (Vollath F5), or counting pixels with very low grayscale (threshold pixel counting). Histogram range method, however, cannot distinguish the high and low frequency components, as the range are mainly determined by the low frequency components.

Tables 3 and 4 summarize the statistical results of applying the five auto-focusing functions on the bone marrow and blood samples. The data demonstrates that Brenner function and threshold pixel count methods are superior to the others. Both these two methods can successfully locate the focal position with high reliability. The threshold pixel counting method has one false maximum in case of the bone marrow samples. For assessing efficiency, however, the threshold method is much more efficient than the Brenner function. Brenner function takes about 15 seconds to process a single image, while threshold method only needs about 0.2 second. The efficiency difference can be attributed by the fact that the Brenner gradient method has high computing complexity. The FWHM of the Brenner method is approximately 1.5μm, while the FWHM of the threshold method is larger than 12.5μm. As compared to the threshold method, the FWHM of the Brenner function (approximately 1.5μm) is closer to the ideal FWHM, which shows that the Brenner function is more sensitive to the change of focusing position. Thus, the Brenner function can search the focal plane more reliably than the threshold method. The accuracies of both these two methods are within the system's DOF.

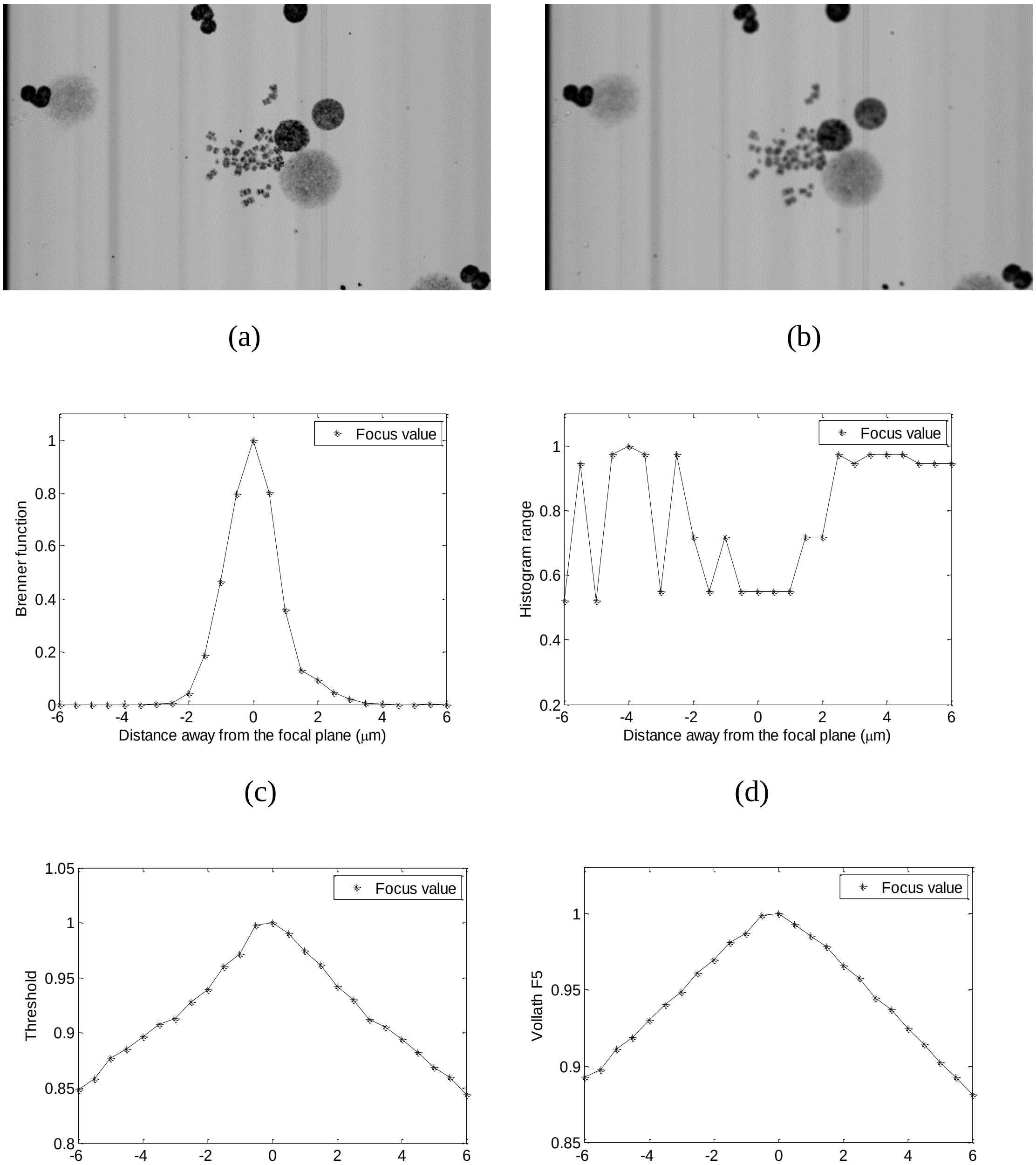

(a) (b)

(c) (d)

(e) (f)

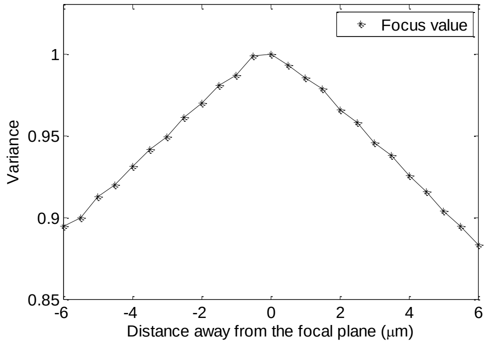

(g)

Figure 31: An example of auto-focusing functions performed on micorsopic images of a pathlogical cell acquried from bone marrow sample

(a): The cell was captured at in-focused position (b): The cell was captured 3μm away from the focal plane. (c): The focus value calculated by Brenner function. (d): The sharpness value calculated by Histogram range function. (e): The sharpness value calculated by Threshold pixel counting function. (f): The sharpness value calculated by Vollath F5 functions. (g): The sharpness value calculated by Variance function.

Table 3: Results of the evaluation of auto-focusing functions for bone marrow specimen

	Executing time (second)	Accuracy (μm)	Number of false maxima	Full width at half maximum (μm)
Brenner function	14.7125±0.6406(3)	0.2500±0.2565(1)	0(1)	1.6344±0.1630(1)
Histogram range	0.1411±0.0066(2)	1.3000±0.6708(5)	15(5)	≥12.5(2)
Threshold	0.1383±0.0033(1)	0.2895±0.2536(4)	1(2)	≥12.5(2)
Vollath F5	34.7059±3.0202(4)	0.2632±0.2565(2)	1(2)	≥12.5(2)
Variance	35.0119±0.8372(5)	0.2632±0.2565(2)	1(2)	≥12.5(2)

Note: Rank is illustrated in the parentheses.

Table 4: Results of the evaluation of auto-focusing functions for blood specimen

	Executing time (second)	Accuracy (μm)	Number of false maxima	Full width at half maximum (μm)
Brenner function	15.3441±0.4044(3)	0.2250±0.2552(2)	0(1)	1.3404±0.6354(1)
Histogram range	0.1435±0.0099(2)	1.1818±0.7833(5)	9(5)	≥12.5(2)
Threshold	0.1400±0.0064(1)	0.2000±0.2513(1)	0(1)	≥12.5(2)
Vollath F5	32.0297±0.6356(4)	0.2500±0.3035(3)	0(1)	≥12.5(2)
Variance	34.5461±0.2625(5)	0.2500±0.3035(3)	0(1)	≥12.5(2)

Note: Rank is illustrated in the parentheses.

Blood and bone marrow samples have different optimal auto-focusing functions. In clinical application, one or two auto-focusing false maxima is acceptable when scanning the blood specimens, as one slide usually contains 30-50 useful cells and clinicians only need 3-5 cells to make the diagnosis. Comparing to the Brenner function, the threshold pixel counting method has much higher efficiency while achieving a satisfactory accuracy and robustness. Therefore, the threshold pixel counting algorithm is suggested as the optimal selection.

For the bone marrow specimen, however, one slide only contains 5-6 useful analyzable metaphase cells. In order to collect enough (20) cells for diagnosis, clinicians need to screen 3-5 slides. Furthermore, even in in-focused state, the image quality of bone marrow cells is not as good as the blood cells, which may affect the auto-focusing operation. Thus, scanning of bone marrow slides requires very high reliability. On the other hand, executing time of the Brenner gradient is highly dependent on the computing environment. The executing time can be significantly reduced by utilizing a high efficiency programming language such as C/C++ under the environment of a high performance workstation. Therefore, Brenner function is the optimal solution for the bone marrow slide, as the Brenner function has high accuracy and robustness to the useless information, especially when using the images with decreased quality.

6.5 Discussion

Metaphase chromosome karyotyping of pathological specimens is a widely used technique for the diagnosis of genetic diseases. In the hospital, clinicians need to carefully examine the number or morphology of the chromosome bands, to determine whether the case is abnormal or not [1, 3, 6, 20, 21]. Therefore, during the image acquisition, we must ensure that the band sharpness is adequate for diagnosis, as the off-focused bands in the captured images might lead to false positive or false negative diagnostic results.

In order to keep the adequate band sharpness in microscopic images, auto-focusing techniques are necessary for the automatic or semi-automatic scanning microscopes, especially the high throughput scanning systems [12, 25]. The auto-focusing technique can be divided into auto-focusing function and searching algorithms. Since the performance of auto-focusing functions varies in different applications, the auto-focusing function must be carefully selected to achieve the satisfactory or optimal results. Although several studies have been reported on selecting the optimal auto-focusing function for some specimens, such as pap smear or tuberculosis, little effort has been done on how to select the “best” auto-focusing function for the metaphase chromosome images acquired from different pathological specimens (i.e. bone marrow or blood) in high resolution imaging environments [110, 112-114].

In this study, five auto-focusing functions were tested and compared on metaphase chromosome images obtained from bone marrow and blood specimens. Four different criteria were used for the evaluation. The results demonstrate that the Brenner gradient and threshold pixel counting are superior to the others. To achieve the optimal performance, Brenner gradient and threshold pixel counting methods are suggested for the bone marrow and blood sample scanning, respectively.

However, this preliminary study has several limitations. First, we only used blood and bone marrow samples. Some other specimens, such as amniotic fluid, product of conception (POC), which are also widely used in clinical practice, were not tested. Second, we only selected five different auto-focusing functions. Some recently developed functions were not considered [101, 118-120]. Third, the selected optimal auto-focusing methods have not been actually performed for realistic imaging scanning. Hence, a more comprehensive study is underway, which may help eventually optimize high throughput microscopic image scanning system in the future clinical practice.

Chapter 7: Objective evaluation of the microscopic image sharpness

7.1 Background

High throughput scanning microscopy is a widely used technique which has attracted extensive research efforts in the last several years [4, 6, 29, 121]. During the chromosome scanning, the efficiency can be improved by increasing the scanning speed [7]. However, for the high speed scanning, the sharpness of the obtained images may be deteriorated [88], which can be attributed to the short exposure, scanning blur, and the stage random vibrations. The deteriorated images cannot be clinically used, as they may lead to misdiagnosis. Therefore, we need to understand the relationship between the scanning speed and image sharpness deterioration.

In this study, the image sharpness at different scanning speeds was investigated objectively using a sharpness function. A standard resolution target and several clinically analyzable metaphase chromosomes were imaged at different scanning speeds, under the condition of 100× objective lens. Then the sharpness of the obtained images was objectively evaluated by a sharpness function.

7.2 Experimental methods

7.2.1 Objective sharpness evaluation of the microscopic images for standard resolution target

In scanning microscopy, the clinical slides are screened at high speed to improve the efficiency [7]. However, increasing the scanning speed may lead to sharpness deterioration of the captured images [88]. In this study, the deterioration was evaluated objectively using a sharpness function.

All the experiments were performed with a custom developed high throughput scanning microscopy prototype [7]. The prototype was built upon a commercialized microscope, which is equipped with a line scanning CCD detector based on the time delay integration (TDI) technique (Piranha HS-40-04k40, Dalsa Company, Ontario, Canada), and a high precision moving stage (99S000, Ludl Electronic Products, New York, U.S.A.). When the system is synchronized, the detector is able to acquire images continuously.

The experiment started with the image acquisition of the standard resolution target USAF1951 (USAF1951, Edmund Optics, New Jersey, U.S.A), which is performed under 100× objective lenses. The target contains a series of resolution patterns with different spatial frequencies up to 645 lp/mm. During the experiment, the target was first fixed on the stage, and the in-focused position is visually determined. Then the target was imaged when the stage is moving continuously with different speeds. Accordingly, the exposure time of the TDI detector must be synchronized with the speed, which can be determined by the following formula [77]:

$$T = \frac{p}{V \times M} \tag{7-1}$$

In the formula, T is the exposure time, V is the scanning speed, M is the system magnification (i.e. the magnification of the objective lens), and p is the pixel size of the detector, which is 0.007mm for our scanning prototype.

When the 100× objective lens was applied, the scanning speed can be ranged from 0.25 mm/s to 2.5mm/s, as the minimal and maximal exposure time of the detector are 1/36000 and 1/3500 second, respectively. Therefore, the investigated speed range was selected from 0.4mm/s to 2.4mm/s, with a step of 0.2mm/s.

After the images were acquired, the sharpness was assessed for each captured image. The evaluation was composed of two steps. Since there are a series of different patterns on each acquired image, we first used the system modulation transfer function (MTF) curve to select one resolution pattern for the assessment. The curve has been measured in our previous investigations [8, 9]. The spatial frequency for which the contrast drops to 50% of the maximum was determined for the following assessment [9]. Therefore, the 645 lp/mm pattern was used in the experiment.

Then, the image sharpness of the selected patterns was assessed. There are many different methods reported recently for the image sharpness evaluation [122, 123]. Among these methods, the gradient sharpness function has low computing complexity and high sensitivity to the change of the exposure. Thus the gradient sharpness function was used in this application, which is demonstrated as follows [79]:

$$S = \frac{1}{2mn}\{[i(x,y)-i(x-1,y)]^2 + [i(x,y)-i(x,y-1)]^2\} \tag{7-2}$$

Where S is the calculated sharpness value, *i(x, y)* is the intensity at pixel *(x, y)*, and m, n are the numbers of rows and columns respectively. The gradient sharpness function first computes the average intensity difference between pixel *(x, y)* and the neighbor pixels *(x-1, y)*, and *(x, y-1)*, respectively. Then, the algorithm adds the computed result of each pixel together and the final value is divided by the number of the pixels of the obtained pattern [79].

For each acquired image, the image sharpness value of the selected pattern was calculated. These sharpness values were finally curved as a function of scanning speed.

7.2.2 Objective sharpness evaluation of the microscopic images for metaphase chromosomes

Similarly, for the metaphase chromosomes, we randomly selected several clinically analyzable metaphase cells from the bone marrow sample. These chromosomes were imaged at the speed between 0.4 and 2.4 mm/s, under the condition of 100× (oil, N.A. = 1.25) objective lens. Among the 46 chromosomes for each acquired image, three of them were randomly selected for the objective sharpness assessment. At each speed, the calculated sharpness value of the selected chromosomes was averaged. The final results were plotted versus scanning speed.

7.3 Experimental results

7.3.1 Results of objective evaluation for standard resolution target

Fig. 32 (a) demonstrates the measured image sharpness values at different scanning speeds for the USAF1951 standard resolution target. The image sharpness is optimized at 0.6 mm/s, at which the target is properly exposed. An example is illustrated in Fig. 32 (c). In addition, the scanning blur and random vibration would not seriously affect the image sharpness when the speed is low. According to the formula (7-1), the exposure time decreases when increasing the scanning speed. Due to the under exposure, the sharpness decreases significantly at 0.8 mm/s, which can be attributed to the non-linearity of the sharpness function and the detector sensitivity. Besides the exposure time, the scanning blur and stage random vibration also affect the image sharpness when the speed is high. Therefore, the sharpness value decreases as the speed increases. When the speed is lower than 0.6 mm/s, the sharpness value decreases again, as the exposure is too long, and the resolution patterns are saturated with light.

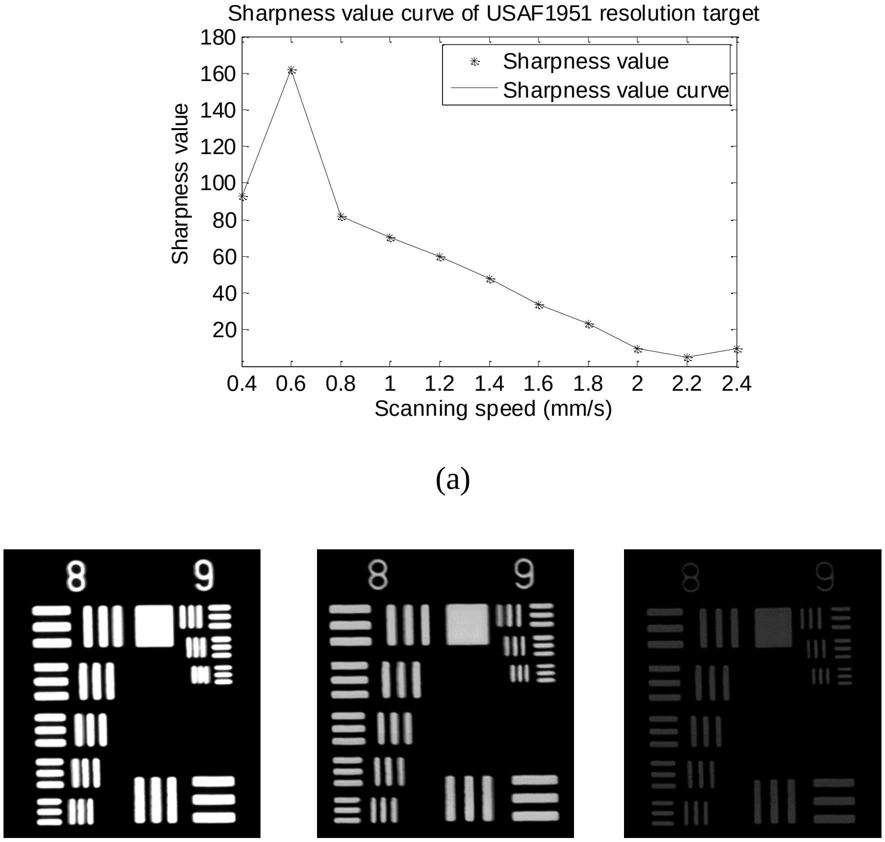

(a)

(b) (c) (d)

Figure 32: Sharpness curve and some partial images of a resolution target obtained at different scanning speeds

(a): The sharpness curve versus the scanning speed under the condition of 100× objective lens (oil, N.A. = 1.25). (b), (c) and (d): Three partial images acquired from the USAF1951 standard resolution target with a scanning speed of 0.3mm/s, 0.6mm/s and 1.6mm/s, respectively.

7.3.2 Results of objective evaluation for metaphase chromosomes

Fig. 33 (a) demonstrates the calculated sharpness value for the metaphase chromosomes. Similarly, the sharpness value reaches the maximum at 0.8 mm/s, and decreases when increasing or decreasing the speeds. Given that the sharpness is optimized at 0.6 mm/s when standard resolution target is imaged, this difference can be attributed to the fact that the attenuate coefficient of the bone marrow samples is smaller than the standard resolution target. The sharpness curve generally agrees with the subjective evaluation of the chromosome bands. When the chromosomes were captured at 0.6 or 0.8 mm/s, the band patterns are adequate for the diagnosis, as demonstrated in Fig 33 (c) and (d). The clinical meaning of the chromosomes decreases when the speed is lower than 0.6 mm/s or higher than 0.8 mm/s, as expected.

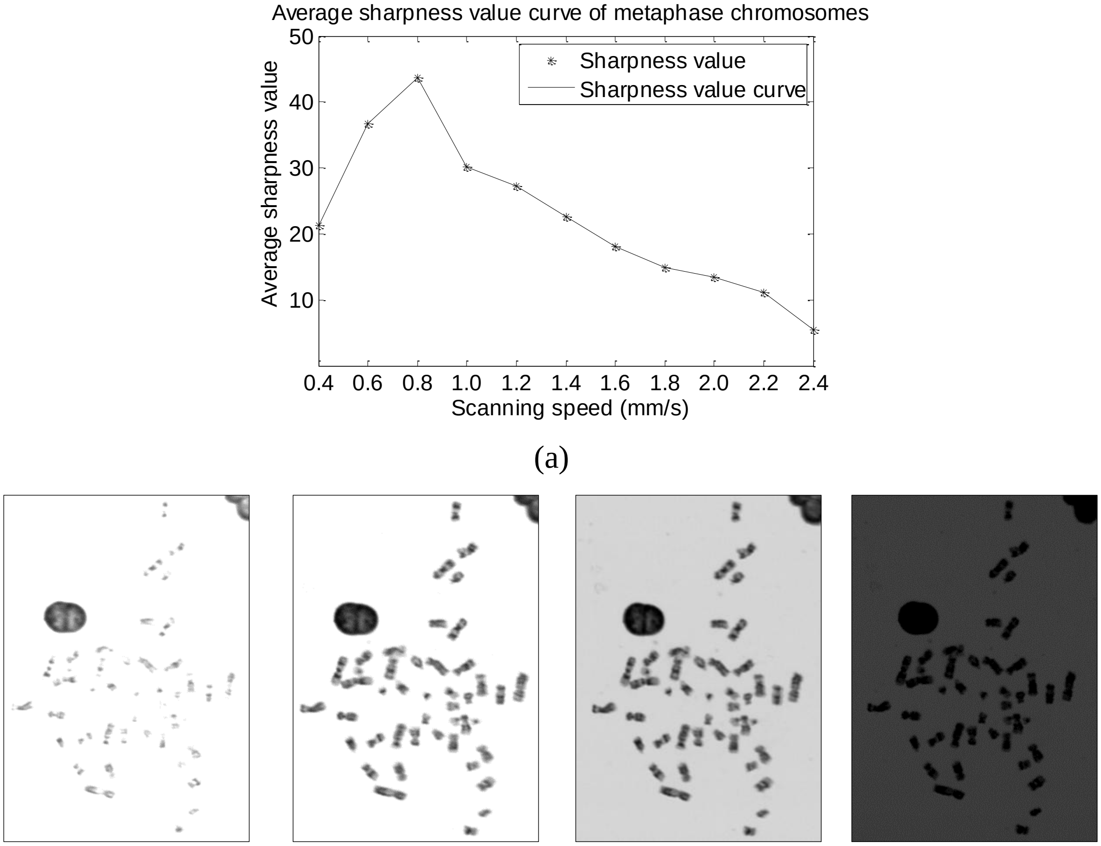

(a)

(b) (c) (d) (e)

Figure 33: Sharpness curve and some images of a metaphase chromosome obtained at different scanning speeds

(a): Sharpness curve versus the scanning speed, when using the 100× objective lens (oil, N.A. = 1.25). (b), (c), (d), and (e): Sample images of a pathologically analyzable chromosome obtained from bone marrow samples, with a scanning speed of 0.4 mm/s, 0.6 mm/s, 0.8 mm/s, and 1.6 mm/s, respectively.

7.4 Discussion

High throughput scanning microscopy is a widely applied technique for the diagnosis of the chromosome abnormalities. When applying this new technique, the sharpness of the chromosome band patterns is a critically important indicator of the image quality, as the acquired images with blurred bands may lead to misdiagnosis. In this study, the chromosome band sharpness was objectively investigated, using a gradient sharpness function. The standard resolution target and several pathological chromosomes were imaged at different scanning speeds, and the sharpness is objectively evaluated by the gradient sharpness function. The results reveal that the captured image sharpness is optimized at 0.6 and 0.8 mm/s, for the resolution target and metaphase chromosomes, respectively. The results general agree with the subjective assessment.

However, this study is preliminary. The clinical samples are limited to bone marrow, and we do not consider the interplay between the impact of speed and the impact of depth of field (DOF) [9]. A more comprehensive study is planned, which might be meaningful for improving the efficiency and quality of clinical cytogenetic scanning.

Chapter 8: An initial study of an automatic scanning method

8.1 Background

Developing automatic microscopic image scanning technologies and systems has been attracting wide research interest in clinical pathology and other areas for the diagnosis of a variety of cancers and other serious diseases [6, 121, 124]. For the high throughput scanning microscopic systems, one of the technical challenges is to minimize the impact of the random vibration and mechanical drifting of the scanning stage, to ensure that the specimen remains in focus during the scanning process, as the off focused images may seriously blur the targeted signals and increase the image noise that lead to reduce the diagnosis accuracy and reliability. In order to keep the system in focus, the current scanner repeatedly applies the auto-focusing operations on the entire imaging field. However, such a method is quite time-consuming and lowly efficient.

In our bioengineering laboratory, a sampling-focusing method was investigated, which differs from the traditional method in that the investigated method only applies the auto-focusing operations on a limited number of locations of the imaging field. For the rest of the imaging field, the focusing position is adjusted very quickly through linear interpolation. The purpose of this study is to investigate an optimal trade-off between image quality and scanning efficiency.

8.2 Experimental methods

The scanning method investigated in this study applies only a limited number of focusing adjustments during the scanning process. For an imaging field of a given size, applying a greater number of focusing operations increases the image quality, but this occurs at a cost of lower efficiency. Experimental studies were performed to determine the optimal trade-off between the quality and efficiency.

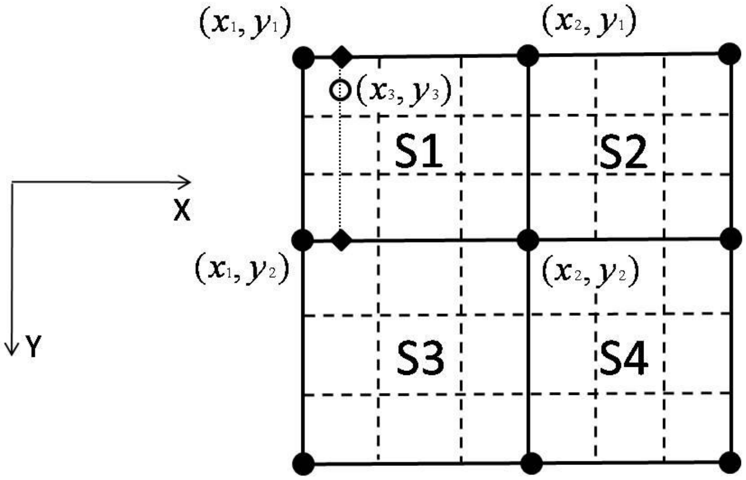

Figure 34: 3×3 scanning scheme

The schematic diagram was applied on the imaging field of pathological slides. The field size is 6.9mm×6.9mm. The bold dots indicate 9 locations where the z-position adjustments (focusing operations) are performed. S1, S2, S3, and S4 are four subfields. Each subfield is composed of 9 scanning regions. The interpolation is performed at the center of each scanning region, as shown by the open dot.

The experiments were performed on a high throughput microscopic image scanning system equipped with a Time Delay Integration (TDI) detector [7, 88]. Clinical slides of blood samples containing both metaphase and interphase cells were used in the experiments.

On the pathological slides, the imaging field size was selected as 6.9mm×6.9mm. Next, the auto-focusing locations were determined. A total of four different sampling schemes were utilized for comparison in this experimental investigation, which are 2×2, 3×2, 3×3, 4×4 auto-focusing locations.

For the 3×3 scanning scheme, a total of 9 auto-focusing locations are evenly distributed across the imaging field, as shown by the bold dots in Fig 34. The distance between two auto-focusing locations is 3.45mm in both the X and Y directions. The imaging field is composed of 4 subfields: S1, S2, S3 and S4. Each subfield has an area of 3.45mm×3.45mm, with four auto-focusing locations distributed at the corners. The method sequentially scans subfields S1, S2, S3, and S4.

Before scanning S1, the method first measures the in-focused z-position at the four corners of S1. At each corner, the motorized scanning stage moves up and down along the z-direction, to adjust the distance between the objective lens of the microscope and the blood sample. With the commonly used auto-focusing technique, the in-focused z-position is determined by comparing the sharpness of the images acquired at a series of z-positions. The z-position corresponding to the sharpest image is considered as the in-focused position. The image sharpness is assessed by applying a sharpness function on the acquired images. The sharpness function has been investigated by researchers for many years [109-111]. Specifically, in this study, a derivative-based sharpness function was applied, as this method has relatively low computational complexity [7, 88]. The function is calculated as follows:

$$SV(z) = \Sigma_{x,y}[i(x+1, y, z) - i(i-1, y, z)]^2 \qquad (8\text{-}1)$$

where $i(x+1,y)$ and $i(x-1,y)$ are the intensity of the pixel $(x+1, y)$ and $(x-1, y)$ of the image which is captured at focusing position z. SV is the sharpness value. The image with the largest sharpness value SV is selected as the sharpest image. The auto-focusing operation is applied on the four corners of S1 to determine the in-focused z-position resulting in the sharpest image.

Then, the method scans the subfield S1, which is divided into 9 scanning regions, as illustrated by the dashed line in Fig 34. Each region has an area of 1.15 mm×1.15mm. The region is scanned continuously by the TDI camera with a fixed z-position, which is calculated by interpolating the measured z-positions at the four corners of the subfield. In the experiment, linear interpolation was applied, as this algorithm is the most efficient method among all the interpolation algorithms [7, 88]. The interpolation is performed at the center of each scanning region, using the following formula:

$$Z(x_3, y_3) = [1-\bar{x}_3 \quad \bar{x}_3]\begin{bmatrix} Z(x_1, y_1) & Z(x_1, y_2) \\ Z(x_2, y_1) & Z(x_2, y_2) \end{bmatrix}\begin{bmatrix} 1-\bar{y}_3 \\ \bar{y}_3 \end{bmatrix} \tag{8-2}$$

In the formula, we have $\bar{x}_3 = \frac{x_3 - x_1}{x_2 - x_1}$ and $\bar{y}_3 = \frac{y_3 - y_1}{y_3 + y_1}$. $Z(x_1,y_1)$, $Z(x_1,y_2)$, $Z(x_2,y_1)$, and $Z(x_2,y_2)$ the in-focused z-positions measured at four locations (x_1, y_1), (x_1, y_2), (x_2, y_1), and (x_2, y_2), respectively.

When the automated-processing of one region is completed, the method moves to the next region until the entire subfield is finished. When S1 is finished, the method scans subfields S2, S3, and S4 using the same approach.

For the 2×2 scheme, the 4 auto-focusing locations are at the four corners of the entire imaging field, and only one subfield is utilized. The 3×2 scheme has 2 scanning subfields, with a size of 3.45mm×6.9mm. The 4×4 scheme has 9 scanning subfields, with a size of 2.3mm×2.3mm. After all the scanning schemes are finished, the clinically meaningful cells are selected from the scanned results and tabulated for comparison.

8.3 Experimental results

Table 5 presents the scanning results from using each of the four different sampling schemes. 25 clinically useful cells were selected when the 2×2 sampling scheme is applied, with a scanning time of 15 minutes. Similarly, when the 3×2, 3×3, and 4×4 sampling schemes were applied, 29, 40 and 41 analyzable cells were identified. However, the scanning time also increases to 21, 29 and 44 minutes, respectively.

Table 5: Comparison between the automatic screening using different sampling schemes

The sampling scheme	Identified useful cells	Scanning time
2×2	25	15 min
3×2	29	21 min
3×3	40	29 min
4×4	41	44 min

The results show that different scanning schemes obtain different numbers of useful cell images, which can be attributed to the z-position interpolation. During the scanning, the interpolated z-position might be different from the in-focused z-position, thus some analyzable cells may be captured as off focused images, which cannot be used for diagnosis. The error decreases when more locations are sampled, as the interpolation is more accurate when the distance between two auto-focusing locations is small. Therefore, more useful images are captured when the number of sampled locations increases. Fig 35 illustrates a clinically analyzable cell captured by the 3×2 and 3×3 sampling schemes in (a) and (b), respectively. The chromosome bands in Fig 35 (a) are unrecognizable. In Fig 35 (b), however, the image sharpness has been substantially improved and the chromosome bands have adequate sharpness for clinical interpretation.

The results demonstrate the trade-off between the scanning efficiency and the number of acquired analyzable cells. As discussed previously, more clinically useful cells can be selected when a larger number of auto-focusing locations are sampled. However, the scanning efficiency will decrease when the number of auto-focusing operations increases. In this specific experiment, the 2×2 sampling scheme identifies 25 clinically meaningful cells, which is adequate in most clinical situations where visually selecting 20 analyzable cells are required to make a diagnostic decision. However, in order to improve diagnostic accuracy in heterogeneous cases in which more numbers of analyzable cells are needed, the 3×2 and 3×3 sampling schemes also provide an option, as these two schemes acquired 4 or 15 more analyzable cells for high accuracy diagnosis, respectively. Obviously, the 4×4 sampling scheme is not recommended, as it takes too much time (44 minutes) by acquiring one additional useful cell, as compared to the use of the 3×3 sampling scheme.

(a) (b)

Figure 35: Microscopic images of a clinically analyzable cell contained in a blood sample, captured by (a) 3×2, (b) 3×3 sampling scheme, respectively

8.4 Discussion

Developing high throughput microscopic image scanning systems has potential to improve disease diagnostic accuracy and efficiency in variety of clinical applications. During the automatic scanning, keeping the specimen in focus is critically important, as the random vibration and mechanical drifting of the stage may result in off focused images, which could make the actually analyzable cells not diagnosable or introduce diagnostic errors. The random vibration and mechanical drifting can be vastly reduced by repeatedly performing the auto-focusing operation on the specimen. However, this method is quite inefficient and unnecessary. The new selective auto-focusing methods evaluated and compared in this preliminary study may offer a practical solution that enables to balance the trade-offs between image quality and scanning efficiency. To assess the robustness of the new scanning method, more comprehensive research has been planned to study these and other design trade-offs for developing the optimal scanning scheme of the high throughput microscopic systems.

Chapter 9: Feature selection for the automated detection of metaphase chromosomes: Performance comparison using a receiver operating characteristic (ROC) method

9.1 Background

Chromosome imaging and karyotyping is an important and widely used clinical method for the diagnosis of genetic related diseases and cancers [1-3]. For this technique, identifying a sufficiently large number of pathologically analyzable metaphase chromosomes is critically important for the final accuracy of cancer diagnosis and residual cancer cell detection. Traditionally, these analyzable metaphase chromosomes are screened and detected manually by the experienced clinicians, which is labor intensive and time consuming. In addition, manual identification also creates substantial inter-observer variation due to the bias of cell selection (i.e., the tendency towards selecting cells with good morphology). Therefore, the automatic scanning techniques are proposed and developed in the last 20 years, in an attempt to reduce the clinicians' workload and improve the diagnostic accuracy and consistency [4].

Recently, a new high throughput scanning method was reported in our laboratory[7]. Comparing to the conventional microscopic image scanners, our new method combines the slide screening and image acquisition, which is able to directly provide the images containing high resolution chromosomes for the following diagnosis purpose [7, 12, 88]. In order to apply the high throughput scanning to the future practice, a computer aided detection (CAD) scheme is needed to be integrated into the image scanning procedure, for selecting the analyzable metaphase chromosomes [7]. The CAD scheme extracts and computes a set of image features from the segmented region of interest (ROI) on the acquired image, in an effort to further determine whether the image contains analyzable chromosomes. Thus selecting optimal and robust features is critically important in the CAD scheme, as the image features will directly determine the final accuracy of the entire scheme. In the last several years, investigating new features has received extensive research interest and a series of different methods have been reported [27-29, 78, 125]. However, the effectiveness of feature selection is often application oriented. The previously published chromosome features cannot be directly compared for our CAD scheme, as these methods are applied under different scanning conditions and evaluated using different standards. Therefore, we need to investigate how to effectively evaluate these features under the high throughput scanning condition.

For this purpose, we performed a new study in which a certain amount of bone marrow chromosomes were scanned and imaged under the high throughput scanning prototype. Different image features were computed by our CAD scheme to detect and classify the analyzable cells among the scanned images. The performance of the features was assessed and compared using a receiver operating characteristic (ROC) data analysis method. The detailed experimental methods and results are reported as follows.

9.2 Receiver operating characteristic (ROC) curve: Basic concepts

9.2.1 ROC curve: Four categories in the diagnosis

During the diagnosis, the patients will be identified as normal (negative) or abnormal (positive) to a specific disease (i.e. Hypertension, cancer, etc). Given that all the patients can be divided into normal and abnormal classes, a number of 4 different categories will be generated, as demonstrated in Fig 36 [126-128]:

True positive category (TP): The actually abnormal patient is diagnosed as abnormal.

False positive category (FP): The patient is diagnosed as abnormal. However, he (she) is actually normal.

True Negative category (TN): The actually normal patient is diagnosed as normal.

False Negative category (FN): The patient is diagnosed as normal. However, he (she) is actually abnormal.

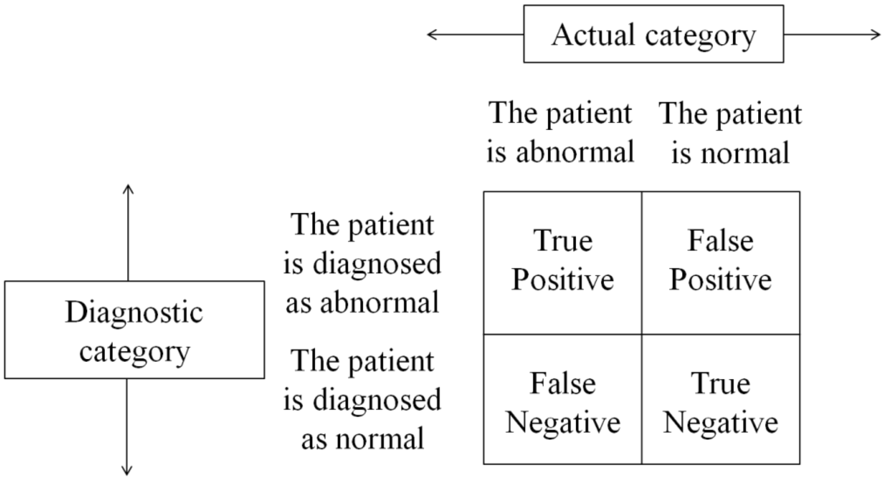

Figure 36: The confusion matrix of the diagnosis [127]

Accordingly, the number N_{TP}, N_{FP}, N_{TN}, N_{FN} are defined as the number of patients in true positive (TP), false positive (FP), true negative (TN), false negative (FN) categories, respectively.

Based on the above four numbers (N_{TP}, N_{FP}, N_{TN}, N_{FN}), the following concepts are defined:

True positive fraction (TPF): TPF is the ratio between the number of TP patients and all the actually positive (abnormal) patients: TPF = $N_{TP} / (N_{TP} + N_{FN})$.

False positive fraction (FPF): FPF is the ratio between the number of FP patients and all the actually negative (normal) patients: FPF = $N_{FP} / (N_{FP} + N_{TN})$.

True negative fraction (TNF): TNF is the ratio between the number of TN patients and all the actually negative (normal) patients: TNF = $N_{TN} / (N_{TN} + N_{FP})$.

False negative fraction (FNF): FNF is the ratio between the number of FN patients and all the actually positive (abnormal) patients: FNF = $N_{FN} / (N_{TP} + N_{FN})$.

Obviously, the following formulas are established:

$$TPF + FNF = 1 \tag{9-1}$$

$$TNF + FPF = 1 \tag{9-2}$$

Specifically, the TPF and TNF are also defined as sensitivity and specificity, respectively.

In addition, the diagnosis accuracy (A) is defined as the ratio between the number of all the correctly diagnosed patients and the total patients:

$$A = (N_{TP} + N_{TN}) / (N_{TP} + N_{FP} + N_{TN} + N_{FN}) \tag{9-3}$$

9.2.2 ROC curve: Definition

ROC curve was first applied in random signal detection, which is defined as the curve of sensitivities at different specificities [126, 129, 130]. At present, the ROC curve is wildly used in the assessment of medical diagnosis.

During the diagnosis, especially in the radiological diagnosis, the patients are classified into several categories. For example, in the breast cancer diagnosis, all the mammograms are divided into five different categories [131, 132]: Definitely benign, benign, probably benign, probably malignant, and definitely malignant. Suppose there are 100 patients, among which 50 are actually breast cancer patients and the others are normal [131]. After the mammogram screening, the radiologist's diagnosis results are illustrated in the following table:

Table 6: The radiologists' diagnostic results of 100 patients

	Definitely malignant	Probably malignant	Probably benign	Benign	Definitely benign	Total
Abnormal	30	7	2	6	5	50
Normal	6	5	3	5	31	50
Total	32	12	9	11	36	100

Since the patients are classified into 5 different categories, six decision rules can be designed:

Rule1: All the patients are diagnosed as normal.

Rule2: The patients with definite malignant results are diagnosed as abnormal, and others are normal.

Rule3: The patients with definitely malignant and probably malignant results are diagnosed as abnormal, and others are normal.

Rule4: The patients with definitely malignant, probably malignant, and probably benign results are diagnosed as abnormal, and others are normal.

Rule5: The patients with definitely malignant, probably malignant, probably benign, and benign results are diagnosed as normal, and others are abnormal.

Rule6: All the patients are diagnosed as abnormal.

Accordingly, based on these rules, the different sensitivities and specificities can be estimated, as illustrated in the Table 7. Using these data, the empirical ROC curve is plotted, which is demonstrated in Fig 37.

Note that the malignant patients are considered positive in the diagnosis.

Table 7: The calculated sensitivity and specificity of the radiologists' diagnostic results

Diagnosis rules	Sensitivity (TPF)	Specificity (TNF)	FPF
Rule1	0	1	0
Rule2	30/50=0.6	(5+3+5+31)/50=0.88	1-0.88=0.12
Rule3	(30+7)/50=0.74	(3+5+31)/50=0.78	1-0.78=0.22
Rule4	(30+7+2)/50=0.78	(5+31)/50=0.72	1-0.72=0.28
Rule5	(30+7+2+6)/50=0.9	31/50=0.62	1-0.62=0.38
Rule6	1	0	1

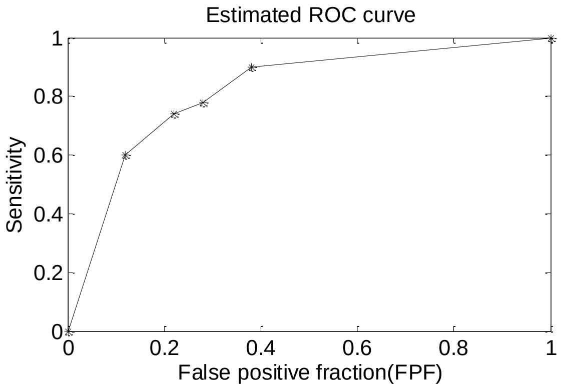

Figure 37: The empirical ROC curve of the above example

9.2.3 ROC curve: Models and estimation

In the realistic application, the distribution of the true and false positive cases can be approximated as normal distributions [133-136]. In order to determine the TPF at different FPF, a number of K different discrimination thresholds are selected, as illustrated in Fig 38 (a). At each threshold x_t, the TPF and FPF is the shaded area under the curve [127, 129]:

$$TPF = P(x_t \le x \mid positive) = \frac{1}{\sqrt{2\pi}\sigma_p}\int_{x_t}^{\infty} e^{-\frac{(x-\mu_p)^2}{2\sigma_p^2}}\,dx = \Phi[(\mu_p - x_m)/\sigma_p] \qquad (9\text{-}4)$$

$$FPF = P(x_t \le x \mid negative) = \frac{1}{\sqrt{2\pi}\sigma_n}\int_{x_t}^{\infty} e^{-\frac{(x-\mu_n)^2}{2\sigma_n^2}}\,dx = \Phi[(\mu_n - x_m)/\sigma_p] \qquad (9\text{-}5)$$

In these formulas, μ_p and σ_p are the mean and standard deviation of the normal distribution for the positive cases, while μ_n and σ_n are the mean and standard deviation of the normal distribution for the negative cases.

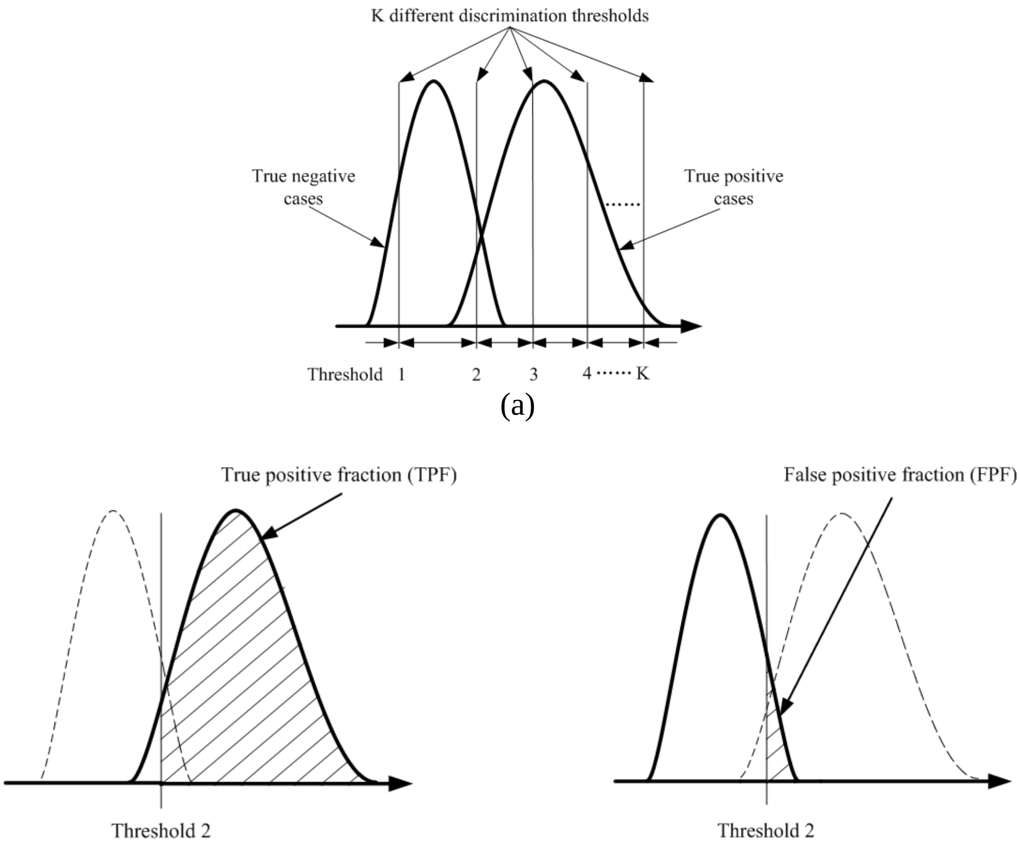

(a)

(b)

(c)

Figure 38: The demonstration of the binomial modal for the ROC curve [127]

(a): A number of 5 discrimination thresholds are used for the ROC estimation. For each threshold, the TPF (b) and FPF (c) can be estimated as the shaded area under the curve.

Using z as the standard normal random variable, we have:

$$z_{TPF} = (\mu_p - x_m) / \sigma_p \tag{9-6}$$

$$z_{FPF} = (\mu_n - x_m) / \sigma_n \tag{9-7}$$

Therefore, the following formula is derived:

$$z_{TPF} = \frac{(\mu_p - \mu_n)}{\sigma_p} + \frac{\sigma_n}{\sigma_p} \times z_{FPF} \tag{9-8}$$

Given that TPF = $\Phi(z_{TPF})$ and FPF = $\Phi(z_{FPF})$, we have

$$TPF = \Phi(a + b \times \Phi^{-1}(FPF)) \tag{9-9}$$

where a = $(\mu_p - \mu_n) / \sigma_p$, b = σ_n / σ_p.

Using $t_i = (x_i - \mu_n) / \sigma_n$ as the normalized discrimination threshold, the FPF is:

$$FPF = \Phi(\frac{\mu_n - x_i}{\sigma_n}) = 1 - \Phi(t_i) \tag{9-10}$$

Therefore, we have:

$$TPF = \Phi(a + b \times \Phi^{-1}(FPF)) = \Phi(a + b \times (-t_i)) = 1 - \Phi(b \times t_i - a) \tag{9-11}$$

The coordinates (x, y) at the ROC curve can be written as:

$$(FPF, TPF) = (1 - \Phi(t_i), 1 - \Phi(b \times t_i - a)) \tag{9-12}$$

where t_i ranges from $-\infty$ to $+\infty$.

Therefore, the entire curve is completely determined when the parameter a and b are estimated.

In order to estimate a and b, the maximum likelihood (ML) method is applied.

As mentioned before, if a number of K different discrimination rules x_1, x_2 ,x_3,…x_K is made, an number of K+1 categories are accomplished.

Thus the probability P ($x \geq x_i \mid p$) is equal to the estimated sensitivity (TPF) when using discriminating rule *i*. Similarly, the probability P ($x \geq x_i \mid n$) is equal to the estimated FPF (1 – specificity) when using discriminating rule *i*.

Therefore, the probability of one actually positive (abnormal) case locating in category *r* ($1 \leq r \leq N+1$) is:

$$P(r \mid p) = P(x_{r+1} \mid p) - P(x_r \mid p) \tag{9-13}$$

The probability of one actually negative (normal) case locating in category r (1 $\leq r \leq N+1$) is:

$$P(r \mid n) = P(x_{r+1} \mid n) - P(x_r \mid n) \tag{9-14}$$

Suppose the dataset has M actually positive (abnormal) cases and N actually negative (normal) cases. Among the M abnormal cases, m_1, m_2,… m_{K+1} responses are located in the K+1 categories, respectively. Similarly, among the N normal cases, n_1, n_2, … n_{K+1} responses are located in the K+1 categories. Then the likelihood of establish such as dataset is [127, 129]:

$$\begin{aligned} P(M, N \mid a, b, x) &= P(1 \mid p)^{m_1} \times P(2 \mid p)^{m_2} \times \ldots \times P(K+1 \mid p)^{m_{K+1}} \\ &\times P(1 \mid n)^{n_1} \times P(2 \mid n)^{n_2} \times \ldots \times P(K+1 \mid n)^{n_{K+1}} \end{aligned} \tag{9-15}$$

where x is the K different discrimination rules.

Then

$$\ln P(M, N \mid a, b, x) = \sum_{i=1}^{K+1} P(i \mid p)^{m_i} + \sum_{i=1}^{K+1} P(i \mid n)^{n_i} \tag{9-16}$$

Using θ to represent the K+2 parameters (a,b, x_1, x_2, …, x_K), then the maximum probability P is achieved when the following condition is satisfied:

$$\frac{\partial \ln P(M, N \mid a, b, x)}{\partial \theta} = 0 \tag{9-17}$$

The parameters can be solved by expanding the above equation. Currently, some standard programs are published and widely used to estimate the ROC curve, such as ROCKIT program, which is developed by Metz [129, 130, 137-139].

In the example discussed in the last section, the sensitivities are 0, 0.6, 0.74, 0.78, 0.9, and 1, while the corresponding FPF are 0, 0.12, 0.22, 0.28, and 0.38, respectively. Using the ROCKIT program, the estimated ROC curve is demonstrated in Fig 39.

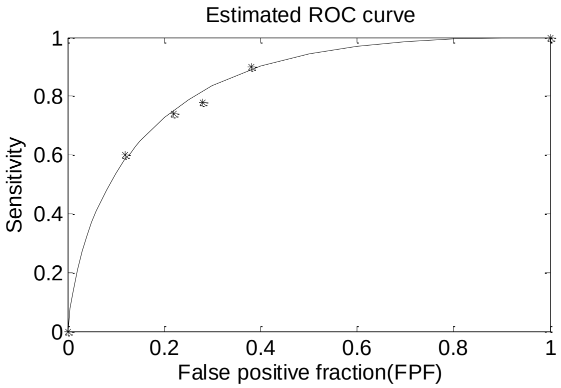

Figure 39: The estimated ROC curve of the example in *Section 9.2.2*

9.2.4 Performance evaluation using ROC curve

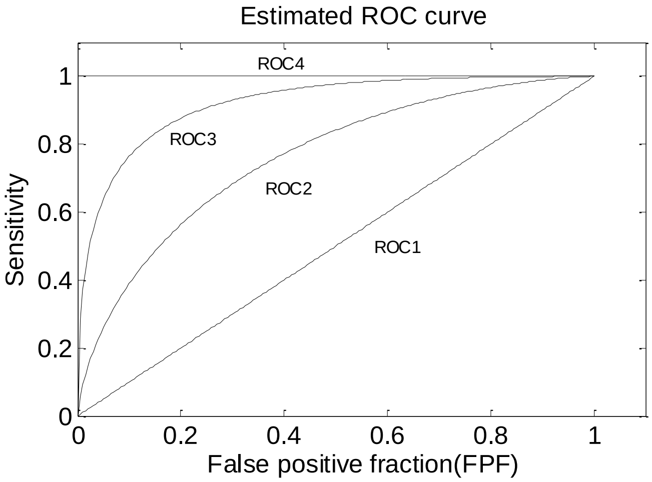

Figure 40: Four different ROC curves

In order to assess the performance of the diagnostic methods, the most important parameter of the ROC is area under curve (AUC). Given one randomly selected positive and one randomly selected negative cases, the AUC is the average probability for which the tested method will give the positive case a higher score than the negative case [140]. Fig 40 illustrates the ROC of four different diagnostic methods (Classifiers). Method 1 has an AUC of 0.5, for which the TPF (Sensitivity) is always equal to the FPF.

Factually, Method 1 is equivalent to the random classification, which has the worst performance among all the four illustrated methods. Method 3 is better than method 2, as method 2 has larger AUC that method 3, and method 3 also has a higher sensitivity than ROC2 at any FPFs. Method 4 is the perfect method with an AUC of 1, which has sensitivity of 1 at any FPFs.

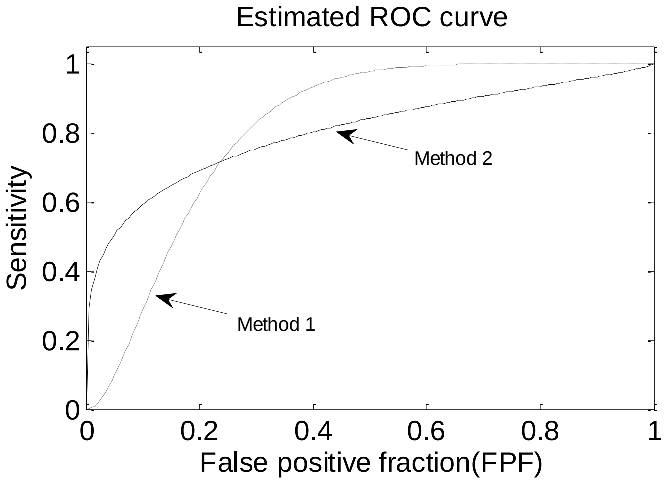

Figure 41: A comparison between two different ROC curves with similar AUC

In many situations, we need to compare the performance of the method at a specified FPF. Fig 41 is an example. The overall performance of method 1 and 2 are very close, as they have similar AUC (Method 1: 0.8145, Method 2: 0.8044). However, the performance of method 1 is better than 2 at high FPF (Low specificity), while the method 2 is better than 1 at low FPF (high specificity). These two different methods might be suitable for different patients. For the average patients, the number of the actually normal (Negative) cases is much more than the abnormal (Positive) cases, the clinician will use the decision rule with high specificity, to reduce the number of the false positive patients. Therefore, Method 2 is more suitable for the average patients, as method 2 has higher sensitivity when the FPF is low (FPF = 1 – specificity). However, if the patients have family history of breast cancer, the clinician will use the decision rule with very high sensitivity to decrease the risk of false negative diagnosis. This high sensitivity will occur with low specificity (or high FPF). Therefore, for these highly suspicious patients, method 1 is more suitable as its sensitivity is higher than method 2 when the FPF is very high.

9.3 Experimental materials and methods

During the specimen slide scanning, only a small amount of the scanned images are qualified for the clinical examination, as most of the scanned image regions contain un-analyzable cells due to the sample processing in genetic laboratory. Therefore, a CAD scheme is applied to detect and identify the image regions of interest (ROIs) depicting the analyzable chromosomes. To develop an effective and robust CAD scheme, feature extraction is a critically important step in the CAD development and optimization [4, 27-29].

In this investigation, different features were assessed under the high throughput scanning condition. The entire assessment includes the following three steps. First, a number of 200 cells were randomly selected from bone marrow specimens. All the selected cells were imaged under our recently developed scanning microscopy prototype [7]. Each cell was captured under a 100× objective lens, by a time delay integration (TDI) camera with a pixel size of 7 μm.

Second, the CAD scheme computed a number of images features for the region of interest on the obtained image. The feature pool includes a number of nine different features, which are widely used for the chromosome classifications [27-29]. They are detailed as follows:

1) Number of the labeled regions [29]: Aftering applying the region growth and labeing algorithm, the CAD detects and counts the number of the isolated "chromosomes".

2) Average region pixel intensity [79]: The CAD computes the average pixel intensity value for all the labeled "chromosomes" on the image.

3) Standard deviation (STD) of the region pixel intensity [79]: The CAD first computes the average pixel intensity for each labeled region, and then calculates the standard deviation of the region pixel intensity for all the labeled "chromosomes".

4) Average region area [79]: The CAD computes the area of each labeled region ("chromosome") by counting the number of the pixels contained in the region. The average region area for the entire image was computed by averaging the region area of all the labeled regions.

5) STD of the region area [79]: The CAD computes the standard deviation of the region area for all the labeled regions contained on the entire image.

6) Average region circularity [29, 80]: In order to calculate this feature, the circularity of each labeled region was first computed. For each region, an equivalent circle was created, and this circle has the same area as the labeled region. The CAD then computes the overlapped area (A_o) between the equivalent circle and the entire region. The region circularity is then defined as the ratio between the overlapped area (A_o) and entire regions area (A): A_o / A. After that, the circularities of all the regions were averaged for the entire image.

7) STD of the region circularity [29, 80]: The CAD computed the standard deviation of the circularities of all the labeled regions within the entire image.

8) The average region distance [29]: The CAD first computes the global gravity center (x_g , y_g) of all the labeled regions. The radial distance is then defined as the distance between the gravity center (x, y) of each labeled region and global gravity center (x_g , y_g). The radial distances of all the regions were averaged as the average region distance.

9) STD of the region distance [29]: The CAD computes the standard deviation of the region distances for all the labeled regions on the image.

Third, the performance of the CAD scheme was assessed using a receiver operating characteristic (ROC) method [126, 129, 130]. For each feature, a ROC curve was computed by estimating the true positive fraction (TPF) at different false positive fractions (FPF) [129]. In the realistic application, the distribution of the true and false positive cases can be approximated as normal distributions [129, 130]. In order to estimate the TPF at different FPF, the data were categorized by several discrimination thresholds. At each threshold, the TPF and FPF were estimated. The ROC curves were estimated by maximum likelihood method, using the ROCKIT program, as discussed in *Section 9.2* [129].

In this investigation, the area under the curve (AUC) was first computed [129]. The features with an AUC under or close to 0.5 were discarded, as their performances are not better than the random decision. Then, each pair of the remained features was compared and the difference significance among these feature classifying performances was determined by the partially paired model [141]. Finally, the correlation of the ROC curve was also calculated to analyze the statistical independence of the features [139].

9.4 Experimental results

Fig 42 shows three images acquired by the high throughput scanner. Fig 42 (a) contains a clinically analyzable region of interest (ROI), while Fig 42 (b) and (c) do not contain analyzable chromosomes for diagnostic purpose. Fig 42 (b) only contains interphase cells. Fig 42 (c) has more than one metaphase cells, and they are overlapped with each other. It can be seen that all the metaphase chromosomes are located in a certain area of the image. Comparing to the interphase cells, the metaphase chromosome is bright and has small size. In addition, the shape of the metaphase chromosome is totally different from the approximately circular interphase cells. The number of the labeled regions in Fig 42 (a) is much larger than Fig 42 (b), as a normal human cell contains 46 chromosomes and one meaningless image would not contain so many interphase cells. As demonstrated in Fig 42 (c), some un-analyzable images have more than one metaphase cells, so the number of the labeled regions is much larger than Fig 42 (a).

Fig 43 shows two scatter diagrams of the dataset demonstrating the relationship of the feature distribution between analyzable and un-analyzable ROIs. Fig 43 (a) is a scatter diagram between average region area and number of the labeled regions. Since most of the chromosomes can be labeled as individual region, most of the analyzable cells have more labeled regions. Moreover, the metaphase chromosomes are much smaller than the un-analyzable interphase cells. Thus most of the clinically analyzable cells are located in the up left corner of the diagram. Some un-analyzable cells are also located in the up left corner, because some un-analyzable cells contain many meaningless metaphase chromosomes, as illustrated in Fig 42(c). Fig 43 (b) is the feature distribution between number of the labeled regions and the average region circularity. A lot of features are overlapped in the horizontal direction, as some short analyzable chromosomes also have a large circularity and the captured analyzable images also contain interphase cells with large circularity.

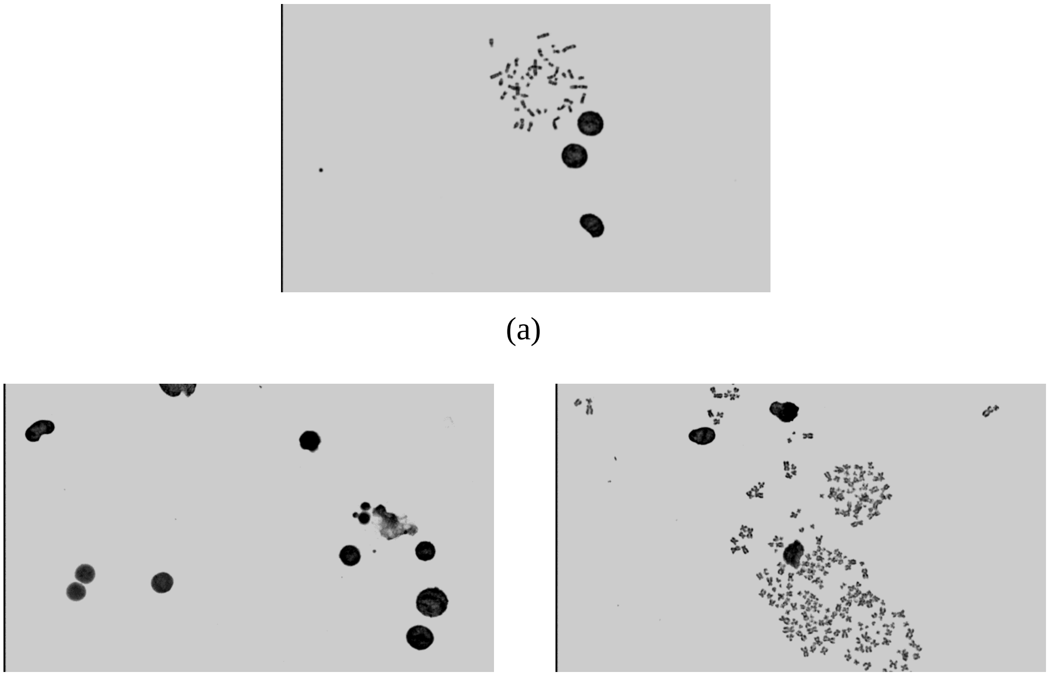

(a)

(b) (c)

Figure 42: Three examples of the microscopic images capitured by the high throughput scanner

The cells were acquried under a 100× objective lens, and imaged by a TDI detector with a pixel size of 7μm. (a): The image contains a clinically analyzable region of interest (ROI). (b) and (c): The image are meaningless to the diagnosis.

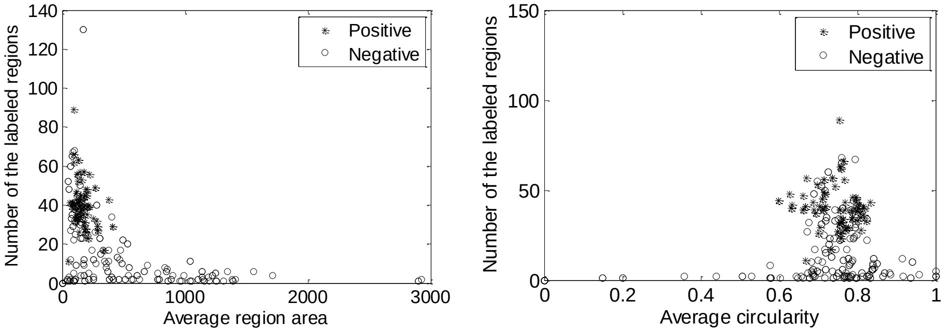

(a) (b)

Figure 43: The feature scatter diagram of the dataset

(a) and (b): The dataset contains 67 clinically meaningful and 133 clinical meaningless chromosomes. The vertical axis shows the number of the labeled regions, while the horizontal axis represents average region area and average region circularity, respectively.

Figure 44 and 45 demonstrate and compare a set of ROC curves computed from different features. Among all these features, the number of the labeled regions, average region area, average region pixel value, the STD of the region circularity, and STD of the region distance demonstrate high discriminatory ability, as the area under curve (AUC) of the other four features are under or very close to 0.5. Among these features, the AUC of the number of the labeled regions are 0.896±0.023, which is significantly better than the AUC of the average region area (0.666±0.037), average region pixel intesity (0.592±0.039), STD of the circulairity (0.581±0.039), and STD of the region distance (0.625±0.038). Although the AUC of the other four features range from 0.666 to 0.581, the differences between these features are not statistically significant ($p \geq 0.05$), as illustrated in Table 8.

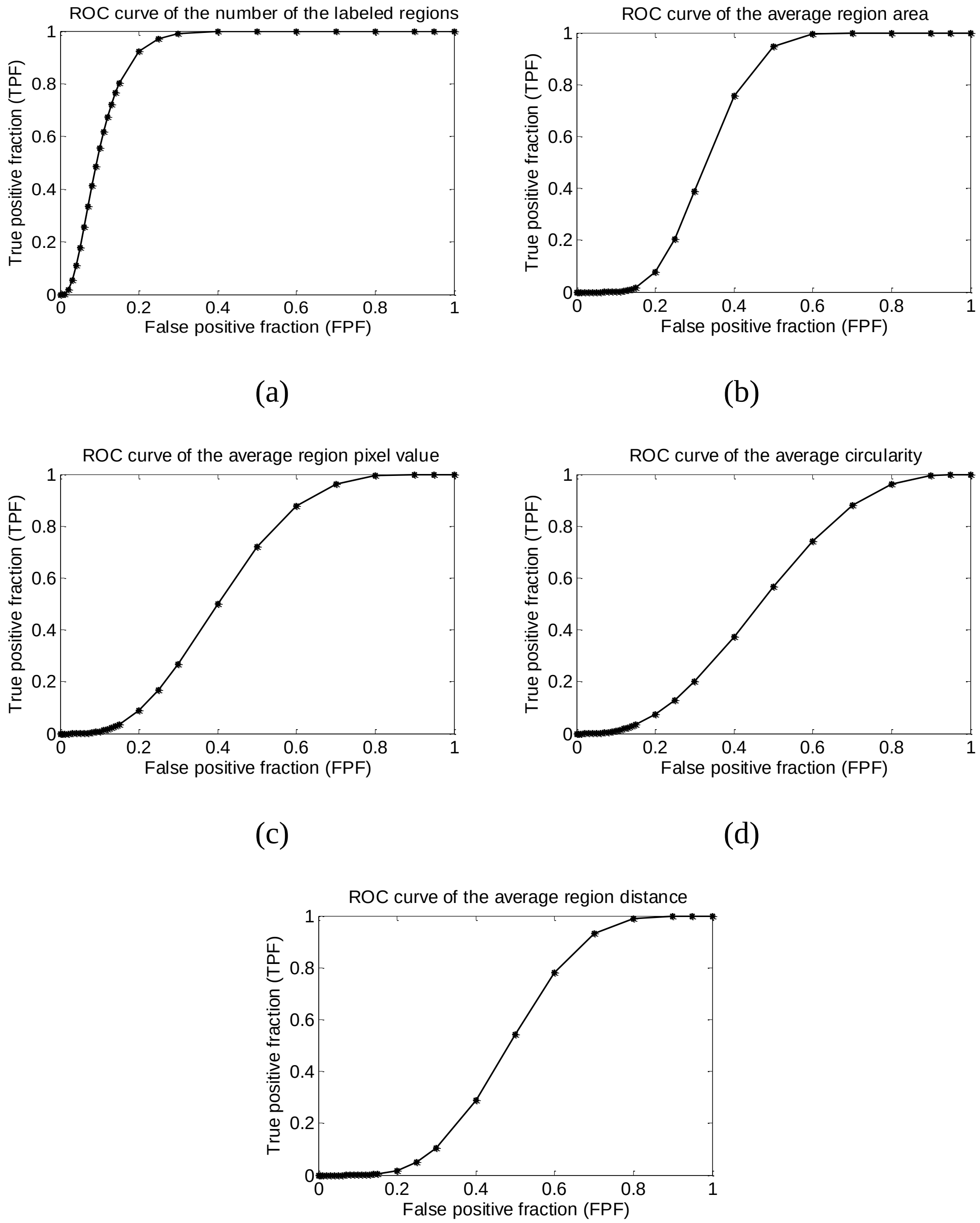

(a) (b)

(c) (d)

(e)

Figure 44: The estimated ROC curve for different extracted features

These features are (a) number of labeled regions (b) average region area (c) average region pixel intesity (d) average region circulairity and (e) average region distance. Accordingly, the calculated area under curve (AUC) are (a) 0.896±0.023 (b) 0.666±0.037 (c) 0.592±0.039 (d) 0.531±0.040 (e) 0.516±0.039, respectively.

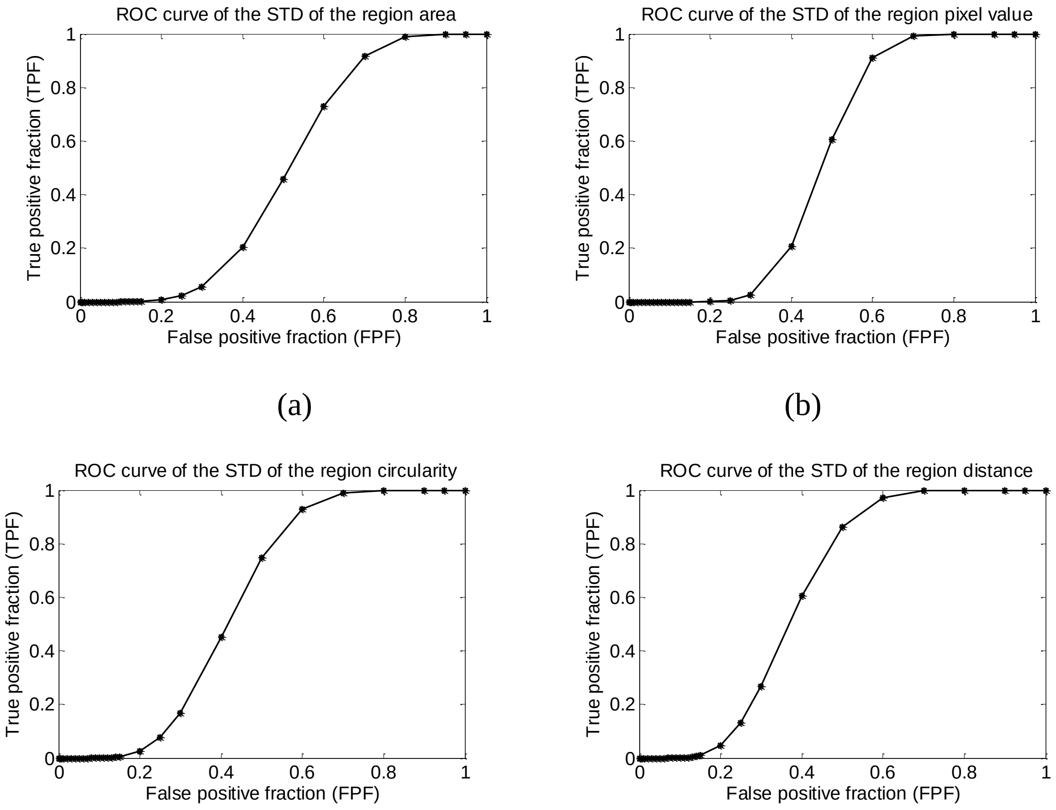

(a) (b)

(c) (d)

Figure 45: The ROC of the standard deviation of different features

These features include (a) region area (b) region pixel intensity (c) region circularity (d) region distance. The AUC of the ROC curves are (a) 0.486±0.039 (b) 0.524±0.039 (c) 0.581±0.039 (d) 0.625±0.038.

Table 9 shows the correlation coefficient between each pair of the investigated features. The data demonstrate that the number of the labeled regions, average region area, and average region pixel value are relatively independent features, as the correlation coefficient between these features are smaller than 0.5. The STD of the region circularity and the STD of the region distance are related with each other, but each of these two features is also independent with the other three features (number of the labeled regions, average region area, and average region pixel value).

For the high throughput scanning, both the on-line and off-line CAD schemes are applied [7]. The on-line CAD scheme synchronizes with the high speed image scanning process and initially detects the analyzable cells, while the off-line CAD scheme is applied after scanning, to further select the analyzable images on the results firstly processed by the on-line scheme. Since the number of the labeled regions has better performance than the other eight features, it is suggested as the only feature for the on line CAD scheme, to satisfy the real time requirement. After the online processing, a number of 1000-3000 ROIs are saved [7], among which only 10-30 ROIs contain analyzable metaphase cells for the following diagnosis. Thus the off-line CAD scheme requires high specificity to discard most of the false positive images selected by the on line CAD scheme. Furthermore, using the modern classifiers, the CAD scheme is able to combine more than one extracted features, to achieve a better accuracy [73-75, 142]. As mentioned before, we do not need to apply both the STD of the region distance and circularity because they are correlated features. Therefore, for the off-line CAD schemes, a combination of four features is recommended, which includes number of the labeled regions, average region area, average region pixel value, and standard deviation of either region distance or circularity.

Table 8: The estimated p-value of the difference significance between the features

	Number of the labeled regions	Average region area	Average pixel value	STD of the region circularity	STD of the region distance
Number of the labeled regions	1	0	0	0	0
Average region area	0	1	0.1873	0.1484	0.4652
Average pixel value	0	0.1873	1	0.6576	0.6230
STD of the region circularity	0	0.1484	0.6576	1	0.3284
STD of the region distance	0	0.4652	0.6230	0.3284	1

Table 9: The estimated correlation coefficients among different features

	Number of the labeled regions	Average region area	Average pixel value	STD of the region circularity	STD of the region distance
Number of the labeled regions	1	0.3253	0.1567	0.2939	0.3467
Average region area	0.3253	1	-0.0151	-0.1524	-0.1038
Average pixel value	0.1567	-0.0151	1	0.3698	0.3334
STD of the region circularity	0.2939	-0.1524	0.3698	1	0.6058
STD of the region distance	0.3467	-0.1038	0.3334	0.6058	1

9.5 Discussion

High throughput scanning microscopy is a promising method to digitalize the cells depicted on the clinical slides. Since only a small amount of cells contained on the slide are actually analyzable for the diagnosis, a CAD scheme is needed to select the ROIs depicting clinically analyzable chromosomes for the following diagnosis. For the development of a robust CAD schemes, the feature selection is critically important, which may directly determine the final performance of the CAD scheme. Thus the CAD designers need to carefully select the most suitable features, to satisfy the different requirements of the various CAD schemes.

In the last several years, many feature extraction methods are reported, which can effectively identify the pathologically analyzable metaphase chromosomes [27-29, 78, 125]. However, we cannot directly compare the reported results, as these features were applied on the different datasets and assessed by the different standards.

In this study, 9 different feature extraction methods were investigated, under the condition of high throughput scanning prototype. A number of 200 bone marrow cells including 67 clinically meaningful chromosomes were first acquired. Then these cell images were processed and the feature extraction methods were applied for each acquired image. After that, the images were classified into analyzable and un-analyzable groups, using each feature extraction method. The performance of each feature was assessed by the ROC curve. The result shows that extracting number of the labeled regions is suitable for the on-line CAD scheme. For the off line CAD scheme, combining four features is recommended, which includes the number of the labeled regions, average region area, average region pixel value, and the deviation of the either region circularity or distance.

As an initial study, however, this investigation has several limitations. First, the performance of the classifiers was not assessed. Different classifiers, such as decision tree [142], support vector machine [74], fuzzy ARTMAP [73], native Bayesian classifier [75], may affect the performance of the final CAD schemes when using more than one features. Second, we did not discuss the overall performance difference between the manual and automatic scanning systems. Thus a more comprehensive study is prepared, which may be able to improve the accuracy of the high throughput scanning systems in the future.

Chapter 10: Conclusion and discussion

10.1 Summary

High throughput scanning microscopy is a recently developed scanning technique, which might be widely applied in the future. In medical imaging lab, University of Oklahoma, a prototype of high throughput microscopic scanning system was developed. The entire system was built upon a commercial transmitted light microscope. On this microscope, a new type of TDI line scanning camera was installed to acquire high resolution moving cells depicted on the specimen. A high precision moving stage is also utilized to hold the specimen, and both the camera and moving stage are synchronized by a computer. Two different CAD modules are applied to select the clinically meaningful cells among all the obtained images.

For the high throughput scanning technique, however, there are several technical challenges. First, we need to compare the performance of this new scanning method with the conventional two-step scanners. Second, the DOF impact is necessary to be examined using the clinically analyzable metaphase chromosomes and the auto-focusing methods should be carefully assessed to achieve the satisfactory results. Third, we need to optimize scanning scheme to balance the image quality and efficiency. Finally, classification accuracy of image features should be evaluated uniformly the under the high throughput scanning condition.

This dissertation is composed of 6 investigations aiming to evaluate and optimize the performance of the high throughput scanning microscopic scanning system. The first investigation was designed to solve the first technical challenge, which utilized a total of 9 slides obtained from five patients to compare the system performance of the high throughput scanning prototype with the conventional scanners.

The second and third studies were performed for the second technical challenge. In the second study, we first computed DOF using a well-recognized theoretic model of an optical image system and then measured DOF of the same optical system using a standard test bar pattern target. After that, we analyzed DOF (by obtaining cytogenetic images under our developed prototype using two objective lenses of 60× (dry, N.A. = 0.95) and 100× (oil, N.A. = 1.25). In the third study, five auto-focusing functions were tested and compared on metaphase chromosome images obtained from bone marrow and blood specimens. Four different criteria were applied to assess the performance of these methods.

The fourth and fifth investigations were targeted to the third technical challenge. The forth study utilized a gradient sharpness function to objectively assess the chromosome band sharpness. The standard resolution target and several pathological chromosomes were imaged at different scanning speeds, and the sharpness is objectively evaluated by the gradient sharpness function. The fifth study analyzed a sampling-focusing method, which only applies the auto-focusing operations on a limited number of locations of the imaging field. For the rest of the imaging field, the focusing position is adjusted very quickly through linear interpolation.

The forth technical challenge was examined by the sixth study. In this study, 9 different feature extraction methods were investigated, under the condition of high throughput scanning prototype. A number of 200 bone marrow cells including 67 clinically meaningful chromosomes were first acquired. Then these cell images were processed and the feature extraction methods were applied for each acquired image. After that, the images were classified into analyzable and un-analyzable groups, using each feature extraction method. The classification performance of each feature was assessed by the ROC curve.

10.2 Original contributions

This dissertation has the following original contributions. First, we preliminarily demonstrated that high throughput scanner can detect more clinically meaningful metaphase cells than clinicians do in six out of the seven slides. These images were presented with adequate contrast and sharpness for further pathological interpretation.

Second, our results in the dissertation showed that the experimentally measured DOF was substantially greater than that computed by the theoretic model. For the commonly cytogenetic specimens, the chromosome band depicted on the acquired images remained analyzable if the specimen were placed within the range of 1.5 or 1.0 μm away from the focal plane when using the two 60× or 100× objective lenses, respectively. Furthermore, in order to maintain the specimen in focus, the Brenner gradient and threshold pixel counting methods were suggested as the most suitable auto-focusing functions for the bone marrow and blood sample scanning, respectively.

Third, we showed that that the captured image sharpness is optimized at 0.6 and 0.8 mm/s, for the resolution target and metaphase chromosomes, respectively. Placing the auto-focusing positions with a distance of 6.9 cm, the prototype could obtain the adequate number of clinically meaningful cells from blood specimens. Using more auto-focusing operations is also meaningful for the high reliability diagnosis when clinically necessary.

Finally, we recommended that extracting number of the labeled regions is suitable for the on-line CAD scheme. For the off line CAD scheme, four different features are suggested, which are the number of the labeled regions, average region area, average region pixel value, and the deviation of the either region circularity or distance.

10.3 Discussion and future study

The investigations in this dissertation have several limitations and a series of further studies can be conducted based on our results. First, we should investigate the impact of the DOF of human eye [99, 100] and the sample thickness on the off-focusing tolerance of the metaphase chromosomes [93]. Second, more recently proposed algorithms should be considered in a more comprehensive assessment of the optimal selection of the auto focusing methods [101, 118-120]. Similarly, using the ROC method, we can assess more modern image features for the CAD modules [4].

Furthermore, this high throughput prototype can be improved in several different ways. On our prototype, the auto-focusing operation is applied on a number of sampled locations, to balance the image quality and scanning efficiency [12]. The system performance, including the image quality and scanning efficiency, can be vastly improved by dynamically adjusting the z-axis position during the continuous scanning. A dynamic auto-focusing method based on the TDI detector was reported by Bravo-Zanoguera and Laris in 2007 [103]. However, this method employs 9 independent optical fiber coupled CCD detectors, which is too expensive and complicated. Thus, developing a low cost dynamic auto-focusing technique is meaningful for the high throughput scanning system.

Recently, more and more interests are focused on digitalize and display the image of the entire slide for diagnosing and reviewing purpose [143-145]. Currently, we did not using the high throughput prototype to scan and store the whole slide imaging (WSI) of the chromosome specimens. Given that most of the current whole slide imaging (WSI) were conducted under 20× or 40× objective lenses [143], one of the technical challenges is to screen and store the high magnification (60× or 100×) whole slide images. According to our studies, both these two lenses have very similar resolving powers (0.353 μm for 60× and 0.268 μm for the 100× lenses) and the captured images can be used for the diagnosis with acceptable quality degradation [9]. Given that the total size of the 60× WSI is much smaller than the 100× WSI, the diagnosis efficacy should be assessed and validated under the condition of applying the 60× lens.

In addition, a more comprehensive study is necessary to be carried on to determine whether the visual specimen screening can be replaced by the digital WSI for the diagnosis of chromosome aberrations. Since the size of the WSI is much larger than the traditionally captured images, the WSI management and interpretation is a typical “big data” problem, which requires the data mining techniques to extract the meaningful information for the clinical practice [142]. However, only few research efforts have been conducted in this emerging area.

The high throughput scanning can also be applied on the FISH slides. The FISH technique can examine both interphase and metaphase chromosomes. But more technical challenges are associated with the optical path and hardware design of the FISH image scanning system, which must capture the fluorescent signals from multiple frequency channels. Fortunately, the hardware complexity can be significantly simplified by applying the new fluorescent biomarkers such as quantum dots [146-148], because quantum dots have very wide exciting spectrum and narrow emitting spectrum.

Identifying the abnormalities of the band patterns or dot numbers is a “course” technique, as a large amount of DNA aberration might occur when these abnormalities are detected. At present, fast developing DNA sequencing technique provides a new way to precisely locate the aberrant DNA segments [149]. A number of research studies have been reported on using the DNA sequence to diagnose different kind of cancers [150-153]. In addition, many DNA sequence analyzing techniques in bioinformatics can be utilized for the computer aided cancer identification based on the DNA sequence [154-158]. Another interesting topic is how to combine the cell level and molecular level information together for the clinical diagnosis.

In summary, we believe that the various genome aberration detecting techniques may hold a prosperous potential for extensive diagnostic applications in the future.

References

[1] J. H. Tjio, and A. Levan, "The chromosome number of man", Hereditas, **42**(1-2), 1-6, (1956).

[2] J. Lejeune, M. Gautier, and R. Turpin, "Etude des chromosomes somatiques de neuf enfants mongoliens", Comptes Rendus Hebdomadaires Des Seances De L Academie Des Sciences, **248**(11), 1721-1722, (1959).

[3] P. C. Nowell, and D. A. Hungerford, "Minute chromosome in human chronic granulocytic leukemia ", Science, **132**(3438), 1497-1497, (1960).

[4] X. W. Wang, B. Zheng, et al., "Development and evaluation of automated systems for detection and classification of banded chromosomes: Current status and future perspectives", Journal of Physics D: Applied Physics, **38**(15), 2536-2542, (2005).

[5] J. Piper, E. Granum, D. Rutovitz, and H. Ruttledge, "Automation of chromosome analysis ", Signal Processing, **2**(3), 203-221, (1980).

[6] K. Truong, A. Gibaud, et al., "Quantitative fish determination of chromosome 3 arm imbalances in lung tumors by automated image cytometry", Medical Science Monitor, **10**(11), 426-432, (2004).

[7] Y. C. Qiu, X. W. Wang, et al., "Automated detection of analyzable metaphase chromosome cells depicted on scanned digital microscopic images", Proc. SPIE **7627**, 7627181-9 (2010).

[8] Y. C. Qiu, X. D. Chen, et al., "The impact of the depth of field on cytogenetic image quality in scanning microscopy", Proc. SPIE **7900**, 79000D1-5 (2011).

[9] Y. C. Qiu, X. D. Chen, et al., "The impact of the optical depth of field on cytogenetic image quality in scanning microscopy", Journal of Biomedical Optics, **17**(9), 0960171-7, (2012).

[10] Y. C. Qiu, X. D. Chen, et al., "Evaluations of auto-focusing methods under a microscopic imaging modality for metaphase chromosome image analysis", Analytical Cellular Pathology, **36**(1-2), 37-44, (2013).

[11] Y. Qiu, Y. Li, et al., "Objective evaluation of the microscopic image sharpness for diagnostic metaphase chromosomes", **8582**, 85820I-85820I-5 (2013).

[12] Y. C. Qiu, X. D. Chen, et al., "An automatic scanning method for high throughput microscopic system to facilitate medical genetic diagnosis: An initial study", Proc. of SPIE **8224**, 82240E1-5 (2012).

[13] L. E. Rosenberg, and D. D. Rosenberg, *Human genes and genomes*. 1 ed. 2012, San Diego, CA: Academic Press.

[14] E. F. Delong, G. S. Wickham, and N. R. Pace, "Phylogenetic stains - ribosomal rna-based probes for the identification of single cells", Science, **243**(4896), 1360-1363, (1989).

[15] R. I. Amann, L. Krumholz, and D. A. Stahl, "Fluorescent-oligonucleotide probing of whole cells for determinative, phylogenetic and environmental-stydies in microbiology", Journal of Bacteriology, **172**(2), 762-770, (1990).

[16] J. Philip, T. Bryndorf, and B. Christensen, "Prenatal aneuploidy detection in interphase cells by fluorescent in-situ hybridization ", Prenatal Diagnosis, **14**(13), 1203-1215, (1994).

[17] A. P. Landstrom, and A. Tefferi, "Fluorescent in situ hybridization in the diagnosis, prognosis, and treatment monitoring of chronic myeloid leukemia", Leukemia & Lymphoma, **47**(3), 397-402, (2006).

[18] R. Amann, and B. M. Fuchs, "Single-cell identification in microbial communities by improved fluorescence in situ hybridization techniques", Nature Reviews Microbiology, **6**(5), 339-348, (2008).

[19] X. W. Wang, B. Zheng, et al., "Automated detection and analysis of fluorescent in situ hybridization spots depicted in digital microscopic images of pap-smear specimens", Journal of Biomedical Optics, **14**(2), (2009).

[20] G. M. Hampton, A. A. Larson, et al., "Simultaneous assessment of loss of heterozygosity at multiple microsatellite loci using semi-automated fluorescence-based detection: Subregional mapping of chromosome 4 in cervical carcinoma", Proceedings of the National Academy of Sciences of the United States of America, **93**(13), 6704-6709, (1996).

[21] B. Kajtar, G. Mehes, et al., "Automated fluorescent in situ hybridization (fish) analysis of t(9;22)(q34;q11) in interphase nuclei", Cytometry Part A, **69A**(6), 506-514, (2006).

[22] M. M. Lebeau, and J. D. Rowley, "Recurring chromosomal-abnormalities in leukemia and lymphoma", Cancer Surveys, **3**(3), 371-394, (1984).

[23] K. H. P. Harnden D.G., Jensen J.T., Kaelbling M. , [An international system for human cytogenetic nomenclature(iscn1985): Report of the standing committee on human cytogenetic nomenclature]. KAEGER, Basel, Switzerland (1985).

[24] C. Mian, D. Bancher, et al., "Fluorescence in situ hybridization in cervical smears: Detection of numerical aberrations of chromosomes 7, 3, and x and relationship to hpv infection", Gynecologic Oncology, **75**(1), 41-46, (1999).

[25] L. J. Van Vliet, I. T. Young, and B. H. Mayall, "The athena semi-automated karyotyping system", Cytometry, **11**(1), 51-58, (1990).

[26] G. Corkidi, L. Vega, et al., "Roughness feature of metaphase chromosome spreads and nuclei for automated cell proliferation analysis", Medical & Biological Engineering & Computing, **36**(6), 679-685, (1998).

[27] F. A. Cosio, L. Vega, et al., "Automatic identification of metaphase spreads and nuclei using neural networks", Medical & Biological Engineering & Computing, **39**(3), 391-396, (2001).

[28] X. W. Wang, S. B. Li, et al., "A computer-aided method to expedite the evaluation of prognosis for childhood acute lymphoblastic leukemia", Technology in Cancer Research & Treatment, **5**(4), 429-436, (2006).

[29] X. W. Wang, S. B. Li, et al., "Automated identification of analyzable metaphase chromosomes depicted on microscopic digital images", Journal of Biomedical Informatics, **41**(2), 264-271, (2008).

[30] X. W. Wang, B. Zheng, et al., "Automated classification of metaphase chromosomes: Optimization of an adaptive computerized scheme", Journal of Biomedical Informatics, **42**(1), 22-31, (2009).

[31] X. W. Wang, B. Zheng, et al., "Automated analysis of fluorescent in situ hybridization (fish) labeled genetic biomarkers in assisting cervical cancer diagnosis", Technology in Cancer Research & Treatment, **9**(3), 231-242, (2010).

[32] A. R. Weeks, H. R. Myler, and H. G. Wenaas, "Computer-generated noise images for the evaluation of image-processing algorithms", Optical Engineering, **32**(5), 982-992, (1993).

[33] E. Grisan, E. Poletti, and A. Ruggeri, "Automatic segmentation and disentangling of chromosomes in q-band prometaphase images", IEEE Transactions on Information Technology in Biomedicine, **13**(4), 575-581, (2009).

[34] C. M. Li, C. Y. Kao, J. C. Gore, and Z. H. Ding, "Minimization of region-scalable fitting energy for image segmentation", IEEE Transactions on Image Processing, **17**(10), 1940-1949, (2008).

[35] E. Poletti, F. Zappelli, A. Ruggeri, and E. Grisan, "A review of thresholding strategies applied to human chromosome segmentation", Computer Methods and Programs in Biomedicine, **108**(2), 679-688, (2012).

[36] L. Ji, "Fully-automatic chromosome segmentation", Cytometry, **17**(3), 196-208, (1994).

[37] G. Agam, and I. Dinstein, "Geometric separation of partially overlapping nonrigid objects applied to automatic chromosome classification", IEEE Transactions on Pattern Analysis and Machine Intelligence, **19**(11), 1212-1222, (1997).

[38] C. U. Garcia, A. B. Rubio, F. A. Perez, and F. S. Hernandez, "A curvature-based multiresolution automatic karyotyping system", Machine Vision and Applications, **14**(3), 145-156, (2003).

[39] G. C. Charters, and J. Graham, "Trainable grey-level models for disentangling overlapping chromosomes", Pattern Recognition, **32**(8), 1335-1349, (1999).

[40] G. C. Charters, and J. Graham, "Disentangling chromosome overlaps by combining trainable shape models with classification evidence", IEEE Transactions on Signal Processing, **50**(8), 2080-2085, (2002).

[41] G. Ritter, and L. Gao, "Automatic segmentation of metaphase cells based on global context and variant analysis", Pattern Recognition, **41**(1), 38-55, (2008).

[42] A. Carothers, and J. Piper, "Computer-aided classification of human-chromosomes - a review", Statistics and Computing, **4**(3), 161-171, (1994).

[43] R. J. Stanley, J. M. Keller, P. Gader, and C. W. Caldwell, "Data-driven homologue matching for chromosome identification", IEEE Transactions on Medical Imaging, **17**(3), 451-462, (1998).

[44] S. Ryu, "A study for the feature selection to identify giemsa-stained human chromosomes based on artificial neural network", Proceedings of the 23rd Annual International Conference of the Engineering in Medicine and Biology Society, 691-692 (2001).

[45] J. M. Cho, "Chromosome classification using backpropagation neural networks - a process that overcomes nonlinearity problems to correctly classify giemsa-stained human chromosomes", IEEE Engineering in Medicine and Biology Magazine, **19**(1), 28-33, (2000).

[46] J. Piper, and E. Granum, "On fully-automatic feature measurement for banded chromosome classification", Cytometry, **10**(3), 242-255, (1989).

[47] M. C. Morrone, and D. C. Burr, "Feature detection in human vision: A phase-dependent energy model", Proceedings of the Royal Society B:Biological Sciences, **235**(1280), 221-245, (1988).

[48] X. W. Feng, P. S. Cong, Z. L. Zhu, and X. Y. Du, "Automated pairing of human chromosomes applying gradient profile and similarity matching algorithm", Chemometrics and Intelligent Laboratory Systems, **111**(1), 46-52, (2012).

[49] X. Wang, B. Zheng, et al., "A rule-based computer scheme for centromere identification and polarity assignment of metaphase chromosomes", Computer Methods and Programs in Biomedicine, **89**(1), 33-42, (2008).

[50] A. S. Arachchige, J. Samarabandu, J. H. M. Knoll, and P. K. Rogan, "Intensity integrated laplacian-based thickness measurement for detecting human metaphase chromosome centromere location", IEEE Transactions on Biomedical Engineering, **60**(7), 2005-2013, (2013).

[51] X. W. Wang, B. Zheng, et al., "Automated identification of abnormal metaphase chromosome cells for the detection of chronic myeloid leukemia using microscopic images", Journal of Biomedical Optics, **15**(4), (2010).

[52] X. Ruan, "A classifier with the fuzzy hopfield network for human chromosomes", Proceedings of the 3rd World Congress on Intelligent Control and Automation **2**, 1159-1164 (2000).

[53] M. Moradi, and S. K. Setarehdan, "New features for automatic classification of human chromosomes: A feasibility study", Pattern Recognition Letters, **27**(1), 19-28, (2006).

[54] Z. Z. Kou, L. Ji, and X. G. Zhang, "Karyotyping of comparative genomic hybridization human metaphases by using support vector machines", Cytometry, **47**(1), 17-23, (2002).

[55] O. Sjahputera, and J. M. Keller, "Evolution of a fuzzy rule-based system for automatic chromosome recognition", IEEE International Fuzzy Systems Conference Proceedings **1**, 129-134 (1999).

[56] M. Bass, [Chapter 28, handbook of optics]. McGraw-Hill Companies, New York 28.18-23 (2010).

[57] H. Netten, Young, I. T., vanVliet, L. J. ,Tanke, H. J. ,Vroljik, H. ,Sloos, W. C. R., "Fish and chips: Automation of fluorescent dot counting in interphase cell nuclei", Cytometry, **28**(1), 1-10, (1997).

[58] G. W. Zack, J. A. Spriet, et al., "Automatic detection and localization of sister chromatid exchanges ", Journal of Histochemistry & Cytochemistry, **24**(1), 168-177, (1976).

[59] T. W. Ridler, Calvard, S., "Picture thresholding using an iterative selection method", IEEE Transactions on Systems Man and Cybernetics, **8**(8), 630-632, (1978).

[60] F. Meyer, "Iterative image transformations for an automatic screening of cervical smears ", Journal of Histochemistry & Cytochemistry, **27**(1), 128-135, (1979).

[61] L. J. v. Vliet, I. T. Young, and G. L. Beckers, "A nonlinear laplace operator as edge detector in noisy images", Comput. Vision Graph. Image Process., **45**(2), 167-195, (1989).

[62] C. O. de Solorzano, A. Santos, et al., "Automated fish spot counting in interphase nuclei: Statistical validation and data correction", Cytometry, **31**(2), 93-99, (1998).

[63] F. Raimondo, M. A. Gavrielides, et al., "Automated evaluation of her-2/neu status in breast tissue from fluorescent in situ hybridization images", IEEE Transactions on Image Processing, **14**(9), 1288-1299, (2005).

[64] J. N. O'Sullivan, J. C. Finley, et al., "Telomere length assessment in tissue sections by quantitative fish: Image analysis algorithms", Cytometry Part A, **58A**(2), 120-131, (2004).

[65] S. Shah, "Image enhancement for increased dot-counting efficiency in fish", Journal of Microscopy-Oxford, **228**(2), 211-226, (2007).

[66] L. Meylan, and S. Susstrunk, "High dynamic range image rendering with a retinex-based adaptive filter", IEEE Transactions on Image Processing, **15**(9), 2820-2830, (2006).

[67] Z. Li, S. B. Li, et al., "Potential clinical impact of three-dimensional visualization for fluorescent in situ hybridization image analysis", Journal of Biomedical Optics, **17**(5), (2012).

[68] M. Gue, C. Messaoudi, J. S. Sun, and T. Boudier, "Smart 3d-fish: Automation of distance analysis in nuclei of interphase cells by image processing", Cytometry Part A, **67A**(1), 18-26, (2005).

[69] M. K. Chawla, G. Lin, et al., "3d-catfish: A system for automated quantitative three-dimensional compartmental analysis of temporal gene transcription activity imaged by fluorescence in situ hybridization", Journal of Neuroscience Methods, **139**(1), 13-24, (2004).

[70] M. Kozubek, S. Kozubek, et al., "High-resolution cytometry of fish dots in interphase cell nuclei", Cytometry, **36**(4), 279-293, (1999).

[71] B. Lerner, W. F. Clocksin, et al., "Feature representation and signal classification in fluorescence in-situ hybridization image analysis", IEEE Transactions on Systems Man and Cybernetics Part a-Systems and Humans, **31**(6), 655-665, (2001).

[72] G. A. Carpenter, S. Grossberg, and J. H. Reynolds, "Artmap - supervised real-time learning and classification of nonstationary data by a self-organizing neural network", Neural Networks, **4**(5), 565-588, (1991).

[73] B. Vigdor, and B. Lerner, "Accurate and fast off and online fuzzy artmap-based image classification with application to genetic abnormality diagnosis", IEEE Transactions on Neural Networks, **17**(5), 1288-1300, (2006).

[74] A. David, and B. Lerner, "Support vector machine-based image classification for genetic syndrome diagnosis", Pattern Recognition Letters, **26**(8), 1029-1038, (2005).

[75] B. Lerner, "Bayesian fluorescence in situ hybridisation signal classification", Artificial Intelligence in Medicine, **30**(3), 301-316, (2004).

[76] H. S. Wong, Y. L. Yao, and E. S. Schlig, "Tdi charge-coupled-devices - design and applications", Ibm Journal of Research and Development, **36**(1), 83-106, (1992).

[77] I. C. Baykal, and G. A. Jullien, "Self-synchronization of time delay and integration cameras", Journal of Electronic Imaging, **13**(4), 680-687, (2004).

[78] X. W. Wang, B. Zheng, et al., "Development and assessment of an integrated computer-aided detection scheme for digital microscopic images of metaphase chromosomes", Journal of Electronic Imaging, **17**(4), 043008, (2008).
[79] R. C. Gonzalez, and R. E. Woods, [Digital image processing]. Prentice Hall, Upper Saddle River, NJ (2002).
[80] B. Zheng, A. Lu, et al., "A method to improve visual similarity of breast masses for an interactive computer-aided diagnosis environment", Medical Physics, **33**(1), 111-117, (2006).
[81] A. V. Oppenheim, and A. S. Willsky, [Signals and systems]. Prentice Hall (1996).
[82] W. Mao, "Optical engineering fundamentals", 181-184, (2006).
[83] S. K. Inoue S [Video microscopy: The fundamentals]. Plenum New York and London (1997).
[84] P. Horst, [Microscope photometry]. Springer, New York and Berlin (1977).
[85] L. C. Martin, [The theory of microscope]. Elsevier, New York (1966).
[86] H. H. Hopkins, "The frequency response of a defocused optical system", Proceedings of the Royal Society of London. Series A, Mathematical and Physical Sciences, **231**(1184), 91-103, (1955).
[87] P. A. Stokseth, "Properties of a defocused optical system", Journal of the Optical Society of America, **59**(10), 1314-1321, (1969).
[88] M. C. Wood, X. W. Wang, et al., "Using contrast transfer function to evaluate the effect of motion blur on microscope image quality", Proc. SPIE **6857**, 68570F1-8 (2008).
[89] C. J. R. Sheppard, "Defocused transfer function for a partially coherent microscope and application to phase retrieval", Journal of the Optical Society of America A: Optics Image Science and Vision, **21**(5), 828-831, (2004).
[90] A. N. Simonov, and M. C. Rombach, "Asymptotic behavior of the spatial frequency response of an optical system with defocus and spherical aberration", Journal of the Optical Society of America A: Optics Image Science and Vision, **27**(12), 2563-2573, (2010).
[91] W. J. Smith, [Modern optical engineering]. McGraw-Hill, New York (2008).
[92] B. Bradie, [A friendly introduction to numerical analysis]. Pearson, New York (2006).
[93] A. Yamamoto, K. Takemoto, et al., "Imaging of chromosomes at nanometer-scale resolution using soft x-ray microscope at ritsumeikan university sr center", Journal of Physics, **Conference Series 186**, (2009).
[94] G. D. Boreman, and S. Yang, "Modulation transfer function measurement using 3-bar and 4-bar targets. ", Applied Optics, **34**(34), 8050-8052, (1995).
[95] D. N. Sitter, J. S. Goddard, and R. K. Ferrell, "Method for the measurement of the modulation transfer function of sampled imageing systems from bar-target patterns. ", Applied Optics, **34**(4), 746-751, (1995).
[96] E. Marom, B. Milgrom, and N. Konforti, "Two-dimensional modulation transfer function: A new perspective", Applied Optics, **49**(35), 6749-6755, (2010).

[97] P. D. Lin, and C. S. Liu, "Geometrical mtf computation method based on the irradiance model", Applied Physics B-Lasers and Optics, **102**(1), 243-249, (2011).

[98] P. D. Lin, and W. Wu, "Calculation of the modulation transfer function for object brightness distribution function oriented along any direction in axis-symmetrical optical systems", Applied Optics, **50**(17), 2759-2772, (2011).

[99] S. Marcos, E. Moreno, and R. Navarro, "The depth-of-field of the human eye from objective and subjective measurements", Vision Research, **39**(12), 2039-2049, (1999).

[100] Y. K. Nio, N. M. Jansonius, et al., "Spherical and irregular aberrations are important for the optimal performance of the human eye", Ophthalmic and Physiological Optics, **22**(2), 103-112, (2002).

[101] S. Yazdanfar, K. B. Kenny, et al., "Simple and robust image-based autofocusing for digital microscopy", Optics Express, **16**(12), 8670-8677, (2008).

[102] S. Yousefi, M. Rahman, and N. Kehtarnavaz, "A new auto-focus sharpness function for digital and smart-phone cameras", IEEE Transactions on Consumer Electronics, **57**(3), 1003-1009, (2011).

[103] M. E. Bravo-Zanoguera, C. A. Laris, et al., "Dynamic autofocus for continuous-scanning time-delay-and-integration image acquisition in automated microscopy", Journal of Biomedical Optics, **12**(3), 034011-16, (2007).

[104] J. F. Brenner, B. S. Dew, et al., "Automated microscope for cytologic research - preliminary evaluation", Journal of Histochemistry & Cytochemistry, **24**(1), 100-111, (1976).

[105] D. Vollath, "The influence of the scene parameters and of noise on the behavior of automatic focusing algorithms", Journal of Microscopy, **151**, 133-146, (1988).

[106] T. T. E. Yeo, S. H. Ong, Jayasooriah, and R. Sinniah, "Autofocusing for tissue microscopy", Image and Vision Computing, **11**(10), 629-639, (1993).

[107] J. Jeon, J. Lee, and J. Paik, "Robust focus measure for unsupervised auto-focusing based on optimum discrete cosine transform coefficients", IEEE Transactions on Consumer Electronics, **57**(1), 1-5, (2011).

[108] F. C. A. Groen, I. T. Young, and G. Ligthart, "A comparison of different focus functions for use in autofocus algorithms", Cytometry, **6**(2), 81-91, (1985).

[109] L. Firestone, K. Cook, et al., "Comparison of autofocus methods for automated microscopy ", Cytometry, **12**(3), 195-206, (1991).

[110] A. Santos, C. O. De Solorzano, et al., "Evaluation of autofocus functions in molecular cytogenetic analysis", Journal of Microscopy, **188**, 264-272, (1997).

[111] Y. Sun, S. Duthaler, and B. J. Nelson, "Autofocusing in computer microscopy: Selecting the optimal focus algorithm", Microscopy Research and Technique, **65**(3), 139-149, (2004).

[112] X. Y. Liu, W. H. Wang, and Y. Sun, "Dynamic evaluation of autofocusing for automated microscopic analysis of blood smear and pap smear", Journal of Microscopy, **227**(1), 15-23, (2007).

[113] O. A. Osibote, R. Dendere, S. Krishnan, and T. S. Douglas, "Automated focusing in bright-field microscopy for tuberculosis detection", Journal of Microscopy, **240**(2), 155-163, (2010).

[114] J. M. Mateos-Perez, R. Redondo, et al., "Comparative evaluation of autofocus algorithms for a real-time system for automatic detection of mycobacterium tuberculosis", Cytometry Part A, **81A**(3), 213-221, (2012).

[115] H. Xie, W. B. Rong, and L. N. Sun, "Construction and evaluation of a wavelet-based focus measure for microscopy imaging", Microscopy Research and Technique, **70**(11), 987-995, (2007).

[116] Y. Ge, and B. J. Nelson, "Wavelet-based autofocusing and unsupervised segmentation of microscopic images", 2003 IEEE/RSJ International Conference on Intelligent Robots and Systems **3**, 2143-2148 (2003).

[117] J. W. Goodman, [Introduction to fourier optics]. Roberts and Company Publishers, Colorado 145-154 (2004).

[118] M. Zeder, and J. Pernthaler, "Multispot live-image autofocusing for high-throughput microscopy of fluorescently stained bacteria", Cytometry Part A, **75A**(9), 781-788, (2009).

[119] S. Chowdhury, M. Kandhavelu, O. Yli-Harja, and A. S. Ribeiro, "An interacting multiple model filter-based autofocus strategy for confocal time-lapse microscopy", Journal of Microscopy, **245**(3), 265-275, (2012).

[120] M. E. Rudnaya, H. G. ter Morsche, J. M. L. Maubach, and R. M. M. Mattheij, "A derivative-based fast autofocus method in electron microscopy", Journal of Mathematical Imaging and Vision, **44**(1), 38-51, (2012).

[121] D. Boehm, S. Herold, et al., "Rapid detection of subtelomeric deletion/duplication by novel real-time quantitative pcr using sybr-green dye", Human Mutation, **23**(4), 368-378, (2004).

[122] P. G. Engeldrum, "A theory of image quality: The image quality circle", Journal of Imaging Science and Technology, **48**(5), 447-457, (2004).

[123] R. Redondo, G. Bueno, et al., "Quality evaluation of microscopy and scanned histological images for diagnostic purposes", Micron, **43**(2-3), 334-343, (2012).

[124] L. Shih, Wang, TL., "Apply innovative technologies to explore cancer genome", Curr Opin Oncol, **17**(1), 33-8, (2005).

[125] K. R. Castleman, "The psi automatic metaphase finder", Journal of Radiation Research, **33**, 124-128, (1992).

[126] S. H. Park, J. M. Goo, and C. H. Jo, "Receiver operating characteristic (roc) curve: Practical review for radiologists", Korean Journal of Radiology, **5**(1), 11-18, (2004).

[127] X. W. Wang, [Development of a computer-aided chromosome analysis system to assist cancer diagnosis: A dessertation for ph.D degree]. Norman, Oklahoma 111-127 (2008).

[128] J. A. Swets, and R. M. Pickett, *Evaluation of diagnostic systems*. Series in cognition and perception. 1982, New York, New York: Academic press.

[129] C. E. Metz, B. A. Herman, and J. H. Shen, "Maximum likelihood estimation of receiver operating characteristic (roc) curves from continuously-distributed data", Statistics in Medicine, **17**(9), 1033-1053, (1998).

[130] D. P. Chakraborty, "Maximum-likelihood analysis of free-response receiver operating characteristic (froc) data", Medical Physics, **16**(4), 561-568, (1989).

[131] N. A. Obuchowski, "Fundamentals of clinical research for radiologists - roc analysis", American Journal of Roentgenology, **184**(2), 364-372, (2005).

[132] C. E. Metz, "Some practical issues of experimental-design and data-analysis in radiological roc studies", Investigative Radiology, **24**(3), 234-245, (1989).

[133] C. E. Metz, "Roc methodology in radiologic imaging", Investigative Radiology, **21**(9), 720-733, (1986).

[134] J. A. Swets, "Form of empirical rocs in discrimination and diagnostic tasks - implications for theory and measurement of performance", Psychological Bulletin, **99**(2), 181-198, (1986).

[135] J. A. Hanley, "The robustness of the binormal assumptions used in fitting roc curves", Medical Decision Making, **8**(3), 197-203, (1988).

[136] K. O. HajianTilaki, J. A. Hanley, L. Joseph, and J. P. Collet, "A comparison of parametric and nonparametric approaches to roc analysis of quantitative diagnostic tests", Medical Decision Making, **17**(1), 94-102, (1997).

[137] D. D. Dorfman, and E. Alf, "Maximum-likelihood estimation of parameters of signal-detection theory and determination of confidence intervals - rating-method data", Journal of Mathematical Psychology, **6**(3), 487-&, (1969).

[138] D. R. Grey, and B. J. T. Morgan, "Some aspects of roc curve-fitting - normal and logistic models", Journal of Mathematical Psychology, **9**(1), 128-&, (1972).

[139] C. Metz, P.-L. Wang, and H. Kronman, *A new approach for testing the significance of differences between roc curves measured from correlated data*, in *Information processing in medical imaging*, Deconinck, F., Editor. 1984, Springer Netherlands. p. 432-445.

[140] T. Fawcett, "An introduction to roc analysis", Pattern Recognition Letters, **27**(8), 861-874, (2006).

[141] C. E. Metz, B. A. Herman, and C. A. Roe, "Statistical comparison of two roc-curve estimates obtained from partially-paired datasets", Medical Decision Making, **18**(1), 110-121, (1998).

[142] T. M. Mitchell, [Machine learning]. McGraw-Hill, Boston (1997).

[143] T. C. Cornish, R. E. Swapp, and K. J. Kaplan, "Whole-slide imaging: Routine pathologic diagnosis", Advances in Anatomic Pathology, **19**(3), 152-159, (2012).

[144] L. Pantanowitz, J. H. Sinard, et al., "Validating whole slide imaging for diagnostic purposes in pathology: Guideline from the college of american pathologists pathology and laboratory quality center", Arch Pathol Lab Med, **1**, 1, (2013).

[145] D. Treanor, N. Jordan-Owers, et al., "Virtual reality powerwall versus conventional microscope for viewing pathology slides: An experimental comparison", Histopathology, **55**(3), 294-300, (2009).

[146] M. Bruchez, M. Moronne, et al., "Semiconductor nanocrystals as fluorescent biological labels", Science, **281**(5385), 2013-2016, (1998).

[147] Z. R. Jiang, R. Y. Li, et al., "Detecting genomic aberrations by fluorescence in situ hybridization with quantum dots-labeled probes", Journal of Nanoscience and Nanotechnology, **7**(12), 4254-4259, (2007).

[148] I. L. Medintz, H. Mattoussi, and A. R. Clapp, "Potential clinical applications of quantum dots", International Journal of Nanomedicine, **3**(2), 151-167, (2008).

[149] R. Drmanac, A. B. Sparks, et al., "Human genome sequencing using unchained base reads on self-assembling DNA nanoarrays", Science, **327**(5961), 78-81, (2010).

[150] D. J. Wu, C. M. Rice, and X. D. Wang, "Cancer bioinformatics: A new approach to systems clinical medicine", Bmc Bioinformatics, **13**, (2012).

[151] C. J. Wang, R. H. Xu, et al., "Bioinformatics method to analyze the mechanism of pancreatic cancer disorder", Journal of Computational Biology, **20**(6), 444-452, (2013).

[152] L. Badea, V. Herlea, et al., "Combined gene expression analysis of whole-tissue and microdissected pancreatic ductal adenocarcinoma identifies genes specifically overexpressed in tumor epithelia", Hepato-Gastroenterology, **55**(88), 2016-2027, (2008).

[153] W. W. Nie, L. Jin, et al., "The bioinformatics analysis of mirnas signatures differentially expressed in her2(+) versus her2(-) breast cancers", Cancer Biotherapy and Radiopharmaceuticals, **28**(1), 71-76, (2013).

[154] D. J. Higham, G. Kalna, and M. Kibble, "Spectral clustering and its use in bioinformatics", Journal of Computational and Applied Mathematics, **204**(1), 25-37, (2007).

[155] J. P. Brunet, P. Tamayo, T. R. Golub, and J. P. Mesirov, "Metagenes and molecular pattern discovery using matrix factorization", Proceedings of the National Academy of Sciences of the United States of America, **101**(12), 4164-4169, (2004).

[156] O. Alter, P. O. Brown, and D. Botstein, "Singular value decomposition for genome-wide expression data processing and modeling", Proceedings of the National Academy of Sciences of the United States of America, **97**(18), 10101-10106, (2000).

[157] B. Andreopoulos, A. J. An, X. G. Wang, and M. Schroeder, "A roadmap of clustering algorithms: Finding a match for a biomedical application", Briefings in Bioinformatics, **10**(3), 297-314, (2009).

[158] H. Pirim, B. Eksioglu, A. D. Perkins, and C. Yuceer, "Clustering of high throughput gene expression data", Computers & Operations Research, **39**(12), 3046-3061, (2012).